Measurement of Non-$D\bar{D}$ Decays of the psi(3770) Resonance at BESIII

A THESIS
SUBMITTED TO THE FACULTY OF THE GRADUATE SCHOOL
OF THE UNIVERSITY OF MINNESOTA
BY

Derrick Richard Toth

IN PARTIAL FULFILLMENT OF THE REQUIREMENTS
FOR THE DEGREE OF
DOCTOR OF PHILOSOPHY

Ron Poling, Adviser

May 2014

First, I would like to thank my adviser, Professor Ron Poling, for his mentoring and guidance throughout my graduate research. I am very lucky to have had such a great adviser. Although he became very busy after taking on the responsibilities of the Head of the School of Physics and Astronomy, I never felt neglected. He always had an open door for me, and for that I am very grateful.

I would also like to thank Jianming Bian for his development of the hadronic selection cuts and the extrapolation of the hadronic efficiency portions of this analysis and to Pete Zweber who developed the selection cuts before him. Thanks also to Hajime Muramatsu who originally performed a similar analysis at CLEO-c and is now a member of the MN BESIII group. It has been my pleasure to work with them, and I appreciate the discussions we've had throughout the years.

Thanks also to the other current and past members of the MN BESIII group: Dan Cronin-Hennessy, Nick Howell, Andy Julin, Xiaoli Niu, Zeb Perrin, Adam Peterson, Katherine Reeves, Nick Smith, and Can Zhang. My time at the University of Minnesota has been wonderful, thanks in large part to the people with whom I've worked. Particular thanks go out to Nick Howell and Zeb Perrin for their management of the software used to operate the Minnesota Monte Carlo farm; it was a life-saver having you guys.

I also appreciate the hard work of the BEPCII accelerator group and the BESIII collaboration. They provided the data and software upon which my thesis is based.

I thank my parents for the love and encouragement they've given me. They were instrumental in shaping me into the person I've become. Their support has helped me to flourish, and for that I thank them. My sister, Erica, has always been there for me through the years, and I'm very thankful to have such an awesome sibling.

I'm also very lucky to have a wonderful extended family. Thanks to Arlin, Caroleen, Jack, and Cassandra, my life has been better for your inclusion in it.

Finally, I would like to thank my wife Jami. I'm truly lucky to be married to such a woman. Her love and caring throughout my graduate career have helped me get through some of the most stressful parts of my life. I always had a ride in to work on rainy days, thanks to her. I greatly appreciate all of the small things she does to show me her love, and it always brings a smile to my face to remember them, no matter how I'm feeling at the time.

Once again, thank you all for what you've meant to me, I wouldn't be here without you.

To my family, thank you for all of the love and support throughout the years. And to my daughter-to-be, Julia Kay, I hope I can make you feel as loved as I've always felt.

Abstract

We measure the branching ratio for $\psi(3770) \to non-D\bar{D}$ final states at $E_{CM} = 3.773$ GeV to be $(9.54 \pm 0.31(stat) \pm 2.64(sys))\%$ using 2.92 fb^{-1} of e^+e^- annihilation data collected with the BESIII detector at the BEPCII collider at 3.773 GeV, as well as 44.5 pb^{-1} taken at 3.65 GeV and a total of 18.7 pb^{-1} taken at five points between 3.5 GeV and 3.671 GeV. The cross sections of $\psi(3770) \to D^0\bar{D}^0$ and $\psi(3770) \to D^+D^-$ at $E_{CM} = 3.773$ GeV are also measured as $(3.641 \pm 0.010(stat) \pm 0.047(sys))$ nb and $(2.844 \pm 0.011(stat) \pm 0.036(sys))$ nb, respectively.

Contents

List of Tables

List of Figures

1 Introduction

This dissertation is concerned with the measurement of the cross section of two classes of decays of the charmonium resonance $\psi(3770)$, namely the open-charm $D\bar{D}$ decays and the non-$D\bar{D}$ decays. We measure the total cross section of the $\psi(3770)$ resonance and its $D\bar{D}$ cross section, and then subtract the $D\bar{D}$ cross section from the total to obtain the non-$D\bar{D}$ cross section. The rate of non-$D\bar{D}$ decays will provide insight into the structure of the $\psi(3770)$ resonance and the interactions governing its decay. The BESIII detector is an ideal laboratory for such a measurement, using the high integrated luminosity delivered by the BEPCII electron-positron collider at the $\psi(3770)$ peak energy. A brief review of particle physics described by the Standard Model is necessary to put this measurement into the proper context. Ho-Kim and Pham's Elementary Particles and Their Interactions [1] and Das and Ferbel's Introduction to Nuclear and Particle Physics [2] provide the basis for much of the material covered in this introduction.

1.1 Elementary Particles and the Standard Model

The Standard Model of particle physics is a theory which describes three of the four fundamental forces of nature, and the elementary particles that mediate and are governed by these forces.The forces which are described in the Standard Model are, in order of decreasing strength, the strong force, the electromagnetic force, and the weak force. The only known fundamental force not accounted for in the Standard Model is gravity. Other notable phenomena which are not accounted for by the Standard Model are the dark energy and dark matter necessary to explain certain cosmological data, as well as the oscillation of neutrinos which necessitates a non-zero neutrino mass.

The elementary particles in the Standard Model consist of two different classes of particles differentiated by their spins. Matter is comprised of fundamental particles with half-integer spin known as fermions. The defining characteristic of fermions is that they follow Fermi-Dirac statistics. Particles obeying Fermi-Dirac statistics are not able to exist in a system with an identical particle occupying the same quantum state, a principle known as "Pauli Exclusion." The other main class of fundamental particles are bosons, which have integer spin and obey Bose-Einstein statistics. Bose-Einstein statistics are applicable for particles which are indistinguishable and able to occupy the same quantum state. The gauge bosons of the Standard Model are force carriers which mediate the interactions between particles.

There are two kinds of fundamental fermions, defined by the fundamental forces through

which they interact. The quarks are the set of fundamental fermions which interact through all three of the forces described by the Standard Model. The quarks come in three generations of increasing mass with pairs having $\frac{2}{3}$ and $-\frac{1}{3}$ of the elementary electron charge, as well as color charge associated with the strong interaction. The up, charm, and top quark are the three quarks in order of increasing mass with a charge of $\frac{2}{3}$, while the down, strange and bottom quark have $-\frac{1}{3}$ charge. The quarks also have anti-particles with opposite charge and the same mass. Quarks are never observed in isolation, but are found in composite particles, and thus only integer units of elementary charge are observed. Leptons are the fundamental fermions which do not participate in the strong interaction, but do participate in the weak force. Leptons also come in three generations of pairs, with one of the pair having electric charge equal to the elementary charge and the other having zero electric charge. The leptons with zero electric charge are known as neutrinos and do not interact through the electric force, while the charged leptons interact electromagnetically. Like the quarks, the charged leptons have different masses across the generations and anti-particles with opposite charges. The neutrinos were assumed to have zero mass by the Standard Model, but oscillations of neutrinos between flavor eigenstates demonstrate the necessity of small but non-zero masses. The charged leptons in order of increasing mass are the electron, muon, and tau.

The gauge bosons of the Standard Model are the fundamental vector particles that mediate the interactions between particles. There are eight gluons corresponding to the generators of the symmetry group $SU(3)$, which is the symmetry group describing the strong interaction. They are massless and have color charge, and thus can interact among themselves. Although the gluons are massless, the strong force coupling constant scales as distance so that interactions are effectively limited to short range. The photon is the massless mediator of the electromagnetic field. The massless nature of the photon allows the electromagnetic force to interact at long range. Due to its lack of electric charge, the photon cannot interact with itself. The weak force is mediated by the massive $W^{\pm}$ and Z^0 bosons with electric charges of ± 1 and 0 in units of fundamental electric charge, respectively. The longitudinal components of these bosons correspond to the massless Nambu-Goldstone bosons of the $SU(2) \times U(1)$ symmetry group which acquire mass through the Higgs mechanism, consequently limiting the range of the weak interaction. An estimate of the ratios of the effective coupling strength of the fundamental forces to the strong interaction are $1, 10^{-2}$, and 10^{-5} for the strong, electromagnetic, and weak forces, respectively. Although not described by the Standard Model, the ratio for gravity is 10^{-39}.

The Higgs boson is a fundamental scalar boson whose interactions with particles give

them their masses. The Higgs field responsible for the Higgs boson is a rotationally invariant (scalar) field which achieves a non-zero vacuum expectation value from spontaneous symmetry breaking. The Higgs bosons can self-interact, and are thus themselves massive particles. Table 1 summarizes the properties of the fundamental particles of the Standard Model.

				Gauge Bosons	Higgs Boson
Quarks	$\frac{2}{3}$ $\frac{1}{2}$ u ~ 2.3 MeV	$\frac{2}{3}$ $\frac{1}{2}$ c 1.3 GeV	$\frac{2}{3}$ $\frac{1}{2}$ t 173 GeV	0 1 g 0	0 0 H 126 GeV
	$-\frac{1}{3}$ $\frac{1}{2}$ d ~ 4.8 MeV	$-\frac{1}{3}$ $\frac{1}{2}$ s ~ 95 MeV	$-\frac{1}{3}$ $\frac{1}{2}$ b 4.2 GeV	0 1 γ 0	
Leptons	-1 $\frac{1}{2}$ e 511 keV	-1 $\frac{1}{2}$ μ 106 MeV	-1 $\frac{1}{2}$ τ 1777 MeV	± 1 1 W 80 GeV	
	0 $\frac{1}{2}$ ν_e < 2 eV*	0 $\frac{1}{2}$ ν_μ < 2 eV*	0 $\frac{1}{2}$ ν_τ < 2 eV*	0 1 Z 91 GeV	

*The neutrinos are listed here as flavor eigenstates and so their masses are not well-defined in this basis. The listed masses correspond to the mass eigenstates which have the largest component from the listed flavor eigenstate.

Table 1: Summary of the properties of fundamental Standard Model particles [3]. The charge, spin, and mass of the particles appear on the top left, top right, and bottom, respectively.

1.2 Symmetry and Noether's Theorem

Symmetries play a vital role in physics, and are particularly important in the study of particle physics. Emmy Noether first proved that any symmetry of a system would necessitate a conserved quantity. The invariance of physical laws under continuous transformations of position, time, orientation, and Lorentz transformation leads to the convservation of momentum, energy, angular momentum, and group generators. Similarly, symmetries with

respect to discrete transformations of space, time, and charge lead to conservation of parity and invariance of time and charge inversion.

The fundamental forces of the Standard Model are gauge fields which are invariant under unitary symmetries in the internal space of the field. This invariance leads to conservation of quantum numbers associated with color, electric charge, and weak isospin. Many other symmetries are approximate and sometimes broken, but are still useful because these symmetries are respected or not in a systematic way. For example, charge-parity conservation is broken by the weak interaction, but not by the other forces.

1.3 Charmonium Spectroscopy

Bound states of a $c\bar{c}$ (charm/anti-charm quark) pair present an excellent laboratory for the study of Quantum Chromodynamics (QCD), the theory of the strong force. The many states of $c\bar{c}$ are analogous to the excited states of the hydrogen atom. Similar to the way in which emission lines from hydrogen can be studied to understand the underlying electromagnetic interaction between the proton and electron, the mass of various charmonium states hints at the strong potential binding the $c\bar{c}$ quarks. Using a color Coulomb potential at short distances and a scalar potential varying linearly for long distance interactions, the mass of various states with quantum numbers $N^{2s+1}L_J$ can be predicted, where N is the principal quantum number, s is the total spin, L is the angular momentum, and J is the total angular momentum. Charmonium is composed of two fermions, and so its total spin can be one or zero. The notation for L follows standard spectroscopic notation, where $L = 1, 2, 3$, and 4 corresponds to S, P, D, and F, while higher states follow alphabetically, omitting J. The results of these predictions for both a non-relativistic potential and a relativized extension of this potential are shown along with experimental measurements in Figure 1 [4, 5].

$D\bar{D}$ threshold is the lowest center-of-mass energy that is able to produce a pair of open-charm D mesons ($c\bar{u}$ and $\bar{c}u$, or $c\bar{d}$ and $\bar{c}d$). Below $D\bar{D}$ threshold, there is fairly good agreement between the predicted masses and the experimental data. However, above $D\bar{D}$ threshold, the more complicated dynamics create larger disagreements. Although some resonances still qualitatively agree with their predictions, there are many states which have been predicted, but not found, as well as several states which have been found experimentally, but with no corresponding prediction. The $\psi(3770)$ state, an excitation of the $c\bar{c}$ vector state, is qualitatively predicted, but not in very good agreement with its prediction as a pure 1^3D_1 state. This may at least be partially due to a mixing with the 2^3S_1 $\psi(3686)$ [6, 7]. This mixing is also supported by a rate for $\psi(3770)$ decay to e^+e^- that is

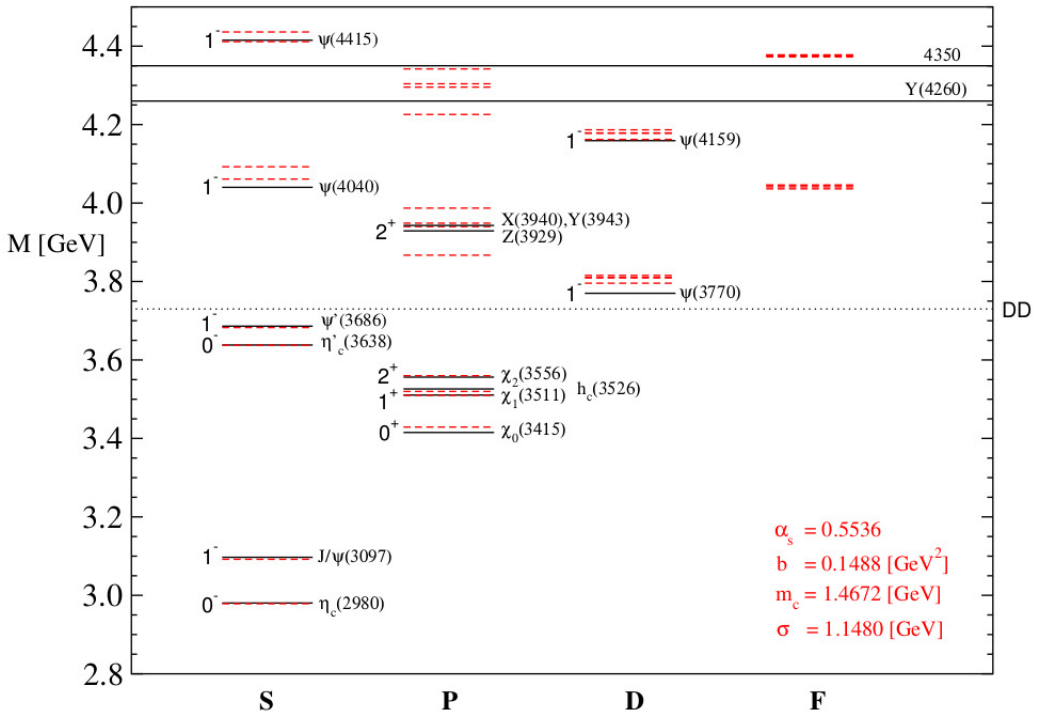

Figure 1: The charmonium spectrum with measured resonances shown with solid lines and predicted states shown with dashed lines. The J^P values are shown to the left of the lines and the particle names to the right. The orbital angular momentum states are indicated on the horizontal axis. The open-charm $D\bar{D}$ threshold is also indicated.

measured to be relatively larger than if the $\psi(3770)$ were a pure 1^3D_1 state [7].

1.4 Fermi's Golden Rule

Fermi's Golden Rule is the result that in perturbation theory the probability per unit time of decaying to a continuum of energy eigenstates is proportional to the density of final states and the Hamiltonian matrix element connecting the initial and final states as

$$P_{i\to f} = \frac{2\pi}{\hbar}| < f|H|i > |^2\rho(E_f). \tag{1}$$

Thus a larger number of ways to achieve a given final-state and a larger interaction strength will increase the probability of decay, and consequently shorten the lifetime of the initial-state particle. For a particle of mass $M = M_0$, the time-dependent wave function may be written as

$$\psi(t) \propto e^{-\frac{ic^2}{\hbar}(M_0 - i\frac{\Gamma}{2})t}. \tag{2}$$

This equation guarantees the exponential decay of the particle with mean-lifetime of $\frac{\hbar}{\Gamma c^2}$. When the Fourier transform of Equation 2 is taken and squared, it gives the Breit-Wigner equation

$$|\psi(M)|^2 \propto \frac{1}{(M - M_0)^2 + \frac{\Gamma^2}{4}}. \tag{3}$$

The interaction probability (cross section) of particles colliding with center-of-mass energy M is increased in the neighborhood of particle resonances of mass M_0 if the resonance is compatible with the quantum numbers of the colliding particles. The BEPCII collider, described in Section 2.1, collides e^+e^- pairs and is able to produce by annihilation via virtual photons $c\bar{c}$ resonances with $J^{PC} = 1^{--}$, corresponding to angular momentum, parity, and charge-conjugation quantum numbers. The produced resonance has the same quantum numbers as the photon because it is produced through a virtual photon. This reaction is shown in Figure 2.

Figure 3 shows the cross-section ratio $R(s) = \sigma(e^+e^- \to hadrons)/\sigma(e^+e^- \to \mu^+\mu^-)$ across the approximate center-of-mass energy range through which BEPCII can run. From this plot it can be seen that the $\psi(3770)$ resonance is much broader than the lower energy $c\bar{c}$ states J/ψ and $\psi(2S)(\psi(3686))$. The strong interaction has the largest interaction strength and thus strong interactions will contribute the most to a resonance's width unless the strong interaction is suppressed relative to the electromagnetic and weak interactions.

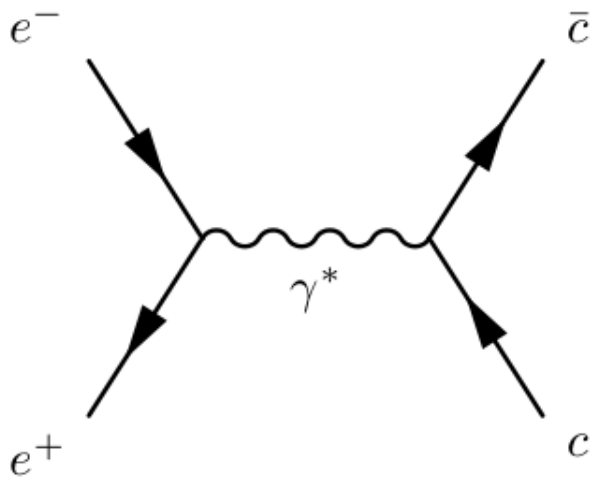

Figure 2: Feynmann diagram of a 1^- $c\bar{c}$ resonance created through a virtual photon with an e^+e^- collision.

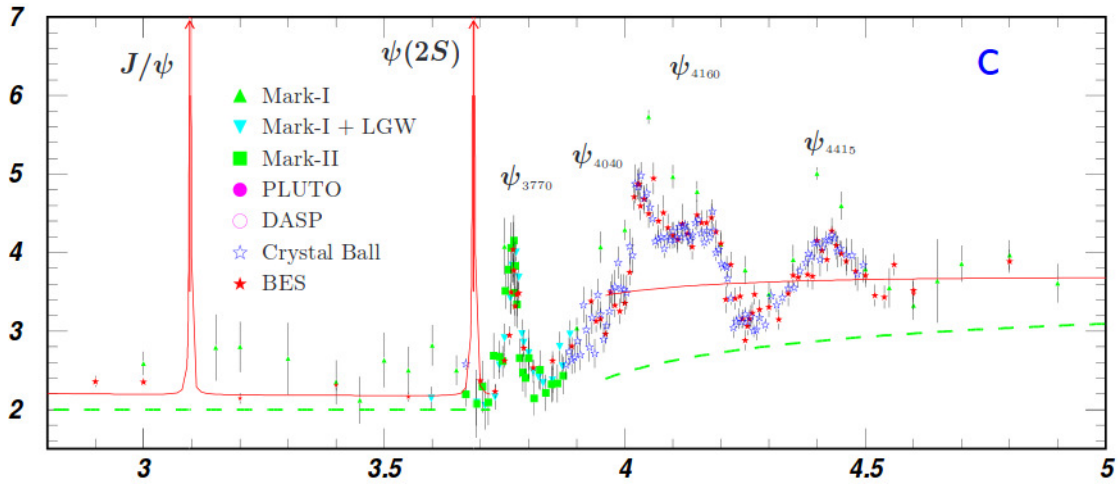

Figure 3: A plot of $R(s) = \sigma(e^+e^- \to hadrons)/\sigma(e^+e^- \to \mu^+\mu^-)$ across a center-of-mass energy range, $\sqrt{s}$, from 2.8-5 GeV.

The $\psi(3770)$ resonance is able to decay via the tree-level strong interaction illustrated in Figure 4 to an open-charm final state of $D\bar{D}$. Depending on whether a $u\bar{u}$ or a $d\bar{d}$ quark pair is generated, a $D^0\bar{D}^0$ or D^+D^- meson pair will be created. The J/ψ and $\psi(3686)$, however, do not have a large enough rest mass to produce a $D\bar{D}$ pair.

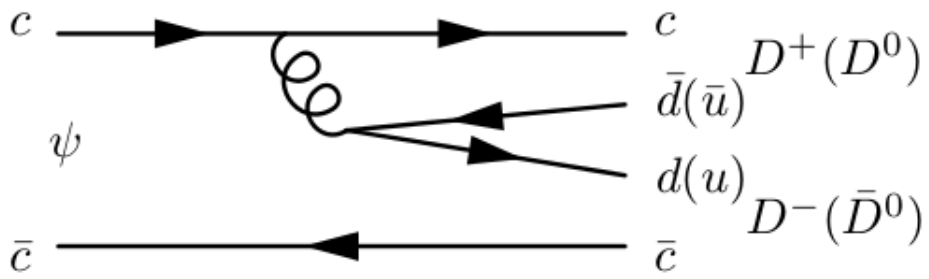

Figure 4: Feynmann diagram of the tree-level strong decay of $\psi \to D\bar{D}$ above open-charm threshold.

The J/ψ and $\psi(3686)$ are color-singlet states with a negative charge conjugation parity. The strong interaction respects C-parity, and so the number of gluons exchanged in a decay must be odd for the decay to proceed through only the strong force. The least number of gluons which can produce a color singlet with the same C-parity as these resonances is three, and a typical decay of this type is shown in Figure 5. The suppression of strong decays in such a way is known as the OZI rule for Okubo [8], Zweig [9], and Iizuka [10] who independently proposed it. The suppression is due to the increased number of vertices in the Feynmann diagram along with the larger momentum transfer of the gluons, as the strong interaction strength decreases as a function of momentum.

Besides the open-charm decay shown in Figure 4, the J/ψ, $\psi(3686)$, and $\psi(3770)$ will have similar decay channels available to them. Due to the relative strength of the strong interaction to the weak and electromagnetic interactions, the widths of the 1^{--} charmonium states able to be produced at e^+e^- colliders are dominated by the strong interaction, except in cases such as the J/ψ and $\psi(3686)$ where this interaction is suppressed. Therefore, the $\psi(3770)$ is expected to decay predominantly to $D\bar{D}$ states.

1.5 Theoretical Predictions of $\mathcal{B}(\psi(3770) \to non - D\bar{D})$

The $\psi(3770)$ resonance decays predominantly through open-charm production of $D\bar{D}$, but it may also decay in other ways. There are several theoretical estimates of the partial decay

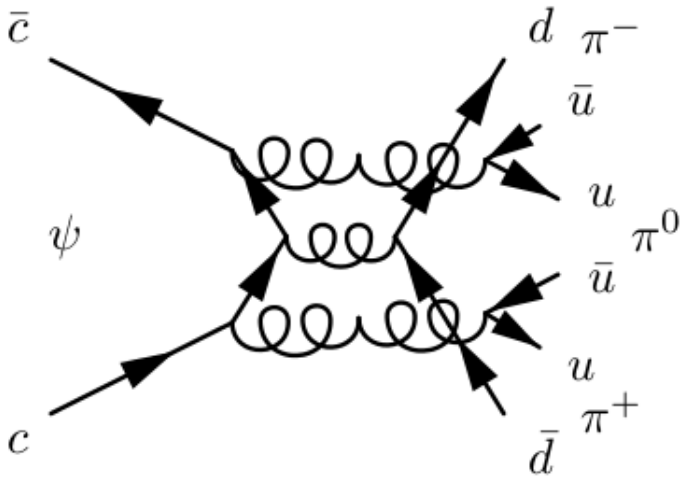

Figure 5: Example Feynmann diagram of the OZI-suppressed strong decay of $\psi \to \pi^+\pi^-\pi^0$.

transitions to χ_{cJ} states, for $J = 0, 1$, and 2, via a radiated photon. Ding, Chin, and Chao [11] use a QCD-motivated potential model with relativistic corrections to predict this rate. Although the $\psi(3770)$ state is predominantly a D-wave state, there is also a substantial S-wave component which is important to account for when calculating decay widths. Using the mixing angle favored by data, they calculate partial widths of 363, 60, and 13 keV for the partial width to $\gamma\chi_{cX}$ for $X = 0, 1$ and 2, respectively. Using a coupled-channel model and accounting for mixing through open charm states, Eichten, Lane and Quigg [12] calculate these widths to be 225, 59, and 3.9 keV. Using a Godfrey-Isgur relativized extension of a potential model, Barnes, Godfrey, and Swanson [4], predict widths of 213, 77, and 3.3 keV. Kuang and Yan predict the hadronic transition to $J/\psi\pi\pi$ to have a width between 30 and 160 keV [13] using a QCD multipole technique and accounting for the S- and D-wave mixing, while neglecting coupled channel contributions. Utilizing a non-relativistic QCD effective theory to the next-to-leading order, He, Fan, and Chao predict the width of $\psi(3770)$ to light hadrons to be 467^{+338}_{-187} keV [14]. Other transitions, such as decay to two leptons, are expected to contribute negligibly to the total width of the $\psi(3770)$. For example, Kuang and Yan determine the e^+e^- width to be 0.73 keV [13], and even this small width is about three times larger than that measured in data, presumably due to large unaccounted-for QCD corrections. Using the experimentally measured full width of the $\psi(3770)$, 27.2 ± 1.0 MeV [3] and summing the predicted exclusive non-$D\bar{D}$ decay widths gives an approximate expectation for $\mathcal{B}(\psi(3770) \to non - D\bar{D})$ of between 2% and 5%.

1.6 Experimental Measurements of $\psi(3770) \to non - D\bar{D}$

Previous experiments have measured the inclusive branching ratio of $\psi(3770) \to non - D\bar{D}$. BESII measured the branching fraction $\mathcal{B}(\psi(3770) \to non - D\bar{D}) = (15.1 \pm 5.6 \pm 1.8)\%$ [15] by directly measuring production of non-$D\bar{D}$ hadrons across a center-of-mass energy range from 3.65 to 3.87 GeV and fitting to determine the production of non-$D\bar{D}$ through the $\psi(3770)$ resonance. BESII also previously measured similar values of $\mathcal{B}(\psi(3770) \to non - D\bar{D})$ [16, 17, 18] through other means. CLEO-c measured $\mathcal{B}(\psi(3770) \to non - D\bar{D}) = (-3.3 \pm 1.4^{+6.6}_{-4.8})\%$, which corresponds to an upper limit of 9% at 90% confidence level [20]. CLEO-c measured the branching fraction by measuring the total observed cross section of $\psi(3770)$ to hadrons and subtracting off their previously measured value for $\sigma_{D\bar{D}}$. However, the main point of difference between these measurements is that CLEO-c corrects for interference between resonant and non-resonant production of hadrons via a virtual photon by assuming that the interference is the same as it is for $\mu^+\mu^-$, while BESII does not account for interference. Without this interference effect, CLEO-c would measure a branching fraction of $\sim 7\%$.

There are also several measurements of exclusive non-$D\bar{D}$ branching fractions. Among these are measurements of $\psi(3770) \to J/\psi\pi^+\pi^-$ [21, 22], $\psi(3770) \to J/\psi\pi^0\pi^0$ [22], $\psi(3770) \to J/\psi\eta$ [22], $\psi(3770) \to \phi\eta$ [23], $\psi(3770) \to \gamma\chi_{c1}$ [24], and $\psi(3770) \to \gamma\chi_{c0}$ [25]. However, as a total, these exclusive branching fraction measurements sum to only 1.4% of $\psi(3770)$ decays. Many searches have also set upper limits on branching fractions of other non-$D\bar{D}$ decays for final states including light hadrons [23, 26], baryons [27], $\rho\pi$ [28], K^0 pairs [29], $\pi^0 + X$ [30], and $\eta + X$ [30]. Table 2 summarizes experimental measurements of exclusive branching fractions for $\psi(3770) \to non - D\bar{D}$ and the corresponding theoretical predictions.

1.7 Possible Explanations of a non-$D\bar{D}$ Excess

In light of the possible excess of inclusive non-$D\bar{D}$ decays over previous theoretical predictions, there has been some effort to understand from where such events may originate. Voloshin suggests that an admixture of light quarks at $O(10\%)$ of probability weight factor may exist with the traditional $c\bar{c}$ pair in the $\psi(3770)$ resonance [31]. A $c\bar{c}$ pair within such a four-quark component would cause a larger non-$D\bar{D}$ width than a pure $c\bar{c}$ state because it could decay with only a single gluon. With this assumption and some reasonable constraints from data, $\mathcal{B}(\psi(3770) \to \pi^0 J/\psi)$ is estimated to be $\sim 2 \times 10^{-4}$ and $\mathcal{B}(\psi(3770) \to \eta J/\psi) \approx 0.14\%$

Lipkin [32] first suggested that long-range OZI-evading strong interactions may also

Decay Mode i	$\mathcal{B}(\psi(3770) \to i)$ (%)	
	Theory	**Experiment**
$\gamma\chi_{c0}$	1.33 [11], 0.83 [12], 0.78 [4]	$0.73 \pm 0.07 \pm 0.06$ [25]
$\gamma\chi_{c1}$	0.22 [11], 0.22 [12], 0.28 [4]	$0.28 \pm 0.05 \pm 0.04$ [24]
$\gamma\chi_{c2}$	0.048 [11], 0.014 [12], 0.012 [4]	< 0.09@90%CL [24]
$J/\psi\pi^+\pi^-$	0.074-0.392 [13]	$0.34 \pm 0.14 \pm 0.09$[21], $0.189 \pm 0.02 \pm 0.02$ [22]
$J/\psi\pi^0\pi^0$	0.037-0.196 [13]	$0.080 \pm 0.025 \pm 0.016$ [22]
$J/\psi\eta$	0.14 [31]	$0.087 \pm 0.033 \pm 0.022$ [22]
Light hadrons	$1.72^{+1.24}_{-0.69}$ [14]	$\psi(3770) \to \phi\eta =$ $0.031 \pm 0.006 \pm 0.003 \pm 0.001$ [23]
Total	2–5	1.4

Table 2: Theoretical and experimental values are shown for $\mathcal{B}(\psi(3770) \to i)$ for various non-$D\bar{D}$ final states. Theoretical predictions have been converted from partial widths to branching fractions by dividing by the experimentally measured total width of $\psi(3770), \Gamma_{\psi(3770)} = 27.2 \pm 1.0$ MeV [3]. Other exclusive modes not shown have been measured experimentally, but only upper limits have been obtained.

account for some of the non-$D\bar{D}$ decays. In this case, the $\psi(3770)$ initially dissociates into a $D\bar{D}$ pair and then re-scatters with a D meson exchange to produce a non-$D\bar{D}$ vector and pseudoscalar final state, shown in Figure 6. Only D exchanges are considered, as other meson loops would be suppressed by flavor and the OZI rule. Several groups have made predictions of $\psi(3770) \to VP$, where V and P are non-$D\bar{D}$ final states composed of a vector and pseudoscalar particle, respectively. Typically, such decays could account for branching fractions of 0.2–1% [33, 34], although up to 3.38–5.23% [35] is possible, depending on the phase angle chosen between the short-distance (OZI-suppressed) and long-distance (D rescattering) strong interactions.

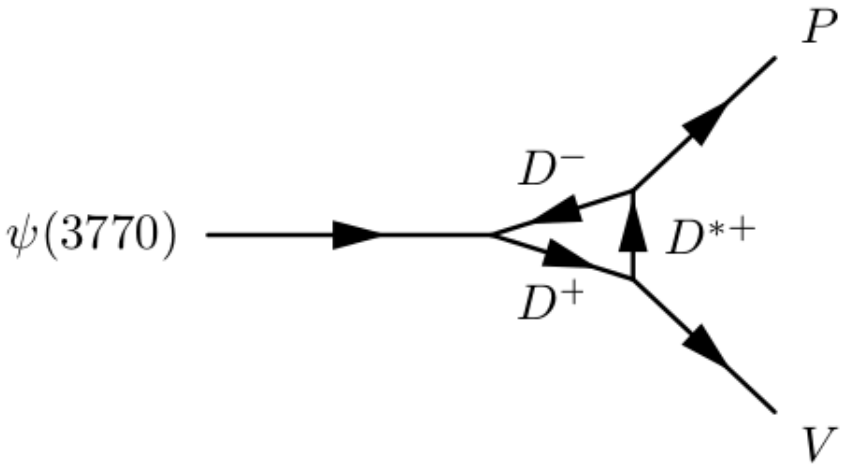

Figure 6: A Feynmann diagram of the OZI-evading strong decay of $\psi(3770) \rightarrow$ a vector and a pseudoscalar via rescattering with a D meson loop is shown. Many similar diagrams are possible with various D mesons and final-state vector and pseudoscalar particles.

2 Detector and Subsystems

The third Beijing Spectrometer (BESIII) detector is located on the campus of the Institute of High Energy Physics (IHEP) in Beijing, China and studies electron-positron annihilations provided by the second Beijing Electron-Positron Collider (BEPCII). These were built on the site of the previous BES detectors and the original BEPC collider. The original BEPC was built in 1989 and was a single-bunch electron-positron collider with a single storage ring, built to provide collisons at center-of-mass energies in the τ-charm region ($\sqrt{s}$ = (2-4.6) GeV) for the BES detector, as well as being a source for high flux synchrotron radiation. The BES detector was upgraded in 1996 to the BESII detector, and BEPC was upgraded throughout the years as well, until they were closed in 2004. At its peak, BEPC was able to deliver 10^{31} cm^{-2} s^{-1} instantaneous luminosity.

BESIII and BEPCII were commissioned in 2003 and began operation in 2009. BEPCII is a two ring collider 237.5 m in circumference operated with multiple electron and positron bunches. The design luminosity is two orders of magnitude larger than its predecessor, 10^{33} cm^{-2} s^{-1}, optimized for 2×1.89 GeV center-of-mass energy, just above the open-charm threshold. The BESIII detector was commissioned along with BEPCII in order to take advantage of new detector technology and the greatly increased luminosity provided by the upgrade to BEPCII. The large data statistics and precise detection provided by BEPCII and BESIII allow for many important precision measurements and searches for rare decays in the τ-charm energy region. For a detailed description of the BESIII detector see Ref. [36].

2.1 BEPCII Accelerator and Storage Ring

To obtain high integrated luminosity data sets, BEPCII must provide high instantaneous luminosity, along with efficient running. Many tightly spaced bunches of electrons and positrons enable the high beam currents necessary. BEPCII operates with 93 bunches in each evacuated ring that are about 1.5 cm long and spaced 8 ns (2.4 m) apart, giving a single-beam current of 0.91 A when run in collison mode (design parameter, not yet achieved). These beams collide at the interaction point with a crossing angle of 11 milliradians and are focused by super-conducting quadrupole magnets near the interaction point using the micro-β technique to compress the vertical beam size to about 5.7 μm. The horizontal beam size is about 380 μm.

To take data with the BESIII detector, electrons and positrons must be circulating in the BEPCII storage rings. Initially, positrons are created by firing electrons at a fixed target. The positrons are created in pairs from photons which interact with the target material to

form e^+e^- pairs. The positrons are then separated magnetically, accelerated, and finally injected into the positron storage ring. Once the positrons in the storage ring have reached the desired beam-current, the electrons are injected. Electron injection proceeds much more quickly because they do not have to created, as the positrons do, but only accelerated and injected. The positrons are injected with a current of 50 mA/min, and the electrons are injected at 200 mA/min.

After injection, the e^+e^- beams are collided and data is taken by BESIII. During the normal course of running, the beams become depleted due to the particles being lost to interactions, both in the desired interaction point collisions and undesired beam-gas collisions because of imperfect vacuum. At a certain point, the currents stored in the beams are non-zero but are below the point of usable instantaneous luminosity. At this point, the beam-currents must be restored to their original levels. BEPCII takes advantage of "top-off" injection, which allows the electron and positron beams to be replenished after a run without completely dumping the beams. This method requires that the injection and collision optics be nearly identical.

2.2 BESIII Detector

The BESIII detector, shown in Figure 7, is centered on the interaction point of the colliding e^+ and e^- beams. The coordinate system used is a right-handed coordinate system located at the center of the BESIII detector. The positive z-axis is along the direction of the positron beam, the positive y-axis points vertically upward, and the positive x-axis points horizontally to the center of the BEPCII ring. The spherical coordinates can be obtained by following standard conventions from Cartesian coordinates. The interactions between the e^+ and e^- beams take place within the beam-pipe, which has an inner radius of 31.5 mm and an outer radius of 57 mm. The beam-pipe must minimize multiple-scatterings and secondary interactions, while being able to maintain high vacuum. The design vacuum pressure is 5×10^{-10} torr. The entire detector is located within a uniform 1 Tesla magnetic field in the z-direction provided by a Super-Conducting Solenoid. This magnetic field was chosen to yield sufficient curvature of charged tracks for precision measurements of momenta in the τ-charm energy region, while limiting the number of charged particles that "curl up" within the tracking volume, and complicating pattern recognition and eliminating useful information from other parts of the detector. The Super-Conducting Solenoid has a mean radius of 1.482 m and a length of 3.53 m.

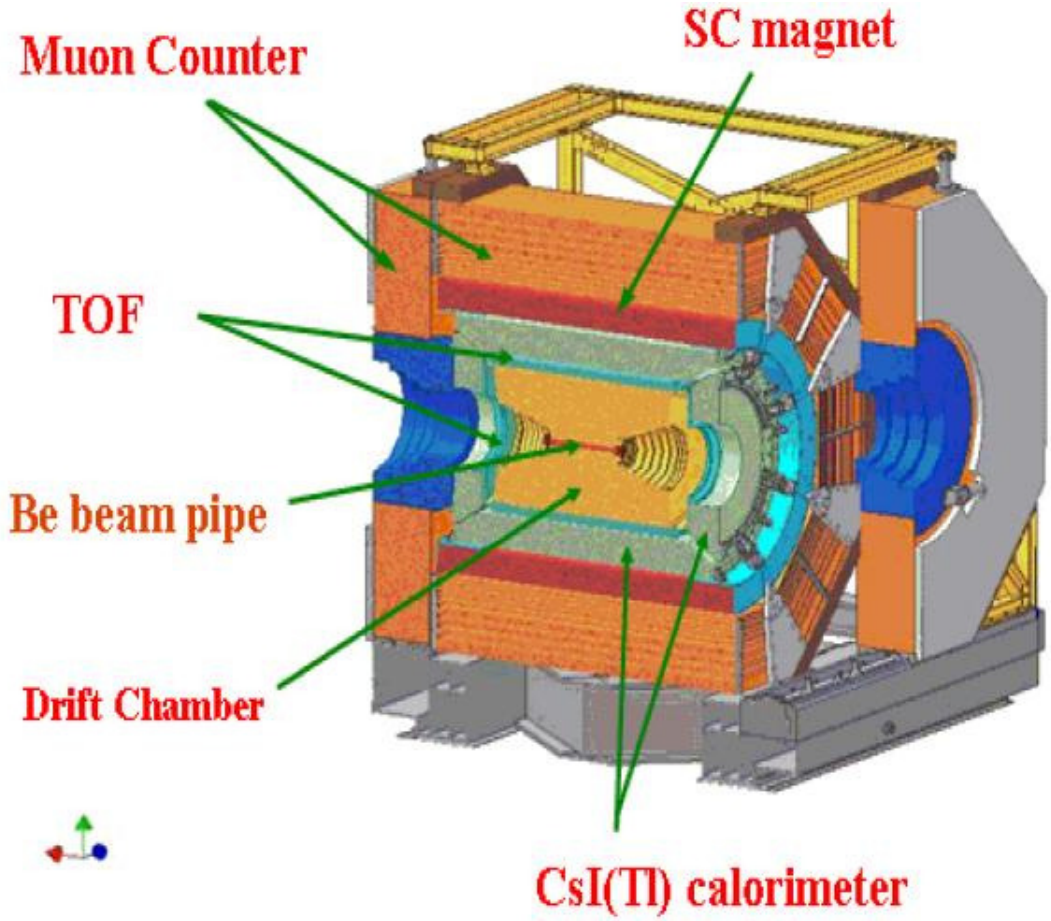

Figure 7: BESIII detector and its sub-systems.

2.2.1 Multi-Layer Drift Chamber

Working from the inside to the outside of the detector, the first system is the Multilayer Drift Chamber (MDC), which detects charged particles and precisely measures their trajectories and energy deposition.The MDC also provides level 1 triggers, described in Section 2.3, to sort physics events from the various backgrounds. Because the detector is within a uniform magnetic field, the helical trajectory of a charged particle allows determination of its charge and momentum.

The MDC is a gas-filled chamber that tracks charged particles passing through its volume by measuring the ionization they cause. The ion-electron pairs created when a charged particle passes through are prevented from recombining by a large electric field applied to the drift chamber. Tungsten wires are used to create a constant electric field that is tuned to a strength that causes the ionized electrons to travel toward alluminum sense wires without causing secondary ionization. The electric field close to the sense wires is much larger than the constant electric field throughout most of the MDC volume. When the ionized electrons get very close to the sense wires, they create an avalanche of secondary ionizations which is proportional to the original amount of ionization. The current caused in the sense wires by these electrons gives a measurement of the energy deposition from the primary ionization, and the locations of the triggered sense wires tracks the path of charged particles travelling through the drift chamber.

The MDC takes measurements of the charged tracks in 43 layers using sense wires set at small stereo angles to allow 3-D track reconstruction of the particle's trajectory. The MDC has an inner radius of 59 mm and an outer radius of 810 mm while covering 93% of the 4π solid angle.The end plates of the inner chamber have a stepped, conical shape to accommodate the final focusing quadrupole being placed as closely to the interaction point as possible. The MDC has a multi-layer, small cell design, with the single cells giving a position resolution better than 130 μm in the r-ϕ plane, and a position resolution of 2 mm in the beam direction at the interaction point. The uncertainty in position resolution is dominated by electron diffusion and time uncertainty due to electronics readouts. The transverse momentum resolution is about 0.5% at 1 GeV/c. The main contributions to momentum uncertainty are the uncertainties from the wire position measurements and from multiple scatterings from material in the drift chamber.

The MDC has a gas mixture of He:C_3H_8 in a ratio of 60:40; this mixture assures efficiency, while minimizing multiple scatterings which would degrade momentum resolution. The helium is chosen because it is the noble gas with the lowest atomic number. Being a

noble gas insures that helium is chemically inert, and so it will not interact with the ionized electrons which measure the position and energy loss of the particle being detected. The low atomic number gives it a long radiation length which reduces the incidence of multiple-scattering. The C_3H_8 acts as a quenching gas which diffuses the energy of ionization through rotational, vibrational, and other means inaccessible to the helium. If the ionization energy were not diffused, the energy measurements in the drifter chamber would be degraded.

The measurements made in the MDC are also used to measure the rate of energy loss per distance, dE/dx. The dE/dx information is used to identify the various long-lived particles because the rate a charged particle deposits energy while travelling through material depends on the particle's velocity and hence its mass [37],

$$-\frac{dE}{dx} = \frac{4\pi}{m_e c^2} \cdot \frac{nz^2}{\beta^2} \cdot \left(\frac{e^2}{4\pi\epsilon_0}\right)^2 \cdot [ln\left(\frac{2m_e c^2\beta^2}{I \cdot (1-\beta^2)}\right) - \beta^2], \tag{4}$$

where ϵ_0 is the vacuum permittivity, n is the electron number density of the MDC, and I is the mean excitation potential for the electrons in an atom of the medium. A scatter plot of normalized dE/dx pulse height vs. momentum is shown in Figure 8. The measured dE/dx is then compared against the expected value and associated uncertainty for a particular particle hypothesis to calculate the deviation from that particle hypothesis for a single measurement:

$$\chi_i = \frac{dE/dx_{measured} - dE/dx_{expected}}{\sigma_i} \tag{5}$$

The total MDC χ^2 is then taken from the sum in quadrature over the hits used to reconstruct the particle's trajectory. This information is used along with measurements from the Time of Flight system described in Section 2.2.2 to calculate the probabilities of the various particle hypotheses. This PID information is used in our selection cuts described in Section 6.2.1. The dE/dx resolution is about 6% for particles with an incident angle of 90° to the beam-axis, with uncertainties arising from fluctuations in the number of primary ionizations along the flight path, fluctuations in the avalanche process, and edge effects from the cells. The dE/dx information provides a 3σ K/π separation for particles with momenta of up to 770 MeV/c.

2.2.2 Time-of-Flight System

The next detector component is the Time-of-Flight (ToF) system. The ToF determines the time it takes charged particles to reach a bank of plastic scintillation detectors mounted on

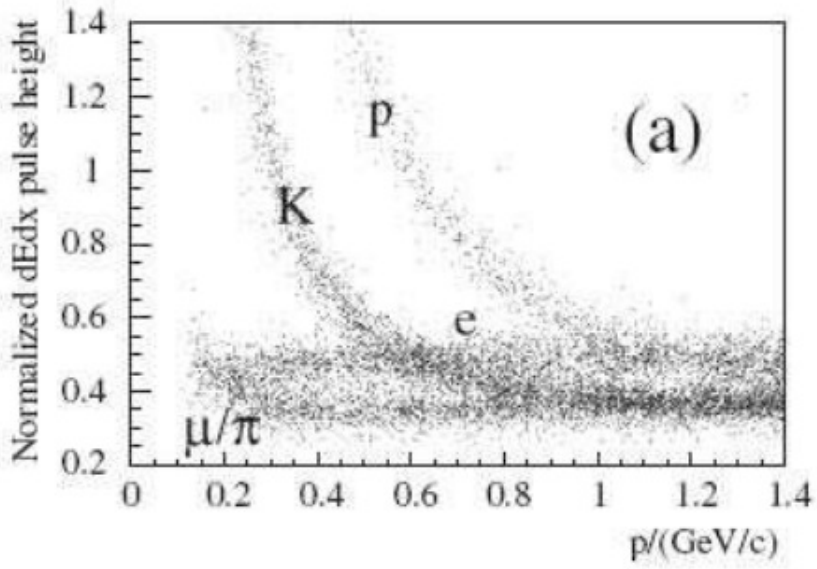

Figure 8: A scatter plot of the normalized dE/dx pulse height vs. momentum described in Section 2.2.1.

the outer surface of the MDC and provides input into the level 1 trigger. Measurements are made from two different bands of staggered scintillation detectors attached to fine mesh photomultiplier readout tubes; one bank is located 0.81 m from the beam-line, and the other is located 0.86 m from the beam-line. This timing measurement enables calculation of the particle's velocity, which allows for separation of particles with similar momenta, but different masses. The measured time of flight is compared against the expected time of flight based on the flight path, the momentum measurement from the MDC, and the particle mass of that particular PID hypothesis. This is divided by the uncertainty in the time measurement and used with the dE/dx measurement from the MDC to calculate the probability of a particular PID hypothesis. A scatter plot of mass-squared vs. momentum is shown for various particles in Figure 9.

The ToF system, shown in Figure 10, is composed of a dual-layer barrel region covering $|cos\theta| < 0.82$, and two single-layer end cap regions covering $0.85 < |cos\theta| < 0.95$. MDC support structure and service lines go through the ToF and are the reason for the dead zone in the polar angle coverage of the ToF. Each layer in the barrel has 88 scintillators which are 5 cm thick with a trapezoidal cross section. There are 48 fan-shaped scintillators in each end cap region. The ToF system has a resolution of about 100 ps, with contributions

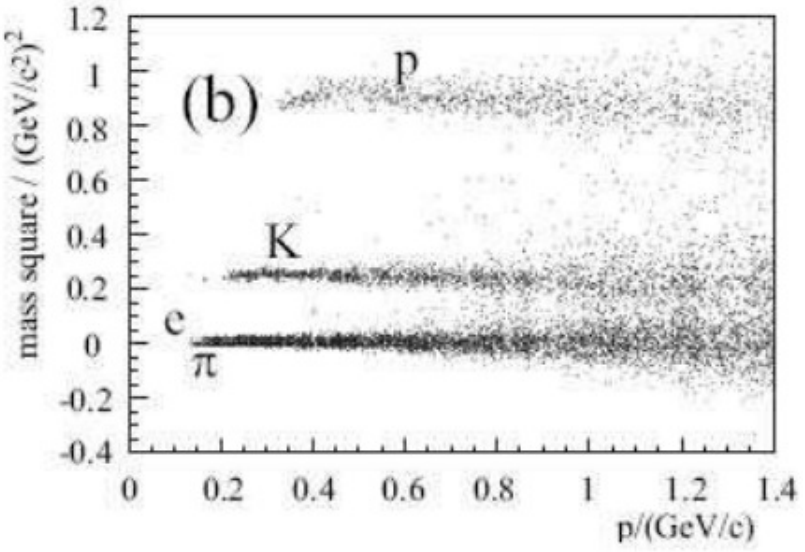

Figure 9: A scatter plot of the mass-squared measured by the ToF, described in Section 2.2.2, vs. momentum.

mostly from uncertainty due to scintillation light rise time, and fluctuations associated with the PMTs. The ToF detector allows 3σ K/π separation for particles with momenta of up to 900 MeV/c and that are at 90 $^\circ$ to the beam-axis.

2.2.3 Electromagnetic Calorimeter

The Electromagnetic Calorimeter (EMC) measures the energy of photons and provides good e/π separation for particles with momenta greater than 200 MeV/c, as well as contributing to the level 1 trigger. Measurements of photon energy below 20 MeV are not considered, as this level of energy is indistinguishable from noise. The EMC's precise energy and approximate direction measurements of photons are used in reconstruction of π^0s and other neutral particles which are reconstructed from their decays into photons.

The EMC is composed of 6,240 CsI(Tl) tellurium-doped cesium iodide crystals which have square front faces that are 5.2 cm to a side and are read out by photodiodes.The crystals are 28 cm (15 radiation lengths) long. These crystals are all set with a small tilt of 1.5 $^\circ$ in the ϕ-direction and about 1.5 $\sim 3^\circ$ in the θ-direction to prevent photons from aligning with the cracks between the crystals. The EMC has an inner radius of 94 cm, and weighs about 24 tons. The energy resolution is σ/E = 2.5% at 1 GeV and 4% down to

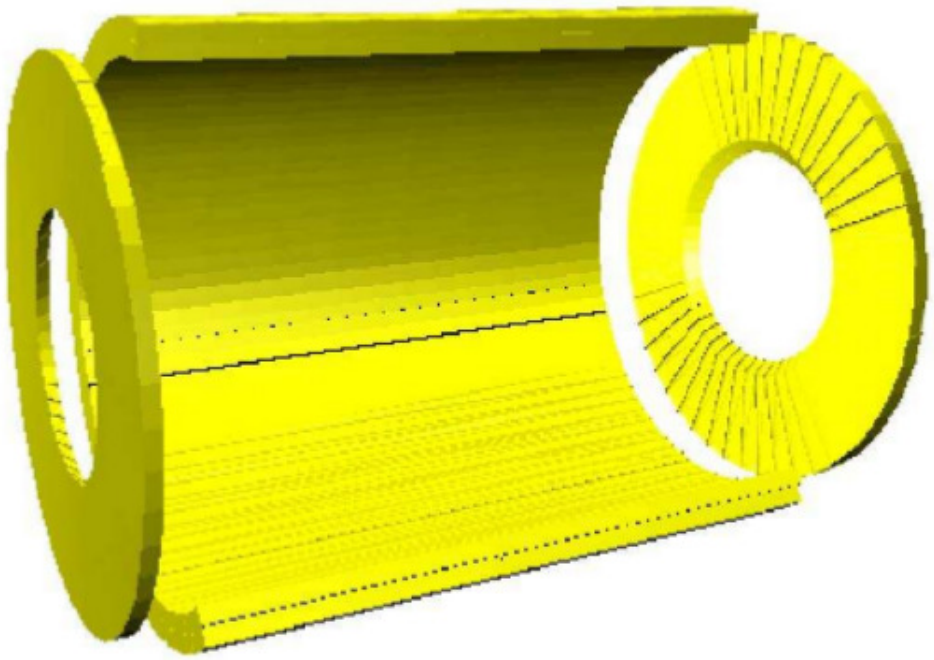

Figure 10: The BESIII Time-of-Flight system with dual-layer barrel region and two single-layer end cap regions, described in Section 2.2.2.

100 MeV. The main uncertainties in the energy measurement are from energy loss out the backs of the crystals and in the dead areas between crystals, and from non-uniform light production. Energy from the ToF is also added back into the EMC energy for showers which began in the ToF. The EMC position resolution is $\sigma = 0.6$ cm$/\sqrt{E}$ (E in GeV), mainly due to crystal segmentation. The EMC covers a range of $|cos\theta| < 0.83$ and $0.85 < |cos\theta| < 0.95$, with a poor performance transition region between these two areas.

The deposition of energy in the EMC is used to separate electrons from other stable charged particles. The stable charged particles that pass through the EMC are moving at relativistic speeds and thus are minimum ionizing particles that deposit a constant amount of energy in the EMC, independent of their momenta. Due to the small mass of the electron, Bremsstrahlung radiation causes electrons to lose energy proportional to their momenta. Heavier particles, such as muons and pions, are not subject to this form of energy loss and so they can be distinguished from electrons based on their energy loss in the EMC. A plot of EMC energy vs. momentum is shown in Figure 11.

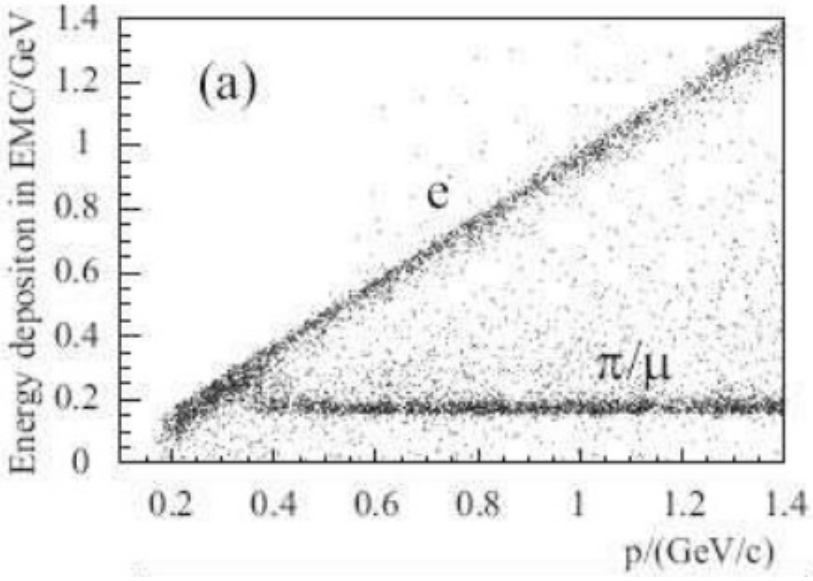

Figure 11: A scatter plot of the energy deposited in the EMC, described in Section 2.2.3, vs. momentum.

2.2.4 Muon Identifier

The final component of the detector is the Muon Identifier (MU) which is composed of resistive plate counters (RPC) interspersed between the steel plates of the magnetic flux return yolk of the superconducting solenoid. The purpose of the MU is to distinguish muons from pions and other hadrons. A muon is a charged lepton which interacts electromagnetically and weakly. Muons can penetrate farther into the MU than charged hadrons which are subject to strong interactions. Electrons will not penetrate into the MU because electrons are much lighter than muons and will shower and be absorbed upstream in the EMC. The barrel section of the MU has nine layers of steel plates with a total thickness of 41 cm. Nine total layers of RPCs are interspersed between the steel plates with one of the layers in front of the first steel layer. The end cap has eight layers of RPCs with the first layer of RPCs coming after 4 cm of steel.Because of the bending of the muon path due to the magnetic field, muon identification in the muon chamber only becomes useful for muons with momenta greater than 0.4 GeV/c.

2.3 Trigger System

The BESIII detector utilizes a two-tier trigger system to filter out background while maintaining high efficiency for physics events, illustrated in a block diagram in Figure 12. The main background is from beam-related sources like beam-gas and beam-wall interactions. Such backgrounds occcur at a rate of 13 MHz. Collimators and masks are utilized to keep lost electrons from interacting with the detector, but the trigger must help to filter these events further. The other source of background that the triggers suppress is cosmic rays which pass through the detector. The cosmic ray rate is about 1.5 kHz. The trigger system must suppress these backgrounds to a level that does not overwhelm the expected rate of physics events, which is about 2 kHz at the J/ψ peak and 600 Hz at the $\psi(3686)$ when run near peak luminosity. Bhabha events ($e^+e^- \to e^+e^-$) happen at a rate of 800 Hz within the detector acceptance, and pre-scaled Bhabha events are recorded for calibration and luminosity measurements. Expected event rates at the J/ψ peak at various points in the trigger process are summarized in Table 3.

The level 1 trigger decision is made with inputs from the MDC, ToF, and EMC subdetectors. This trigger is read out every clock cycle (24 ns) at a rate of 41.65 MHz. There is a 6.4 μs latency between the trigger signal and the event occurence, mainly due to the slow signal from the EMC, which has a 1 μs peaking and 3 μs decay time.

The MDC defines short and long tracks as tracks which have segments in superlayers

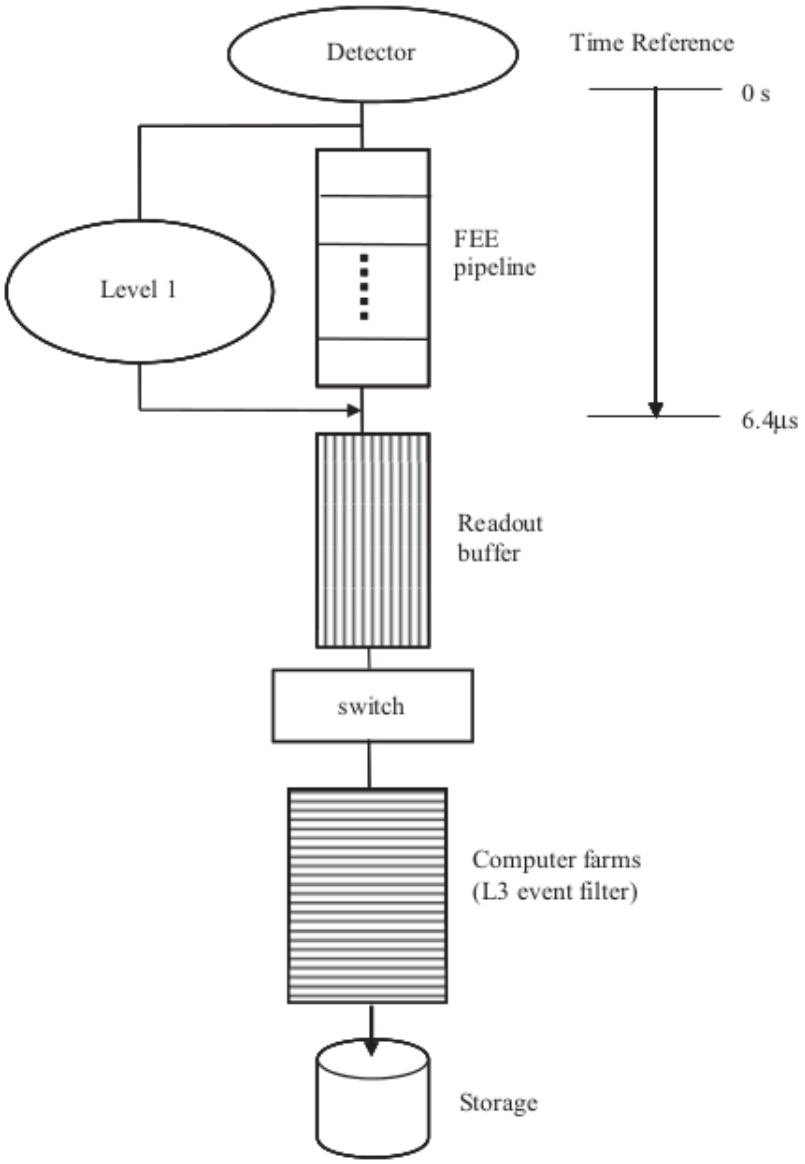

Figure 12: Block diagram of the BESIII trigger system described in Section 2.3.

Process	**Event Rate (kHz)**	**After L1 (kHz)**	**After L3 (kHz)**
Physics	2	2	2
Bhabha	0.8	Pre-scaled	Pre-scaled
Beam-related Background	$> 10^4$	< 2	< 1
Cosmic Ray Background	< 2	~ 0.2	~ 0.1
Total	$> 10^4$	4	3

Table 3: The rates of various backgrounds and signal at the J/ψ peak before and after filtering from the trigger system described in Section 2.3.

3-5 and in superlayers 3-5 and 10, respectively. A minimum transverse momentum cut is applied to these tracks to insure that the track has sufficient momentum to originate from the interaction point and reach the appropriate outermost superlayer while travelling in a 1 Tesla magnetic field. This cut is 90 MeV for short tracks and 120 MeV for long tracks. The number of short and long tracks, along with information on back-to-back tracks, is passed to the level 1 trigger to be used in conjunction with the ToF and EMC information.

The ToF passes on the number of hits in the barrel and end-cap regions, as well as information on back-to-back hits in the barrel and end cap ToF. The ToF must have hits within a range of 9 counters on the opposite side of the detector to be considered back-to-back.

The first step in determining the level 1 trigger information from the EMC is clustering. Clustering is the combining of nearby crystal energies around a local maximum-energy deposit in a crystal. The number of isolated clusters is sent on to the level 1 trigger along with back-to-back information for the barrel and end-cap EMC. The balance of energy in the ϕ direction within the barrel and the balance of energy in the z direction are also passed to the level 1 trigger.

Combining information from these three sub-detectors enables the trigger to reduce the rate of cosmic ray background to about 200 Hz and the beam-related background to 1.84 kHz. The maximum level 1 trigger rate is 4 kHz. When the data in the buffer is $\sim 80\%$ full, level 1 triggers are no longer generated until the buffer drops below 10% full, at which time trigger generation resumes. The level 1 trigger efficiencies are summarized in Table 4 for various processes.

Once a level 1 trigger is received, the electronics from all of the sub-detectors are read-out and the event is assembled in an online computer farm. This farm is responsible for the somewhat confusingly named level 3 software trigger. The background reduction for the level 3 trigger is fairly modest, taking a background rate of about 2 kHz and reducing it

Process	**Level 1 Trigger Efficiency (%)**
$J/\psi \to$ anything	97.66
$\psi(3686) \to$ anything	99.50
$\psi(3770) \to D\bar{D}$	99.90
$e^+e^- \to e^+e^-$	100
$e^+e^- \to e^+e^-\gamma$	100
Beam-related backgrounds	4.6×10^{-3}
Cosmic ray backgrounds	9.4

Table 4: The percent of events passing the level 1 trigger, described in Section 2.3 for various processes.

by half. Combined with a 2 kHz signal rate at the J/ψ peak, the level 3 trigger writes out events at about a 3 kHz rate. This corresponds to data being written to tape at a speed of 40 MB/s.

3 Software

The detector description, calibration, data reconstruction, Monte Carlo simulation and reconstruction, and analysis tools are implemented within the BESIII Offline Software System (BOSS) [38]. BOSS is an object-oriented framework written in C++ and designed to be run within a Scientific Linux CERN (SLC) operating system [39]. The BOSS framework is based on the Gaudi software architecture for data processing in high energy physics [40] and provides a standard interface for the software tools needed in data processing and analysis. The BOSS software is managed with the Configuration Management Tool (CMT) [41], which handles the dependencies between software packages, as well as creating the executables and the libraries from the source code and header files.

3.1 Reconstruction

The BOSS software takes the electronics readouts from the detector sub-systems and reconstructs them into events with objects which are useful for end-user analysis. The electronic readouts are combined with detector material and geometry descriptions saved in Geometry Design Markup Language (GDML) files [42], which are based on XML. After reconstructing objects from the various sub-detectors, the data is written out into Data Summary Tape (.dst) files using Gaudi conversion tools. These .dst files are written as ROOT [43] nTuples. ROOT is a C++ based language designed for performing physics analyses. This BOSS data-flow process is summarized in Figure 13.

3.1.1 MDC Reconstruction

The reconstruction in the MDC begins with finding track segments from the raw hits according to pre-calculated patterns. A least-squares method is then used to fit axial segments to circles. Once a circle has been identified from axial segments, stereo hits are added and the axial and stereo hits are fitted iteratively to the helix shape that represents a charged particle's path through a uniform magnetic field. A Kalman-filter process is then applied which refits using possible additional hits which were missed when reconstructing the seed track. The Kalman filter also reconstructs the tracks using hypotheses for the stable, charged particles (e, μ, π, K, p) which take into account differences in interactions between those particles and the detector material. For charged particles with transverse momentum greater than 150 MeV the reconstruction efficiency is quite high at 98%, even in high background environments.

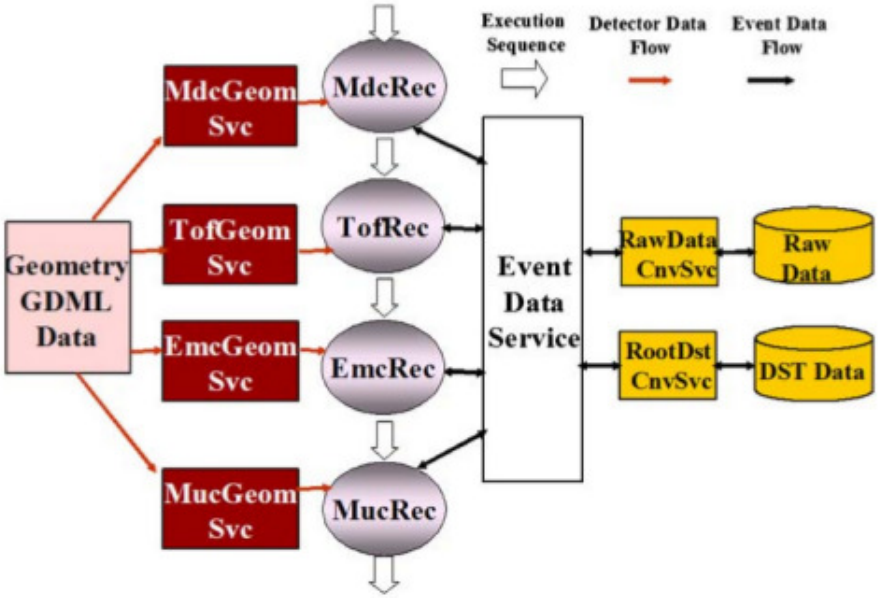

Figure 13: Representation of the BOSS data flow, described in Section 3.1.

Once the tracks have been reconstructed in the MDC, a GEANT4 based algorithm [44] extrapolates these tracks into the other detector sub-systems. The extrapolated path takes into account multiple scatterings, magnetic deflections, and ionization. The reconstructed tracks in the MDC are used to determine a particle's charge, momentum, and position. The dE/dx information from the hits along the track is used in conjunction with ToF information to provide Particle Identification.

3.1.2 ToF Reconstruction

The ToF sub-system matches the extrapolated paths of charged particles in the MDC with hits in the two layers of barrel ToF, or single-layer end-cap ToF. Using the information provided from the MDC about the particle's momentum and flight path, the ToF time measurements are used to discriminate between the charged particle hypotheses. The χ^2_{ToF} of the time measurement for the various particle hypotheses is combined with the MDC dE/dx χ^2_{MDC} to calculate the probability of that particle hypothesis. Energy deposited in the ToF is also added back into the energy from the EMC for showers that started in the ToF.

3.1.3 EMC Reconstruction

EMC reconstruction begins with conversion of the analog readout signals from EMC crystals into true energies using calibration files. Then a clustering algorithm is used which groups related hits from nearby crystals around a local maximum energy deposit in a crystal. These are used as the shower seeds. The energy of a shower is computed from the sum of the energies deposited in the crystals for that cluster and, if necessary, includes energy from the ToF system. The position of the shower is calculated using the energy-weighted first moments. Extrapolations from charged tracks in the MDC determine whether an EMC shower is presumed to be from a photon or should be associated with a charged track.

3.1.4 MU Reconstruction

Reconstruction in the Muon Chamber is fairly minimal, and is mainly used to see how far a particle penetrates from the interaction point to separate muons from other charged particles. The MU looks for hit matches along the axial and transverse wires and combines these into tracks. These tracks are then compared with the extrapolated positions from MDC tracks to see whether the MU hits should be associated with an MDC track or not.

3.2 Database

BESIII uses a MySQL [45] database to store information on individual runs, such as the beam energy, luminosity, data-taking status, trigger conditions, magnetic field information, and the software version. The location of files used to calibrate the sub-systems is also found within the database, among other things. The information in the database is important for both reconstruction and accurate Monte Carlo simulation. The database is distributed to off-site locations via a reduced SQLite version, or in full via an ssh-tunnel to the on-site database. The University of Minnesota maintains an active ssh-tunnel to completely reproduce the database and utilizes a proxy configuration to distribute the database calls among three local machines to meet the high demands of the University of Minnesota BESIII computer farm.

3.3 Monte Carlo Simulation

Useful Monte Carlo simulations depend on a good model of the physics being generated, described in Section 3.4, an accurate propagation of the physics event through the detector, and a realistic detector response to the particles generated. The BESIII Object Oriented

Simulation Tool (BOOST) [46] is based on GEANT4 [44], the standard framework for simulating detector response in high energy physics. BOOST handles the propagation of the particles through the detector and their interactions with detector materials, which are described in the GDML files mentioned in Section 3.1. Physics processes are generated in the center-of-mass system and boosted outside of the generator framework to account for the small ($\sim$ 11 mrad) crossing angle of the electron and positron beams. The detector response-digitization code is responsible for translating the interactions between particles and detector material into electronic readout similar to what would be obtained from true data. Random electronic noise is also added into the simulations during reconstruction by utilizing random-trigger files. Random-trigger files are files containing detector readout during the dead-time when e^+ and e^- are known not to be in collision. The location of random-trigger files is accessed via the database. Simulations are done on a per-run basis to reflect the same running conditions as the physical run. Beam energy, magnetic field conditions, and random-triggers are obtained from the database and inserted into the scripts used to generate Monte Carlo. The University of Minnesota also generates runs such that their number of events generated is proportional to the integrated luminosity of that run taken from the database.

3.4 Monte Carlo Generators

3.4.1 KKMC

The KKMC generator [47], originally developed for the LEP and SLC colliders, is used to model Standard Model electroweak interactions and generates processes of the form $e^+e^- \to f\bar{f}$+nγ, where $f = \mu, \tau, u, d, s, c, b$. KKMC takes into account second-order subleading corrections. Initial-state radiation and interference between initial-state and final-state radiation are modelled by KKMC. The effects of beam energy spread, $\sim$ 1 MeV at the $\psi(3770)$ energy, are also included by KKMC. Two hard photons are modelled using exact matrix elements.

The fermion/anti-fermion pair is then decayed with different models, depending on the fermion. For $\tau\bar{\tau}$, the TAUOLA [48] library is used which takes into account spin-polarization effects. The PYTHIA [49] model is used to hadronize final-state $q\bar{q}$ continuum with the parton shower model. For resonance production, in our case $\psi(3770)$, KKMC is used to generate intial-state radiation, and then hands off a virtual photon to be decayed by the BesEvtGen generator described below.

3.4.2 BesEvtGen

The BesEvtGen generator [50] is based on EvtGen [51], which was originally developed for the CLEO and BaBar programs. The strength of BesEvtGen is its incorporation of many different decay models into a single package. Over 30 models for exclusive decays are available in BesEvtGen, in addition to the ability to easily incorporate user-created decay models. BesEvtGen sequentially decays particles with dynamic information based on amplitude probability and forward/backward spin-density matrix information. The final-state radiation of particles is handled by the PHOTOS [52] model. The LundCharm [53] model is used to generate unknown decays of charmonium resonances, while PYTHIA [49] takes care of other unknown hadronic decays.

We use the BesEvtGen model along with KKMC to generate direct resonance production of $\psi(3770)$. BesEvtGen is used with the VECTORISR [51] model to generate radiative return to the J/ψ and $\psi(3686)$. This process occurs when the e^+ or e^- in the initial state radiates a photon such that the center-of-mass energy of the e^+e^- system is able to produce a lower mass resonance.

3.4.3 Babayaga

Babayaga [54] is a precision QED generator which we use to generate $e^+e^- \to e^+e^-, \mu^+\mu^-$, and $\gamma\gamma$. Babayaga matches exact next-leading order corrections with a parton shower algorithm. Babayaga has an estimated theoretical accuracy of 0.1% and is used to determine efficiencies and acceptances for measuring the integrated luminosity of BESIII data samples. For more details on the Monte Carlo generators used at BESIII, see Ref. [55].

4 Method for Measuring $\mathcal{B}(\psi(3770) \to non - D\bar{D})$

To measure the branching fraction of $\psi(3770) \to non - D\bar{D}$, we use

$$\mathcal{B}(\psi(3770) \to non - D\bar{D}) = \frac{\sigma_{non-D\bar{D}}}{\sigma_{\psi(3770)}}, \tag{6}$$

where the σs are the corresponding cross sections obtained from

$$\sigma_{non-D\bar{D}} = \frac{N_{non-D\bar{D}}}{\mathcal{L}^{3.773}\epsilon_{non-D\bar{D}}} \text{ and } \sigma_{\psi(3770)} = \frac{N_{\psi(3770)}}{\mathcal{L}^{3.773}\epsilon_{\psi(3770)}}, \tag{7}$$

the $N_{non-D\bar{D}}$ and $N_{\psi(3770)}$ are the observed numbers of such events, $\mathcal{L}^{3.773}$ is the integrated luminosity of the data taken at 3.773 GeV (the peak of the $\psi(3770)$ resonance) described in Section 5, and the ϵs are the efficiencies of such events passing hadronic event selection cuts, described in Section 7.1. Non-$D\bar{D}$ events are assumed to be similar to $\psi(3686)$ decays, and so the efficiency is estimated by the efficiency of radiative return to $\psi(3686)$ events at the 3.773 GeV energy point. Because $\psi(3770)$ events include both $D\bar{D}$ and non-$D\bar{D}$ events, the overall efficiency is given by

$$\epsilon_{\psi(3770)} = \frac{\sigma_{D\bar{D}}\epsilon_{D\bar{D}} + (\sigma_{\psi(3770)} - \sigma_{D\bar{D}})\epsilon_{non-D\bar{D}}}{\sigma_{\psi(3770)}}. \tag{8}$$

The determination of the $D\bar{D}$ cross section $\sigma_{D\bar{D}}$ is described in Section 6. The hadronic event selection efficiency for $D\bar{D}$ events is taken from Monte Carlo. Combining Equation 7 and Equation 8 gives the $\psi(3770)$ cross section as

$$\sigma_{\psi(3770)} = \sigma_{D\bar{D}} + \frac{\frac{N_{\psi(3770)}}{\mathcal{L}^{3.773}} - \sigma_{D\bar{D}}\epsilon_{D\bar{D}}}{\epsilon_{non-D\bar{D}}}. \tag{9}$$

The measurement of the cross section for hadronic events is described in Section 7. To measure the uncorrected number of hadronic events from the $\psi(3770)$ resonance, $N_{\psi(3770)}$, we find the total number of hadronic events at the 3.773 GeV energy point using hadronic event selection cuts and a fit to the average vertex distribution of the events to remove backgrounds that are not from beam-beam interactions, and then subtract off the various other backgrounds: $q\bar{q}$, $l\bar{l}(l = e, \mu, \tau)$, $\gamma\gamma$, two-photon fusion ($e^+e^- \to e^+e^- f\bar{f}$, where f is a quark or lepton), radiative return to $\psi(3686)$, and radiative return to J/ψ, using

$$\begin{aligned} N_{\psi(3770)} = N_{had}^{3.773} \\ -(N_{q\bar{q}}^{3.773} + N_{e\bar{e}}^{3.773} + N_{\mu\bar{\mu}}^{3.773} + N_{\gamma\gamma}^{3.773} + N_{2\gamma-fus}^{3.773}) \\ -N_{\tau\bar{\tau}}^{3.773} - N_{\gamma\psi(3686)}^{3.773} - N_{\gamma J/\psi}^{3.773}. \end{aligned} \tag{10}$$

The $\tau\bar{\tau}$, radiative return to J/ψ, and radiative return to $\psi(3686)$ backgrounds are estimated from Monte Carlo, while the remaining backgrounds all follow $\frac{1}{s}$ energy dependence and are estimated from data taken at 3.65 GeV. Despite also following $\frac{1}{s}$ energy dependence, the $\tau\bar{\tau}$ background is not included in the data-driven subtraction because some of the extrapolation points lie below the $\tau\bar{\tau}$-threshold, while other points are above it.

The non-$\tau\bar{\tau}$ $\frac{1}{s}$ backgrounds are determined from a measurement at 3.65 GeV and scaled with relative efficiency, integrated luminosity, and $\frac{1}{s}$ to the 3.773 GeV energy point with the equation

$$\begin{aligned} (N_{q\bar{q}}^{3.773} + N_{e\bar{e}}^{3.773} + N_{\mu\bar{\mu}}^{3.773} + N_{\gamma\gamma}^{3.773} + N_{2\gamma-fus}^{3.773}) = \\ (N_{had}^{3.65} - N_{\tau\bar{\tau}}^{3.65} - N_{\psi(3686)}^{3.65} - N_{\gamma J/\psi}^{3.65}) \frac{\epsilon(3.773)}{\epsilon(3.65)} \frac{\mathcal{L}^{3.773}}{\mathcal{L}^{3.65}} \frac{3.65^2}{3.773^2}, \end{aligned} \tag{11}$$

where the $N^{3.65}$ quantities are determined with the 2009 data at 3.65 GeV in the same way as the $N^{3.773}$ quantities are with their respective data sets. The ratio of efficiencies, $\frac{\epsilon(3.773)}{\epsilon(3.65)}$, is determined via fit extrapolation, described in Section 7.4, using the five continuum energy points taken in 2013, and scaling to the absolute efficiency of the data taken at 3.65 GeV in 2009. The energy dependence is believed to be run-period independent while the absolute efficiency is not.

To determine the number of non-$D\bar{D}$ events, we subtract the number of $D\bar{D}$ events passing hadronic event selection cuts from the number of $\psi(3770)$ hadronic events,

$$N_{non-D\bar{D}} = N_{\psi(3770)} - N_{D\bar{D}}\epsilon_{D\bar{D}}. \tag{12}$$

5 Data and MC Samples and Software Versions

This analysis uses the folowing data and Monte Carlo samples:

1. Data

   928 pb^{-1} taken at 3.773 GeV during 2010, runs 11414-13988 and 14395-14604. Used in the initial un-blind analysis and referred to in this paper as the first round of $\psi(3770)$ data.

   1989 pb^{-1} taken at 3.773 GeV during 2011, runs 20448-23454, referred to as the second round of $\psi(3770)$ data.

   44.5 pb^{-1} taken at 3.65 GeV during 2009, runs 9613-9779. Used to determine a data-driven background subtraction of $q\bar{q}$ at the 3.773 GeV energy point.

   Continuum data taken at five energy points during July 2013, runs 33725-33772, to be used in the fit extrapolation of hadronic event selection efficiency: 3.7 pb^{-1} at 3.5 GeV, 4.5 pb^{-1} at 3.542 GeV, 0.4 pb^{-1} at 3.6 GeV, 5.4 pb^{-1} at 3.65 GeV, and 4.7 pb^{-1} at 3.671 GeV. Details for calculating the integrated luminosity of these points are given in Section 7.4.3.

2. Monte Carlo

   Monte Carlo samples were produced at the University of Minnesota corresponding to the 3.773 GeV data sets taken in 2010 and 2011. For each of the physics processes listed, two Monte Carlo samples each of approximately 10$\times$ data-size were produced: generic $D^0\bar{D}^0$ from $\psi(3770)$, generic D^+D^- from $\psi(3770)$, $q\bar{q}$, $\tau\bar{\tau}$, radiative return to $\psi(3686)$, and radiative return to J/ψ. Two 15 million event non-$D\bar{D}$ samples were also generated, as well as approximately 1 million event samples for $e\bar{e}$, $\mu\bar{\mu}$ and $\gamma\gamma$.

   Approximately 1-million-event samples were generated at the University of Minnesota, corresponding to the six continuum data points taken during 2009 and 2013 for the following processes (where energetically appropriate): $q\bar{q}$, radiative return to J/ψ, $e\bar{e}$, $\mu\bar{\mu}$, $\tau\bar{\tau}$, and $\gamma\gamma$.

   For the $D\bar{D}$ and non-$D\bar{D}$ Monte Carlo samples, initial state radiation was handled via the KKMC generator [47], and the particles were subsequently decayed with EvtGen [51] according to world average branching fractions from the PDG. The remaining events associated with charmonium decays are generated with Lundcharm [53], while other hadronic events are generated with PYTHIA [49]. For unmeasured decays, the

non-$D\bar{D}$ sample was decayed similarly to $\psi(3686)$. The radiative return samples were also generated with the EvtGen generator. The $q\bar{q}$ and $\tau\bar{\tau}$ samples were generated with KKMC. A $q\bar{q}$ sample generated with EvtGen using the LUNDA model was also used for diagnostic purposes, but did not contribute to the final analysis. $e\bar{e}$, $\mu\bar{\mu}$, and $\gamma\gamma$ were all generated with Babayaga [54].

3. BOSS version 6.6.2 is used to reconstruct data and MC, and to simulate MC for the 2009-2011 data sets. BOSS version 6.6.3.p01 is used to reconstruct data and MC, and to simulate MC for the 2013 continuum data points. The following packages are also utilized:

   DTagAlg-00-00-49 to reconstruct D-tags

   Customized DTagTool-00-00-09 to provide useful functions for interacting with D-tags

   SimplePIDSvc-00-00-06 for particle identification

   Pi0EtaToGGRecAlg-00-00-09 for π^0 reconstruction

6 $\sigma_{D\bar{D}}$ Measurement

6.1 Introduction to D-Tagging

When the $\psi(3770)$ decays into a D meson, a $\bar{D}$ meson is always produced. This is because when a $\psi(3770)$ decays to $D\bar{D}$, a quark and anti-quark pair (either a $u\bar{u}$ pair for neutral D or $d\bar{d}$ in the case of charged D) are produced from the vacuum and pair with the $\bar{c}$ and c quarks of the $\psi(3770)$, respectively, to produce a $\bar{D}$ and D meson pair and there is insufficient energy to produce additional particles. To select the $D\bar{D}$ events, we fully reconstruct a D using one of nine "tag modes" that are common and easily reconstructable D-decay single-tag modes (3 for neutral $D/\bar{D}^0$, and 6 for charged D^+/D^-). Similarly, the entire $D\bar{D}$ event can be reconstructed as a double tag by taking any two single-tag modes of opposite net charge, opposite-charm D parents, and no common tracks between them. The "D-Tagging" technique was pioneered by MARK-III [56, 57], utilized by CLEO-c, and is now used by BESIII. The decay modes that will be used in this analysis are $D^0 \to K^-\pi^+$, $D^0 \to K^-\pi^+\pi^0$, $D^0 \to K^-\pi^+\pi^+\pi^-$, $D^+ \to K^-\pi^+\pi^+$, $D^+ \to K^-\pi^+\pi^+\pi^0$, $D^+ \to K^0_s\pi^+$, $D^+ \to K^0_s\pi^+\pi^0$, $D^+ \to K^0_s\pi^+\pi^+\pi^-$, and $D^+ \to K^-K^+\pi^+$, and their charge conjugates. Charge conjugate modes are implied throughout this paper. The exclusive branching fraction measurements of the $D^0 \to K^-\pi^+\pi^+\pi^-$ and $D^+ \to K^0_s\pi^+\pi^+\pi^-$ modes usually reject or treat as peaking background oppositely charged pion pairs originating from a K_s (except the K_s being explicitly reconstructed). However, in our measurement, there is no reason to distinguish between final-state charged pion pairs from a K_s and those from other sources, so we treat such decays as signal.

6.2 D-Tagging Selection Requirements

All of the particles used to construct the D-Tag candidate must pass cuts specific to that particle type. A "track" is the reconstructed path of a charged particle within the detector and is the object that is subjected to the various cuts. Track and reconstructed particle selection cuts are taken from the BESIII DTag Note [58].

6.2.1 K^+/K^- and π^+/π^- Selection

All reconstructed charged tracks are required to pass within 1 cm of the interaction point (determined run by run) in the plane transverse to the beam-direction, and within 10 cm in the direction of the beam-axis. They also must have $|cos\theta| < 0.93$, where θ is the polar angle measured in the drift chamber. Particle identification is determined from ToF and

dE/dx measurements using SimplePIDSvc. We require Prob(K) > Prob(π) for kaon and Prob(π) > Prob(K) for pion identification.

6.2.2 K_s^0 Selection

A K_s^0 meson is reconstructed from its decay into a pair of oppositely charged pions, which happens 69.2% [3] of the time. These pions are not required to pass particle identification cuts nor the standard interaction point cuts for pions, because the K_s^0 decays in flight. These pions are kinematically constrained to a common vertex. The fitted K_s^0 mass must be within $\sim 3\sigma$ of the nominal K_s^0 mass ($487 - 511$ MeV), and the fit must converge and have $\chi^2 < 100$. The momentum of the K_s^0 obtained from the vertex fit is used for the subsequent reconstruction of the D-tag candidate.

6.2.3 Photon Selection

Photons are required to have a minimum energy of 25 MeV in the barrel region ($|cos\theta| < 0.8$), and of 50 MeV in the end cap region ($0.84 < |cos\theta| < 0.92$). This is done to help separate real photons from noise in the EMC. Photons must pass a TDC timing cut ($time < 14 \cdot 50$ ns) to insure that they are consistent with originating from a physics event.

6.2.4 π^0 Selection

A π^0 meson is reconstructed from its decay into two photons, which happens 98.8% [3] of the time. These photons must also pass the above photon cuts, and at least one of the photons must be in the barrel region of the detector. The π^0 mesons must be within the mass range from 115 MeV to 150 MeV, and the kinematic fit of the photons' momenta to the π^0 invariant mass must converge and have a $\chi^2 < 200$. The π^0 momentum components from the kinematic fit are used in the reconstruction of the D-tag candidates.

6.2.5 Cuts on the Reconstructed D-Tag

As well as the restrictions on the particles that constitute the D-tag, the reconstructed D-tag must also pass additional cuts.

1. The energy difference $\Delta E = E_D - E_{beam}$ must be consistent with zero, where E_D is the energy of the reconstructed D candidate, and E_{beam} is the beam energy, determined run-by-run. The ΔE cuts are $\pm 3\sigma$ about the mean and vary by mode as well as between data and MC due to differing resolutions. For modes with a π^0, the cuts

are asymmetric about the mean and extend down to -4σ, due to a long low-side tail from photon reconstruction. The ΔE cuts are taken from the BESIII DTag Note [58] and are reproduced in Table 5. Figure 15 shows the data/MC overlays of the ΔE distribution by mode. The ΔE cut requires that the D-Tag candidate have the right energy for production through $\psi(3770) \to D\bar{D}$.

2. The beam-constrained mass is $m_{BC}c^2 = \sqrt{E_{beam}^2 - |\mathbf{p}_{tag}c|^2}$, where $\mathbf{p}_{tag}$ is the 3-momentum of the candidate D-tag. The m_{BC} is the variable used in the fits, described in Sections 6.4 and 6.5, to determine signal yields. A wide cut between 1.83 and 1.89 GeV is initially imposed, and after the fit a mode-dependent cut is applied so that the m_{BC} is consistent with the mass of the D. The beam-constrained mass is used instead of the invariant mass of the D-tag because the beam energy is known to a much greater precision than the energy of the particles composing the D-tag. The beam-constrained mass cut effectively constrains the D-tag candidate to have the correct momentum. Additionally, a small shift upward of just under 1 MeV is made to the D-momentum used to calculate the m_{BC} in Monte Carlo to give better agreement with data. In practice, the fits described in Section 6.4 have enough freedom to accommodate this even if this shift were not applied.

3. For the selection of single-tag candidates, a best candidate is chosen per mode, per charm, per event based on the lowest $|\Delta E|$.

4. For the selection of double-tag candidates, the best candidate per mode combination per event is chosen based on the $\frac{m_{BC1}+m_{BC2}}{2}$ most consistent with the nominal D mass.

5. For the $D^0 \to K^-\pi^+$ single-tag mode, an additional set of cuts is used to reject backgrounds from cosmic ray and QED events. These backgrounds have only two charged tracks, and thus only events tagged as $K^-\pi^+$ single tags are susceptible to these backgrounds. An event is vetoed if there are exactly two charged tracks that pass the cuts, besides PID, described in Section 6.2.1 and at least one of the following conditions is satisfied:

   (a) Both particles have valid ToF information, and the difference between their times is greater than 5 units.

   (b) If the combined χ^2 from SimplePIDSvc comparing the two-particle $K^-\pi^+$ hypothesis to the e^-e^+ hypothesis satisfies $\chi^2_{K^-} - \chi^2_{e^-} + \chi^2_{\pi^+} - \chi^2_{e^+} > -10$.

(c) Both tracks have EMC energy divided by momentum greater than 0.8.

(d) There are no EMC showers not associated with charged tracks with energy greater than 50 MeV and either track is consistent with being a muon. A track is designated as a muon if its EMC energy is between 150 and 300 MeV, its depth in the MUC is greater than 40 or greater than or equal to $80 \cdot |p| - 40$, where $|p|$ is its momentum in GeV, and its MdcDedx χ^2_μ is less than 5.

Figure 14 shows the m_{BC} distribution of events before and after this veto, as well as the m_{BC} distribution of vetoed events.

	MC		**Data**	
Tag Mode	**Error (MeV)**	**Mean (MeV)**	**Error (MeV)**	**Mean (MeV)**
$D^0 \to K^-\pi^+$	7.6	-0.4	9.4	-0.8
$D^0 \to K^-\pi^+\pi^0$	14.1	-7.6	15.4	-7.6
$D^0 \to K^-\pi^+\pi^+\pi^-$	8.2	-1.4	9.8	-2
$D^+ \to K^-\pi^+\pi^+$	7.2	-0.9	8.6	-1.2
$D^+ \to K^-\pi^+\pi^+\pi^0$	12.8	-6.9	13.7	-6.9
$D^+ \to K^0_s\pi^+$	6.7	0.4	8.4	-0.1
$D^+ \to K^0_s\pi^+\pi^0$	14.6	-7.7	16.2	-7.9
$D^+ \to K^0_s\pi^+\pi^+\pi^-$	8.2	-1.1	10.4	-1.7
$D^+ \to K^+K^-\pi^+$	6.2	-1.1	7.2	-1.5

Table 5: The cut on ΔE is $\pm 3\sigma$ about the mean, except that for modes with a π^0 an extended lower bound of -4σ is used. The resolution and mean are determined separately for data and Monte Carlo, and are taken from [58].

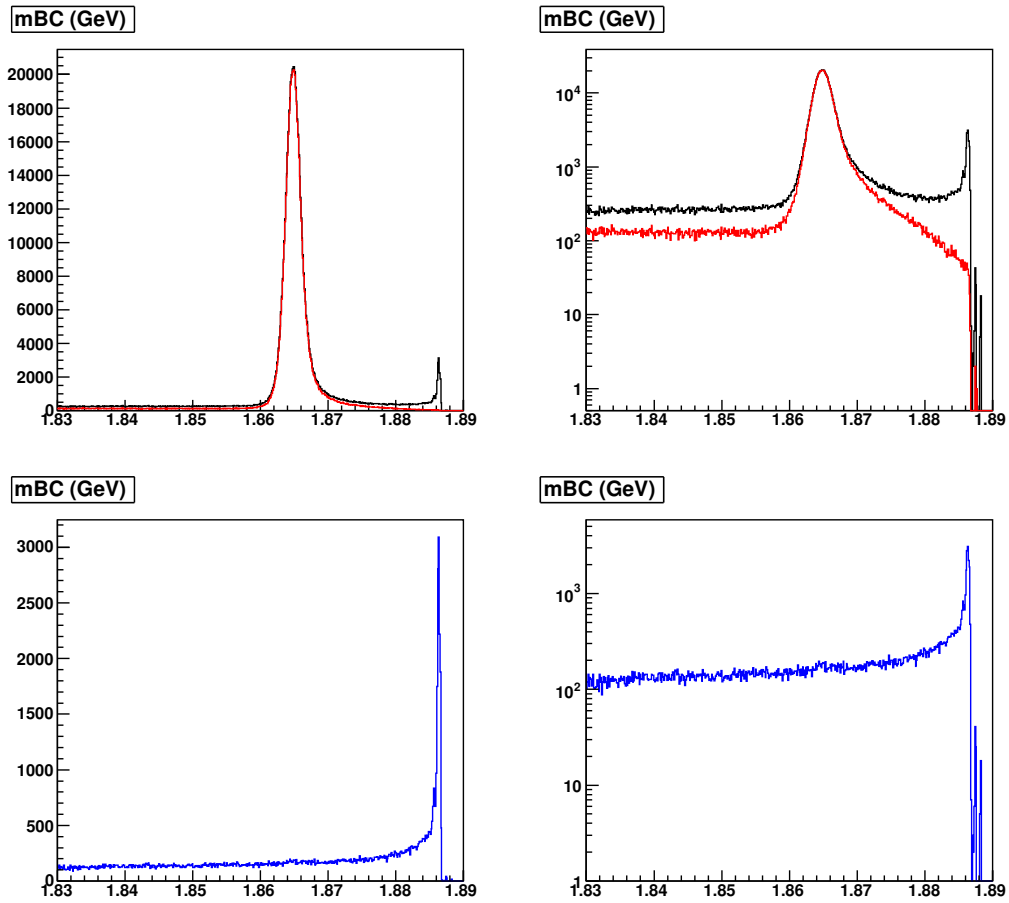

Figure 14: Plot of m_{BC} for decay mode $K^-\pi^+$, overlaying data with and without the cosmic and lepton veto, with linear scale on the left and a log scale on the right. The bottom plots show the vetoed events, demonstrating a very high cut efficiency, and almost no loss of signal events.

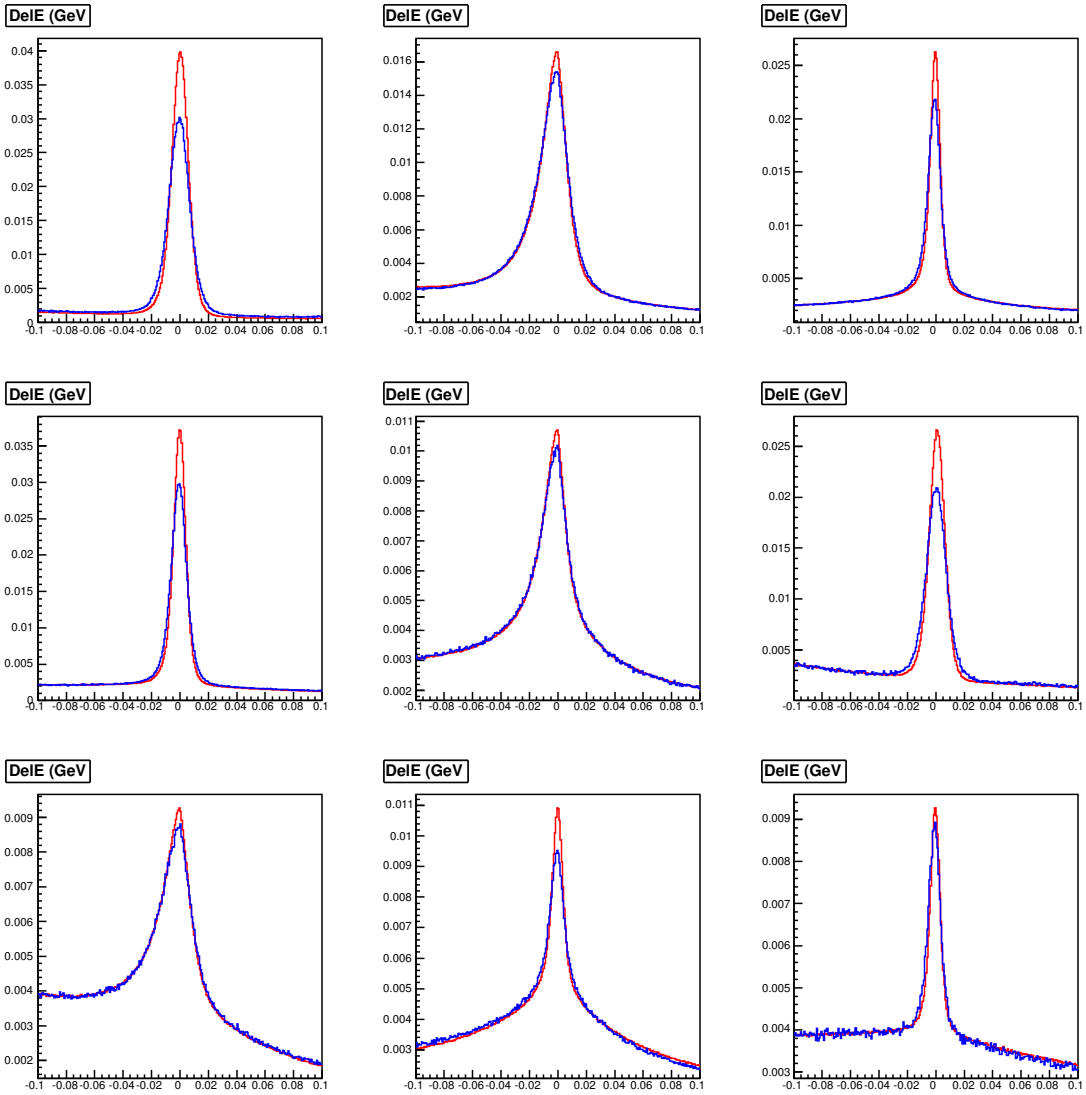

Figure 15: ΔE by mode. Starting from the top left, the modes are: $D^0 \to K^-\pi^+, D^0 \to K^-\pi^+\pi^0, D^0 \to K^-\pi^+\pi^+\pi^-, D^+ \to K^-\pi^+\pi^+$, $D^+ \to K^-\pi^+\pi^+\pi^0$, $D^+ \to K^0_s\pi^+$, $D^+ \to K^0_s\pi^+\pi^0$, $D^+ \to K^0_s\pi^+\pi^+\pi^-$, and $D^+ \to K^+K^-\pi^+$. These plots overlay the 3.773 data and the corresponding, narrower width MC as described in Section 5. Only cuts on the constituent particles and a very loose m_{BC} cut (1.83 GeV $\leq m_{BC} \leq$ 1.89 GeV) have been applied.

6.3 Calculating $\sigma_{D\bar{D}}$

The yield, X_i, for single-tag mode i is determined via the equation

$$X_i = N_{D\bar{D}} \cdot \mathcal{B}(D \to i) \cdot \epsilon_i, \tag{13}$$

where $N_{D\bar{D}}$ is the total number of $D\bar{D}$ events, $\mathcal{B}(D \to i)$ is the branching fraction of this decay mode, and ϵ_i is the reconstruction efficiency of this single-tag mode determined from Monte Carlo. A similar equation

$$Y_j = N_{D\bar{D}} \cdot \mathcal{B}(\bar{D} \to j) \cdot \epsilon_j \tag{14}$$

applies for $\bar{D}$ decaying to mode j. For reconstruction of a double-tag mode, where the D decays to mode i and the $\bar{D}$ decays to mode j, the following equation holds:

$$Z_{ij} = N_{D\bar{D}} \cdot \mathcal{B}(D \to i) \cdot \mathcal{B}(\bar{D} \to j) \cdot \epsilon_{ij}, \tag{15}$$

where ϵ_{ij}, and Z_{ij} are the efficiency and yield of the double-tag mode ij, respectively. Using these equations and algebra, $N_{D\bar{D}}$ can then be calculated as

$$N_{D\bar{D}} = \frac{X_i \cdot Y_j \cdot \epsilon_{ij}}{Z_{ij} \cdot \epsilon_i \cdot \epsilon_j}. \tag{16}$$

This method is chosen over a measurement of $N_{D\bar{D}}$ via the single-tag Equations 13 and 14 above because a ratio of Monte Carlo efficiencies is used, thus lessening the systematic dependence on Monte Carlo, although with an accompanying loss of statistics due to the double-tag meausurement. However, as this is a systematics limited measurement, this is optimal.

Finally, to determine the cross section we divide $N_{D\bar{D}}$ by the integrated luminosity of the $\psi(3770)$ sample [59], $\sigma_{D\bar{D}} = \frac{N_{D\bar{D}}}{\mathcal{L}}$.

6.4 Single-tag Yield and Efficiency Extraction

The single-tag yields are determined via a cut-and-count method. The m_{BC} distribution from data is fitted between 1.83 and 1.89 GeV with a Monte-Carlo-derived signal-shape and an ARGUS function background [60]. The signal-shape is convolved with a double Gaussian with a common mean, to allow for differences in m_{BC} resolution between data and Monte Carlo. Charm-conjugate modes are fitted simultaneously with the double-Gaussian signal-shape parameters constrained, and the normalizations and background parameters allowed

to float independently. This is done to limit the double-Gaussian parameters while still allowing freedom in the background fit.

The Monte Carlo truth-shape is determined by truth-tagging signal events to insure that the correct tag mode has been reconstructed. The reconstructed particles must match with the PDG code of the generated particles, and all particles must share a common D parent. Peaking backgrounds, contributed by decay modes that have similar final states to the signal mode, are similarly truth-tagged and included in the signal-shape, although the yields are corrected after the fit to count only true signal events. This shape is then convolved with a double Gaussian with a common mean and floating widths and fraction of events in each Gaussian. The signal-shape is obtained from an approximately $10\times$ data-size generic Monte Carlo sample, described in Section 5.

The signal-shape is used in conjunction with a background ARGUS function that models combinatoric background in a reconstructed invariant mass distribution, including a cut-off due to a kinematic limit. The ARGUS function is defined as

$$ARGUS(m_{BC}; c, p, m_0) = m_{BC} e^{c(1-(\frac{m_{BC}}{m_0})^2)} (1 - (\frac{m_{BC}}{m_0})^2)^p. \quad (17)$$

The c and p parameters represent the slope and power, respectively, and m_0 represents the kinematic cut-off, in this case E_{beam}. m_0 is held constant in our fits, because it is well known and allowing it to float causes the fits to have problems with convergence. An example m_{BC} fit with details is shown in Figure 16 and all fits used to measure single-tag yields and efficiencies are shown in Figures 17-20, and summarized in Table 6. The fits in Figures 17-20 have the same parameters that are fixed and floated as the fit in Figure 16, but the shape parameters have been suppressed in the outputs for easier viewing of the fits.

After the fit has been performed, the m_{BC} histogram is integrated within the signal region, 1.858 GeV $\leq m_{BC} \leq$ 1.874 GeV for D^0 modes and 1.8628 GeV $\leq m_{BC} \leq$ 1.8788 GeV for D^+ modes, and then the analytic integral of the ARGUS function in this region is subtracted off. Finally, this number is multiplied by the fraction of true signal events in the signal-shape to correct for peaking backgrounds, discussed in more detail in Section 6.6.

Single-tag efficiency numerators are found using the same cut-and-count method as data on an independent, $\sim 10\times$ data-size Monte Carlo sample including generic $D\bar{D}$ decays and backgrounds, as listed in Section 5. Although convolving the signal shape with a double-Gaussian is unnecessary to reproduce the resolution when fitting to Monte Carlo, the convolution is still performed so the Monte Carlo fits will have the same freedom as fits to data. Fits to Monte Carlo typically have $> 98\%$ of their double-Gaussian components

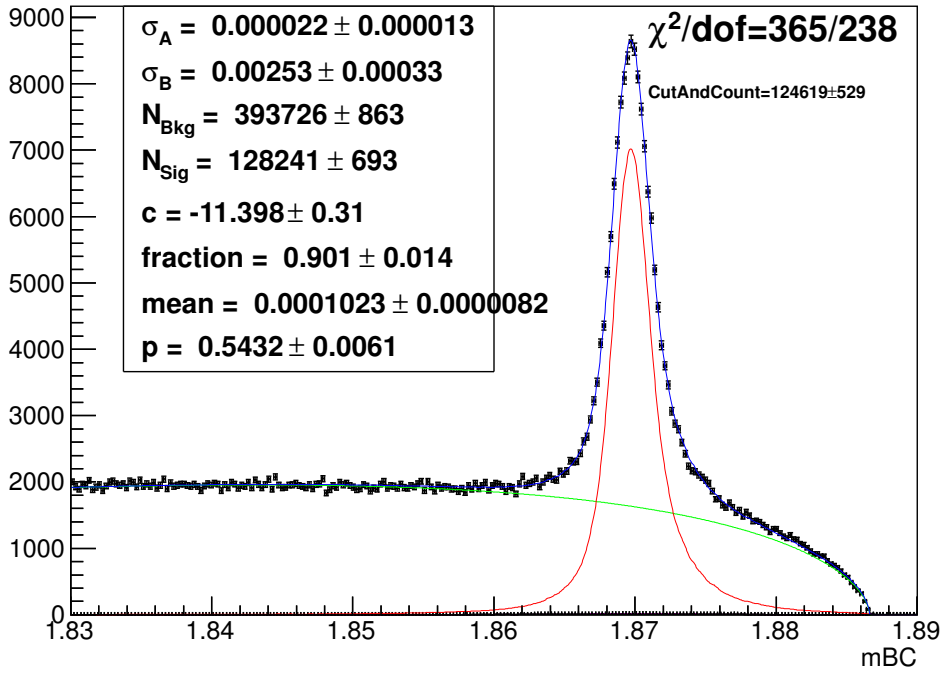

Figure 16: m_{BC} fit for tag-mode $D^+ \to K^-\pi^+\pi^+\pi^0$, from data, as detailed in Section 6.4.

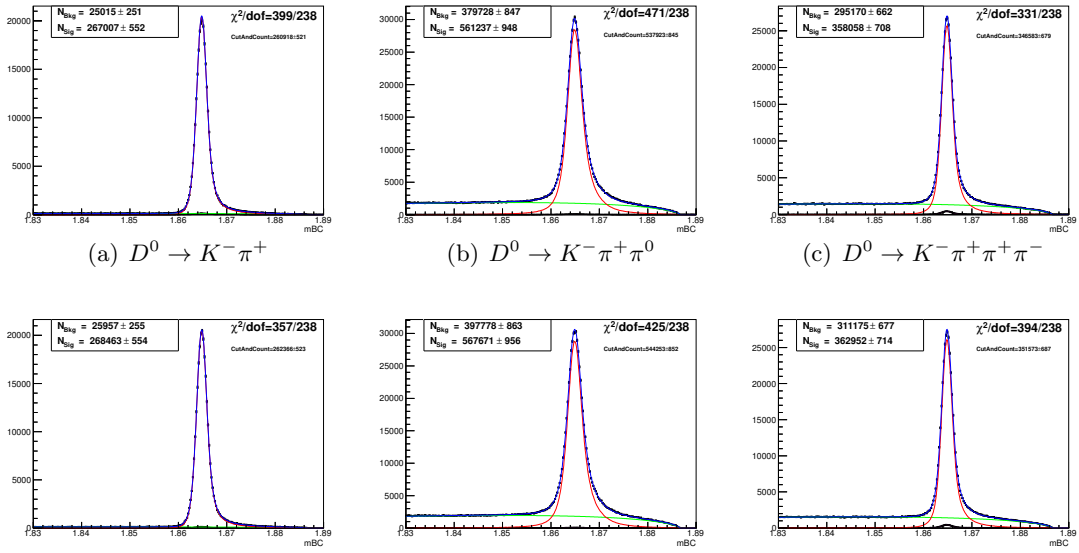

(a) $D^0 \to K^-\pi^+$ (b) $D^0 \to K^-\pi^+\pi^0$ (c) $D^0 \to K^-\pi^+\pi^+\pi^-$

(d) $\bar{D}^0 \to K^+\pi^-$ (e) $\bar{D}^0 \to K^+\pi^-\pi^0$ (f) $\bar{D}^0 \to K^+\pi^+\pi^-\pi^-$

Figure 17: m_{BC} fits, from data, for neutral D modes, as detailed in Section 6.4.

in the Gaussian with a width of approximately zero, bearing out that this convolution is not significant when fitting Monte Carlo. The denominators are calculated from the truth information for these MC samples.

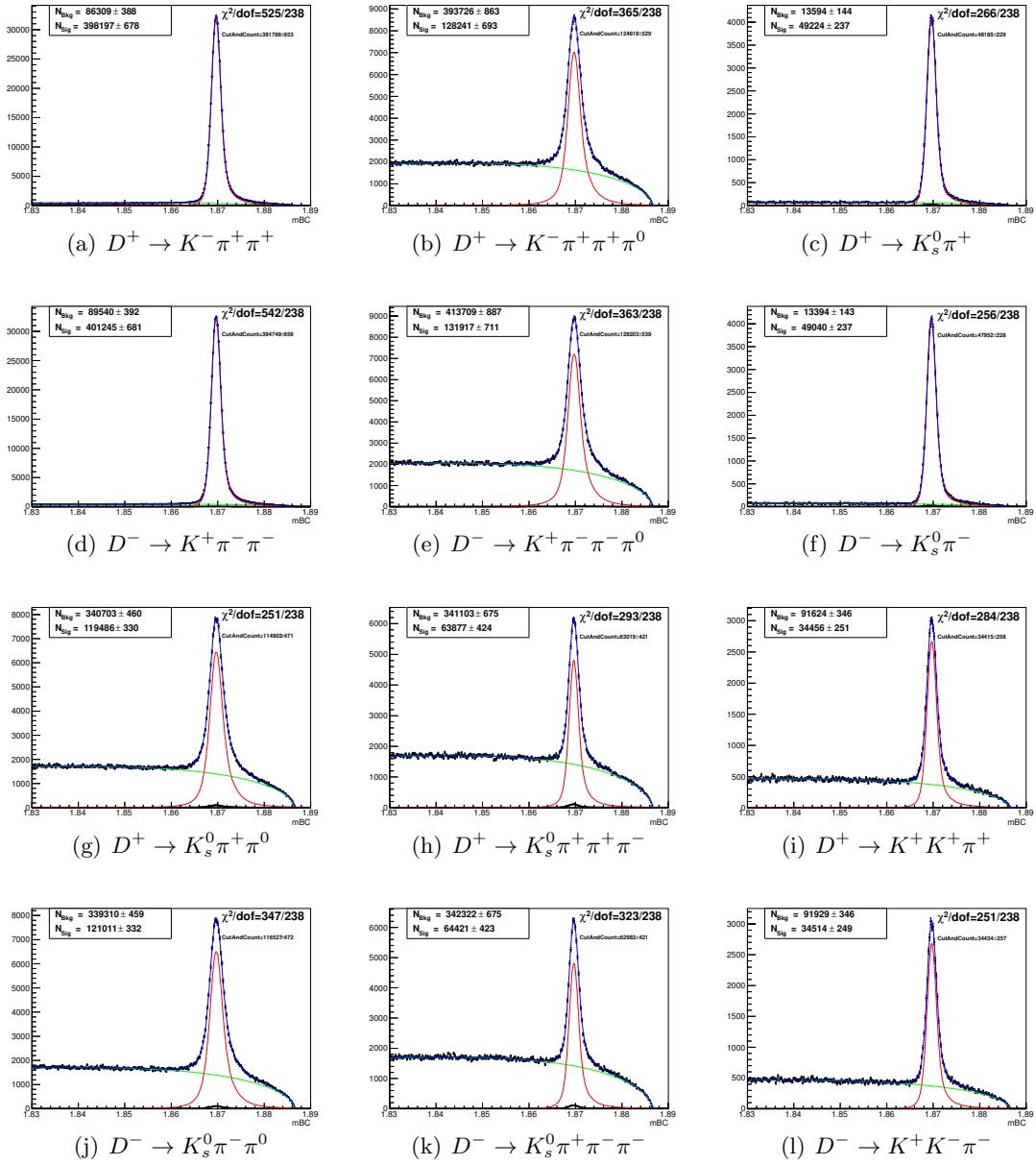

(a) $D^+ \to K^-\pi^+\pi^+$ (b) $D^+ \to K^-\pi^+\pi^+\pi^0$ (c) $D^+ \to K^0_s\pi^+$

(d) $D^- \to K^+\pi^-\pi^-$ (e) $D^- \to K^+\pi^-\pi^-\pi^0$ (f) $D^- \to K^0_s\pi^-$

(g) $D^+ \to K^0_s\pi^+\pi^0$ (h) $D^+ \to K^0_s\pi^+\pi^+\pi^-$ (i) $D^+ \to K^+K^+\pi^+$

(j) $D^- \to K^0_s\pi^-\pi^0$ (k) $D^- \to K^0_s\pi^+\pi^-\pi^-$ (l) $D^- \to K^+K^-\pi^-$

Figure 18: m_{BC} fits, from data, for charged D modes, as detailed in Section 6.4.

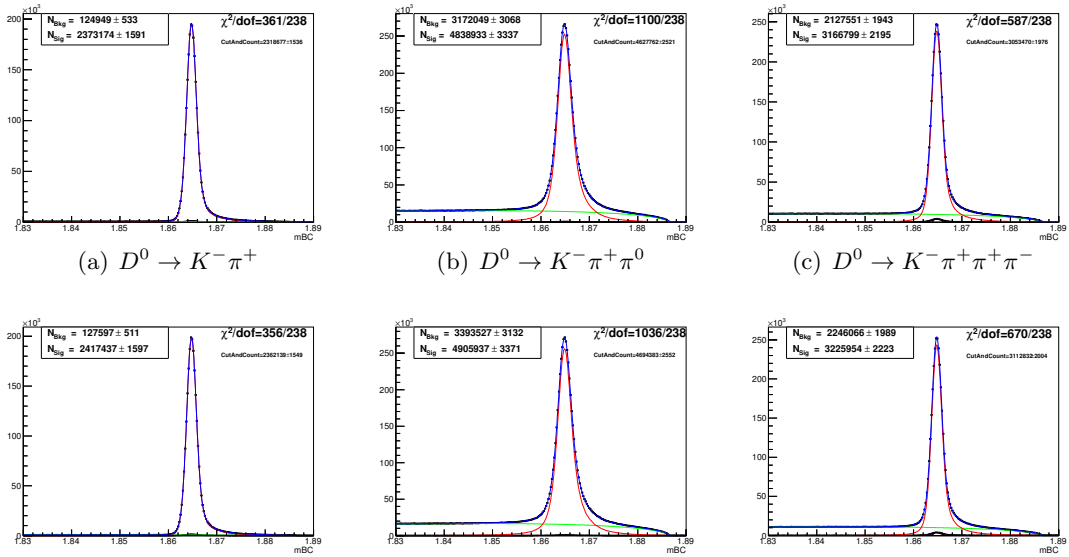

(a) $D^0 \to K^-\pi^+$ (b) $D^0 \to K^-\pi^+\pi^0$ (c) $D^0 \to K^-\pi^+\pi^+\pi^-$

(d) $\bar{D}^0 \to K^+\pi^-$ (e) $\bar{D}^0 \to K^+\pi^-\pi^0$ (f) $\bar{D}^0 \to K^+\pi^+\pi^-\pi^-$

Figure 19: m_{BC} fits used to determine single-tag efficiencies for neutral D modes, as detailed in Section 6.4, from a $\sim$ 10x data-sized sample of $D\bar{D}$ and background Monte Carlo sample, as described in Section 5.

Tag Mode	**Yield**	**Efficiency (%)**	Tag Mode	**Yield**	**Efficiency (%)**
$D^0 \to K^-\pi^+$	260915 ± 520	63.125 ± 0.007	$\bar{D}^0 \to K^+\pi^-$	262356 ± 522	64.272 ± 0.006
$D^0 \to K^-\pi^+\pi^0$	537923 ± 845	35.253 ± 0.007	$\bar{D}^0 \to K^+\pi^-\pi^0$	544252 ± 852	35.761 ± 0.007
$D^0 \to K^-\pi^+\pi^+\pi^-$	346583 ± 679	38.321 ± 0.007	$\bar{D}^0 \to K^+\pi^+\pi^-\pi^-$	351573 ± 687	39.082 ± 0.007
$D^+ \to K^-\pi^+\pi^+$	391786 ± 653	50.346 ± 0.005	$D^- \to K^+\pi^-\pi^-$	394749 ± 656	51.316 ± 0.005
$D^+ \to K^-\pi^+\pi^+\pi^0$	124619 ± 529	26.138 ± 0.014	$D^- \to K^+\pi^-\pi^-\pi^0$	128203 ± 539	26.586 ± 0.015
$D^+ \to K^0_S\pi^+$	48185 ± 229	36.726 ± 0.008	$D^- \to K^0_S\pi^-$	47952 ± 228	36.891 ± 0.008
$D^+ \to K^0_S\pi^+\pi^0$	114919 ± 471	20.687 ± 0.011	$D^- \to K^0_S\pi^-\pi^0$	116540 ± 472	20.69 ± 0.011
$D^+ \to K^0_S\pi^+\pi^+\pi^-$	63018 ± 421	21.966 ± 0.019	$D^- \to K^0_S\pi^+\pi^-\pi^-$	62982 ± 421	21.988 ± 0.019
$D^+ \to K^+K^-\pi^+$	34416 ± 258	41.525 ± 0.042	$D^- \to K^+K^-\pi^-$	34434 ± 257	41.892 ± 0.042

Table 6: Single-tag yields from data and efficiencies from Monte Carlo, by mode, as described in Section 6.4.

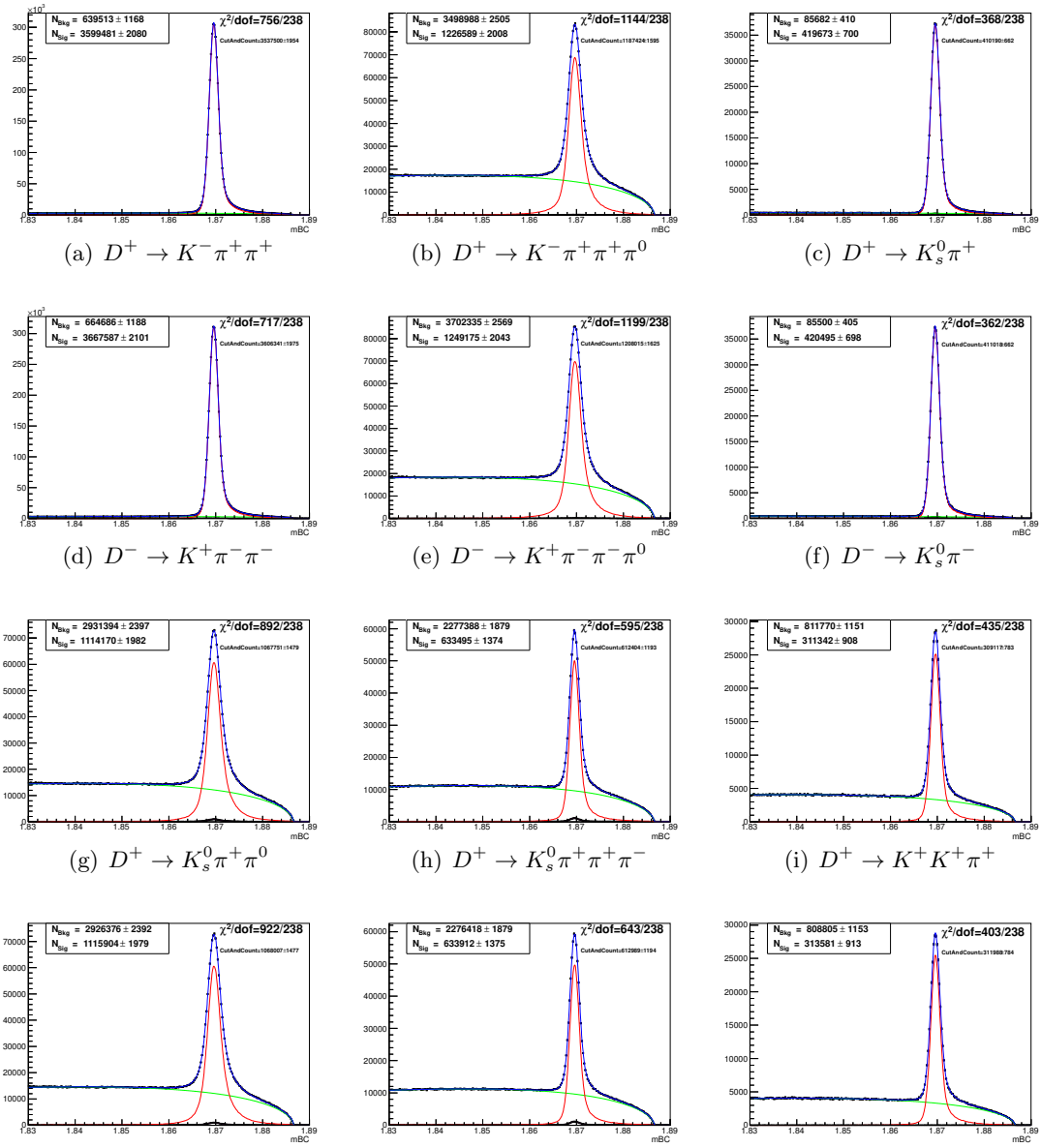

(a) $D^+ \to K^-\pi^+\pi^+$ (b) $D^+ \to K^-\pi^+\pi^+\pi^0$ (c) $D^+ \to K^0_s\pi^+$

(d) $D^- \to K^+\pi^-\pi^-$ (e) $D^- \to K^+\pi^-\pi^-\pi^0$ (f) $D^- \to K^0_s\pi^-$

(g) $D^+ \to K^0_s\pi^+\pi^0$ (h) $D^+ \to K^0_s\pi^+\pi^+\pi^-$ (i) $D^+ \to K^+K^+\pi^+$

(j) $D^- \to K^0_s\pi^-\pi^0$ (k) $D^- \to K^0_s\pi^+\pi^-\pi^-$ (l) $D^- \to K^+K^-\pi^-$

Figure 20: m_{BC} fits used to determine single-tag efficiencies for charged D modes, as detailed in Section 6.4, from a $\sim$ 10x data-sized sample of $D\bar{D}$ and background Monte Carlo sample, as described in Section 5.

6.5 Double-tag Yield and Efficiency Extraction

The double-tag yields are determined by performing a two-dimensional cut-and-count on the fitted m_{BC} distribution of the D and $\bar{D}$, analogous to the single-tag yield method but with more complicated background shapes due to the correlations between the tags. The signal-shape is derived from an approximately $10\times$ data-sized Monte Carlo sample, as described in Section 5, which has been truth-tagged and includes peaking backgrounds, which are discussed in more detail in Section 6.6. Unlike in the single-tag fits, the MC-derived signal shape used in double-tags is not convoluted with a smearing shape. The double-tag signal shape is not convoluted because it is unclear whether or not the convolution should be isotropic in the two-dimensional m_{BC} plane or not, due to the correlations between the two D-tags. We evaluated an isotropic convolution of the signal shape with a double-Gaussian and obtained negligibly different double-tag yields from the unconvolved fit, and so we are confident in our choice of an unconvolved double-tag signal shape.

The background shapes correspond to the four possible ways to mis-reconstruct an event. A direct product of a Monte Carlo derived signal-shape and an analytic ARGUS function background, with shape parameters fixed to those of the corresponding single-tag fit, is used to represent a correctly reconstructed D and incorrectly reconstructed $\bar{D}$. Similarly, there is another background-shape corresponding to the charm-conjugate situation. For events that are completely reconstructed continuum events or completely reconstructed but mispartitioned $D\bar{D}$ events (particles assigned incorrectly to the D and $\bar{D}$), a direct product of a double-Gaussian function and an ARGUS function rotated 45° is used as a representation. The end-point and power parameter of the rotated ARGUS are fixed, while the slope parameter, c, is allowed to float. It should be noted that the c parameter and the double-Gaussian parameters floated in the double-tag fits are associated with only the diagonal background, and do not correspond in any way to the similar parameters in the single-tag fits. Finally, background events that neiter involve a correctly reconstructed D meson, nor are completely reconstructed, are modelled with a direct product of two ARGUS functions, whose parameters are taken from the corresponding single-tag fits. The regions in which the various fit shapes dominate are illustrated in Figure 21. An example fit to data is shown with details in Figure 22, while all double-tag fits can be found in Appendix A. The fits in Appendix A have the same parameters that are fixed and floated as the fit in Figure 22, but the shape parameters have been suppressed in the outputs for easier viewing of the fits. The double-tag yields and efficiencies are summarized in Tables 7-8.

After the two-dimensional fit is performed, the m_{BC} histogram is integrated within the

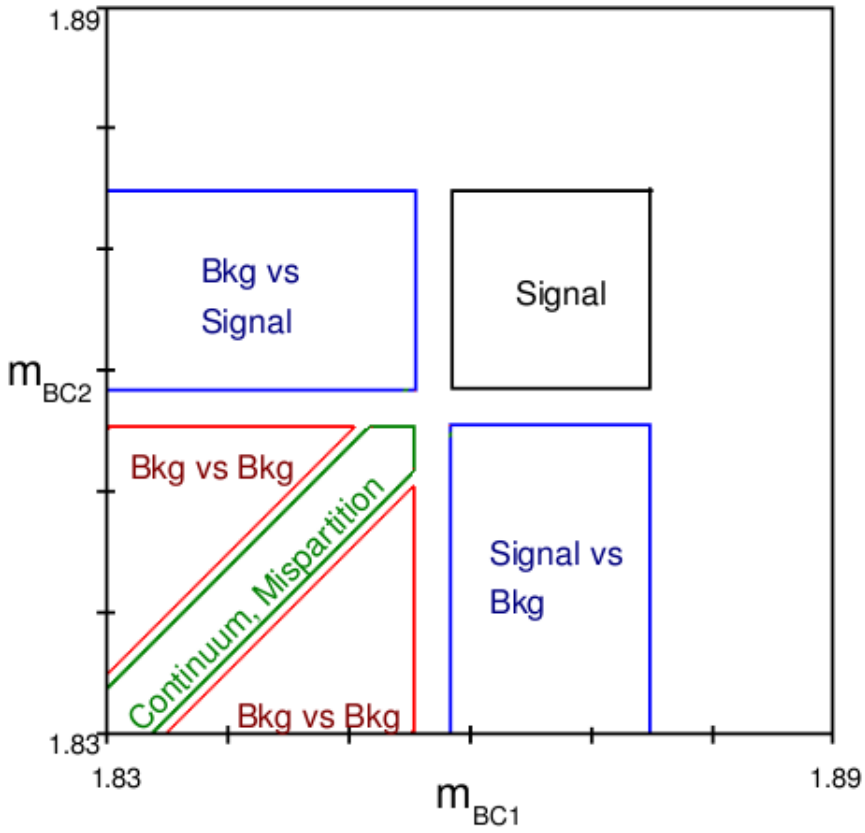

Figure 21: The two-dimensional m_{BC} plane divided into regions dominated by signal and various backgrounds. These regions represent the shapes used in the double-tag fitting method described in Section 6.5 and are used in the sideband-subtraction method described in Section 6.9.2.

same signal region as the single-tag fits, and the integrals of the four background shapes are subtracted from this total. As is the case with the single tags, the yield is then adjusted to remove peaking backgrounds.

Double-tag efficiencies are found using Monte Carlo truth information to determine the total number of each double-tag decay mode for the denominator, and using the same cut and count method as data on an independent, approximately 10× data-size Monte Carlo sample including generic $D\bar{D}$ decays and backgrounds, as listed in Section 5, to determine the numerator.

Tag Mode	**Yield**	**Efficiency (%)**
$D^0 \to K^-\pi^+$ vs. $\bar{D}^0 \to K^+\pi^-$	6545 ± 81	42.58 ± 0.13
$D^0 \to K^-\pi^+$ vs. $\bar{D}^0 \to K^+\pi^-\pi^0$	14701 ± 122	24.9 ± 0.06
$D^0 \to K^-\pi^+$ vs. $\bar{D}^0 \to K^+\pi^+\pi^-\pi^-$	9096 ± 96	25.54 ± 0.08
$D^0 \to K^-\pi^+\pi^0$ vs. $\bar{D}^0 \to K^+\pi^-$	14526 ± 122	24.94 ± 0.06
$D^0 \to K^-\pi^+\pi^0$ vs. $\bar{D}^0 \to K^+\pi^-\pi^0$	30311 ± 176	13.94 ± 0.03
$D^0 \to K^-\pi^+\pi^0$ vs. $\bar{D}^0 \to K^+\pi^+\pi^-\pi^-$	18651 ± 139	14.35 ± 0.03
$D^0 \to K^-\pi^+\pi^+\pi^-$ vs. $\bar{D}^0 \to K^+\pi^-$	8988 ± 96	25.77 ± 0.08
$D^0 \to K^-\pi^+\pi^+\pi^-$ vs. $\bar{D}^0 \to K^+\pi^-\pi^0$	18635 ± 139	14.32 ± 0.03
$D^0 \to K^-\pi^+\pi^+\pi^-$ vs. $\bar{D}^0 \to K^+\pi^+\pi^-\pi^-$	11572 ± 110	14.86 ± 0.04

Table 7: $D^0\bar{D}^0$ mode double-tag yields from data and efficiencies from Monte Carlo, as described in Section 6.5.

6.6 Peaking Background

We explicitly correct the data yields and fitted efficiencies for the presence of background decays which peak in the m_{BC} signal region. Such backgrounds come from other D decays which have similar kinematics and particle compositions as the faked mode. We rely on the Monte Carlo, which has been generated with PDG world-average branching fractions, to produce the correct fraction of peaking background events, as well as to calculate the reconstruction efficiency of these peaking background events. Many peaking backgrounds originate from a D meson with the same charm and charge as the reconstructed decay. These sorts of backgrounds appear in both single and double tags, and thus have little sensitivity to Monte Carlo because of cancellation in the ratio of single to double tags. Peaking backgrounds which come from a D of opposite charm or charge to the D that was reconstructed will not appear in the double tags and are more sensitive to correct Monte

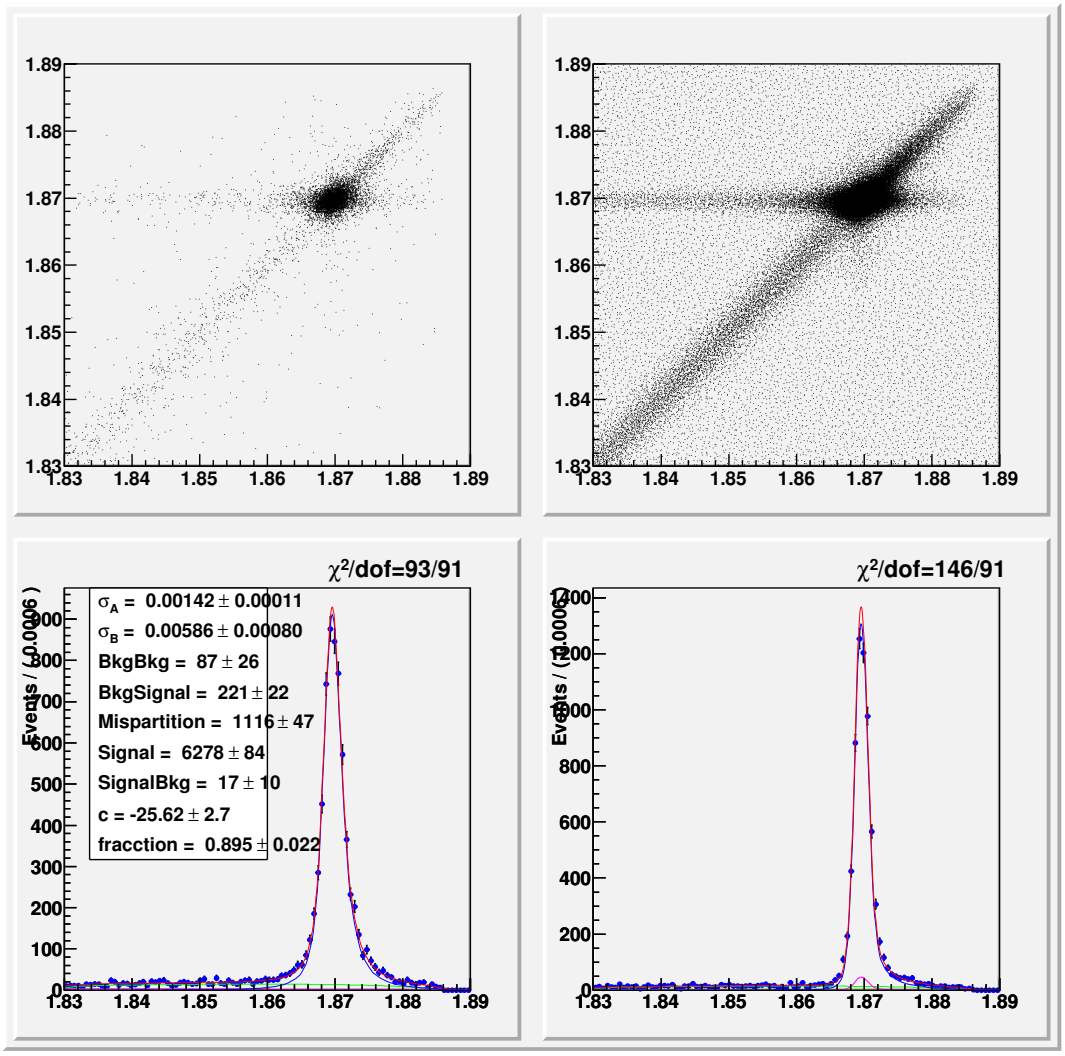

Figure 22: Example two-dimensional m_{BC} double-tag fit, from data, as detailed in Section 6.5, for tag-mode $K^-\pi^+\pi^+\pi^0 vs. K^+\pi^-\pi^-$. The top left figure is a scatter plot of the data, the top right is a scatter plot of the fit to the data, and the bottom two plots are overlays of data and the fit projected onto the positive and negative charm m_{BC} axes. The remaining double-tag fits are shown in Appendix A.

Tag Mode	**Yield**	**Efficiency (%)**
$D^+ \to K^-\pi^+\pi^+$ vs. $D^- \to K^+\pi^-\pi^-$	18800 ± 138	26.02 ± 0.05
$D^+ \to K^-\pi^+\pi^+$ vs. $D^- \to K^+\pi^-\pi^-\pi^0$	5981 ± 80	13.62 ± 0.05
$D^+ \to K^-\pi^+\pi^+$ vs. $D^- \to K^0_S\pi^-$	2368 ± 49	18.45 ± 0.12
$D^+ \to K^-\pi^+\pi^+$ vs. $D^- \to K^0_S\pi^-\pi^0$	5592 ± 75	10.51 ± 0.04
$D^+ \to K^-\pi^+\pi^+$ vs. $D^- \to K^0_S\pi^+\pi^-\pi^-$	2826 ± 53	10.82 ± 0.06
$D^+ \to K^-\pi^+\pi^+$ vs. $D^- \to K^+K^-\pi^-$	1597 ± 40	20.87 ± 0.15
$D^+ \to K^-\pi^+\pi^+\pi^0$ vs. $D^- \to K^+\pi^-\pi^-$	6067 ± 80	13.48 ± 0.05
$D^+ \to K^-\pi^+\pi^+\pi^0$ vs. $D^- \to K^+\pi^-\pi^-\pi^0$	1895 ± 53	6.79 ± 0.06
$D^+ \to K^-\pi^+\pi^+\pi^0$ vs. $D^- \to K^0_S\pi^-$	693 ± 26	9.82 ± 0.11
$D^+ \to K^-\pi^+\pi^+\pi^0$ vs. $D^- \to K^0_S\pi^-\pi^0$	1726 ± 44	5.22 ± 0.04
$D^+ \to K^-\pi^+\pi^+\pi^0$ vs. $D^- \to K^0_S\pi^+\pi^-\pi^-$	857 ± 33	5.41 ± 0.06
$D^+ \to K^-\pi^+\pi^+\pi^0$ vs. $D^- \to K^+K^-\pi^-$	549 ± 24	10.78 ± 0.15
$D^+ \to K^0_S\pi^+$ vs. $D^- \to K^+\pi^-\pi^-$	2352 ± 48	18.96 ± 0.12
$D^+ \to K^0_S\pi^+$ vs. $D^- \to K^+\pi^-\pi^-\pi^0$	722 ± 27	9.8 ± 0.12
$D^+ \to K^0_S\pi^+$ vs. $D^- \to K^0_S\pi^-$	269 ± 16	13.95 ± 0.27
$D^+ \to K^0_S\pi^+$ vs. $D^- \to K^0_S\pi^-\pi^0$	678 ± 26	7.67 ± 0.1
$D^+ \to K^0_S\pi^+$ vs. $D^- \to K^0_S\pi^+\pi^-\pi^-$	383 ± 20	7.9 ± 0.13
$D^+ \to K^0_S\pi^+$ vs. $D^- \to K^+K^-\pi^-$	191 ± 14	15.2 ± 0.34
$D^+ \to K^0_S\pi^+\pi^0$ vs. $D^- \to K^+\pi^-\pi^-$	5627 ± 75	10.64 ± 0.04
$D^+ \to K^0_S\pi^+\pi^0$ vs. $D^- \to K^+\pi^-\pi^-\pi^0$	1708 ± 43	5.28 ± 0.04
$D^+ \to K^0_S\pi^+\pi^0$ vs. $D^- \to K^0_S\pi^-$	624 ± 25	7.67 ± 0.1
$D^+ \to K^0_S\pi^+\pi^0$ vs. $D^- \to K^0_S\pi^-\pi^0$	1557 ± 40	4.08 ± 0.03
$D^+ \to K^0_S\pi^+\pi^0$ vs. $D^- \to K^0_S\pi^+\pi^-\pi^-$	747 ± 28	4.26 ± 0.05
$D^+ \to K^0_S\pi^+\pi^0$ vs. $D^- \to K^+K^-\pi^-$	503 ± 23	8.51 ± 0.13
$D^+ \to K^0_S\pi^+\pi^+\pi^-$ vs. $D^- \to K^+\pi^-\pi^-$	2857 ± 53	11.01 ± 0.06
$D^+ \to K^0_S\pi^+\pi^+\pi^-$ vs. $D^- \to K^+\pi^-\pi^-\pi^0$	924 ± 34	5.44 ± 0.06
$D^+ \to K^0_S\pi^+\pi^+\pi^-$ vs. $D^- \to K^0_S\pi^-$	313 ± 18	7.72 ± 0.13
$D^+ \to K^0_S\pi^+\pi^+\pi^-$ vs. $D^- \to K^0_S\pi^-\pi^0$	778 ± 29	4.17 ± 0.05
$D^+ \to K^0_S\pi^+\pi^+\pi^-$ vs. $D^- \to K^0_S\pi^+\pi^-\pi^-$	468 ± 24	4.28 ± 0.06
$D^+ \to K^0_S\pi^+\pi^+\pi^-$ vs. $D^- \to K^+K^-\pi^-$	246 ± 18	8.96 ± 0.19
$D^+ \to K^+K^-\pi^+$ vs. $D^- \to K^+\pi^-\pi^-$	1576 ± 40	21.31 ± 0.16
$D^+ \to K^+K^-\pi^+$ vs. $D^- \to K^+\pi^-\pi^-\pi^0$	509 ± 23	10.41 ± 0.15
$D^+ \to K^+K^-\pi^+$ vs. $D^- \to K^0_S\pi^-$	185 ± 14	14.48 ± 0.33
$D^+ \to K^+K^-\pi^+$ vs. $D^- \to K^0_S\pi^-\pi^0$	468 ± 22	8.23 ± 0.13
$D^+ \to K^+K^-\pi^+$ vs. $D^- \to K^0_S\pi^+\pi^-\pi^-$	232 ± 18	8.62 ± 0.19
$D^+ \to K^+K^-\pi^+$ vs. $D^- \to K^+K^-\pi^-$	156 ± 16	16.46 ± 0.53

Table 8: D^+D^- mode double-tag yields from data and efficiencies from Monte Carlo, as described in Section 6.5.

Carlo simulation. However, such peaking backgrounds are very small or well measured and thus will contribute negligibly to the systematic error.

We account for any peaking background which contributes more than 0.01% to the total fitted yield of the faked mode. The mode with the largest contribution of peaking background to the total fitted yield is $D^+ \to K_s\pi^+\pi^+\pi^-$, with about 2.5% of the total fitted yield coming from peaking backgrounds. $D^0 \to K^-\pi^+\pi^+\pi^-$ and $D^+ \to K_s\pi^+\pi^0$ both have $\sim 2\%$ of their total fitted yields from peaking backgrounds. All other modes have less than 1% of their fitted yields from peaking backgrounds. There are several categories of peaking background; these are listed in approximate order of contribution to the total fitted yield for the mode they are faking in the list below.

1. A charged pion pair that is not from a K_s, but still falls within the K_s invariant mass cut causes the dominant peaking background for single- and double-tag modes that reconstruct a K_s. These peaking backgrounds have the same final state as the decay modes they are reconstructing, except that the charged pion pair used to reconstruct the K_s is from combinatorial background. These peaking backgrounds account for up to $\sim 2\%$ of the total fitted yields of the tag modes they fake.

2. Doubly Cabibbo-suppressed decays are peaking backgrounds to the single-tag D^0 modes of opposite charm, but same particle composition. Such events have been correctly reconstructed, but have been assigned the wrong charm. These peaking backgrounds account for between $0.2 - 0.4\%$ of the total fitted yields of the tag modes they fake.

3. Incorrect particle identification occurs when the PID cuts, which are described in Section 6.2.1, misidentify a reconstructed particle(s), but the tag is otherwise correctly reconstructed. This can happen in D^0 modes where simultaneously misidentifying a charged kaon and pion effectively changes the charm of the reconstructed decay. For both D^0 and D^+ modes, misidentifying a lepton as a pion and missing a low-momentum neutrino also causes peaking background. Peaking backgrounds from particle misidentification account for up to $\sim 0.2\%$ of the fitted yields.

6.7 $\sigma_{D\bar{D}}$ Results

Once the many individual measurements of $N_{D\bar{D}_{ij}}$, the number of $D\bar{D}$ events as measured by positive charm tag-mode i and negative charm tag-mode j, have been made, these measurements must be combined. We combine them together using an error-weighted

mean. However, particular care must be taken with the handling of errors, as there are statistical correlations within and between the mode-dependent measurements of $N_{D\bar{D}}$.

To account for the shared population in the single and double tags, the statistical error on $N_{D\bar{D}_{ij}}$ includes an additional negative-definite term in addition to the fractional uncertainty from the yields.

$$\sigma_{N_{D\bar{D}_{ij}}} = N_{D\bar{D}_{ij}} \sqrt{(\frac{\sigma_{X_i}}{X_i})^2 + (\frac{\sigma_{Y_j}}{Y_j})^2 + (\frac{\sigma_{Z_{ij}}}{Z_{ij}})^2 + 2\sigma^2_{Z_{ij}} \frac{Z_{ij} - X_i - Y_j}{Z_{ij} X_i Y_j}} \tag{18}$$

The statistical error on the error-weighted mean must account for the correlations between mode combinations that share a common single-tag mode of the same charm. The shared populations between single- and double-tag modes across the separate $N_{D\bar{D}_{ij}}$ measurements must also be taken into account. To make these long equations more readable, we define a number of intermediate quantites: a ratio of Monte Carlo efficiencies

$$R_{ij} \equiv \frac{\epsilon_{ij}}{\epsilon_i \epsilon_j}, \tag{19}$$

the normalization due to error weighting

$$S \equiv \sum_{k,l} \sigma^{-2}_{N_{D\bar{D}_{kl}}}, \tag{20}$$

two terms for modified single-tag yield errors

$$\begin{aligned} \sigma^2_{\mathcal{X}_i} &\equiv \sigma^2_{X_i} - \sum_l \sigma^2_{Z_{il}} \\ \sigma^2_{\mathcal{Y}_j} &\equiv \sigma^2_{Y_j} - \sum_k \sigma^2_{Z_{kj}}, \end{aligned} \tag{21}$$

and finally two terms related to $N_{D\bar{D}_{ij}}$,

$$\begin{aligned} A_i &\equiv \sum_l \frac{R_{il} Y_l}{Z_{il} \sigma^2_{N_{D\bar{D}_{il}}}} \\ B_j &\equiv \sum_k \frac{R_{kj} X_k}{Z_{kj} \sigma^2_{N_{D\bar{D}_{kj}}}}. \end{aligned} \tag{22}$$

The statistical error on the error-weighted mean is then

$$\sigma_{<N_{D\bar{D}}>} = \frac{1}{S}\sqrt{\sum_{i,j} R_{ij}\left(\frac{A_i Y_j \sigma^2_{\mathcal{X}_i}}{Z_{ij}\sigma^2_{N_{D\bar{D}_{ij}}}} + \frac{B_j X_i \sigma^2_{\mathcal{Y}_j}}{Z_{ij}\sigma^2_{N_{D\bar{D}_{ij}}}} + \left(A_i + B_j - \frac{R_{ij} X_i Y_j}{Z^2_{ij}\sigma^2_{N_{D\bar{D}_{ij}}}}\right)^2 \sigma^2_{Z_{ij}}\right)}. \quad (23)$$

To verify these error calculations, toy Monte Carlo simulations were performed. We produced twenty thousand toy Monte Carlo trials for both charged and neutral D events. For each trial, we decayed approximately 1 fb^{-1} of $D\bar{D}$ pairs according to PDG branching ratios into the tag-modes used in this analysis, or to a generic non-tag decay. We simulated reconstruction by using reconstruction efficiencies taken from full Monte Carlo, including the effects of the other-side environment on the tag-side reconstruction. After obtaining the single- and double-tag yields within a trial, we calculate the weighted mean, $< N_{D\bar{D}} >$. We then plot $(< N_{D\bar{D}measured} > - N_{D\bar{D}simulated})/\sigma_{<N_{D\bar{D}}>}$ for each of the trials. If the error calculation is correct, then this distribution will have a mean of zero and a width of one when fitted with a Gaussian distribution.

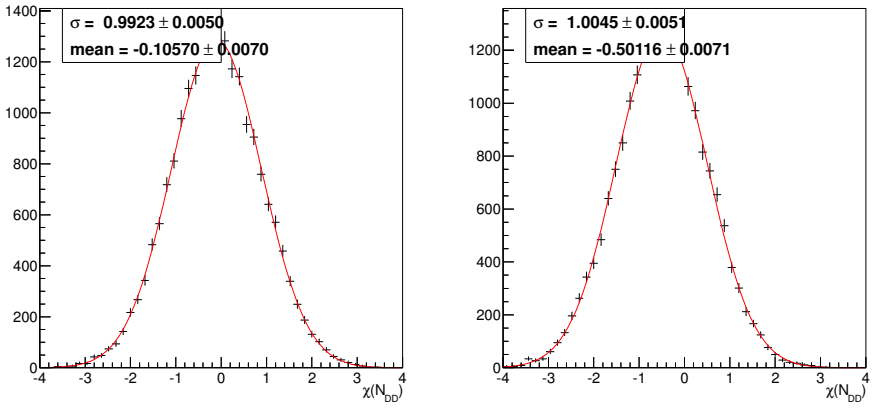

(a) $D^0\bar{D}^0$ (b) D^+D^-

Figure 23: Toy Monte Carlo plot of $(< N_{D\bar{D}measured} > - N_{D\bar{D}simulated})/\sigma_{<N_{D\bar{D}}>}$ for twenty thousand trials, with error calculated from Equation 23.

As seen in Figure 23, the magnitude of the error is correct, but the calculation of $< N_{D\bar{D}} >$ is systematically biased low. The calculation is biased because the error calculation of $\sigma_{N_{D\bar{D}_{ij}}}$, which weights each $N_{D\bar{D}_{ij}}$, is biased to give a lower reported error when $N_{D\bar{D}_{ij}}$ is smaller, as can be seen from Equation 18. If $N_{D\bar{D}_{ij}}$ is replaced by $< N_{D\bar{D}} >$ in this equation,

$$\sigma_{N_{D\bar{D}_{ij}}} =< N_{D\bar{D}} > \sqrt{(\frac{\sigma_{X_i}}{X_i})^2 + (\frac{\sigma_{Y_j}}{Y_j})^2 + (\frac{\sigma_{Z_{ij}}}{Z_{ij}})^2 + 2\sigma^2_{Z_{ij}} \frac{Z_{ij} - X_i - Y_j}{Z_{ij} X_i Y_j}}, \quad (24)$$

then this error is no longer biased. This can be accomplished by iteratively calculating $< N_{D\bar{D}} >$. The first iteration to calculate $< N_{D\bar{D}} >$ uses the biased Equation 18 to weight the measurements, because $< N_{D\bar{D}} >$ is not yet available. On the next iteration, $< N_{D\bar{D}} >$ is used in Equation 24 to re-calculate $< N_{D\bar{D}} >$. A single iteration is sufficient to remove all significant bias and obtain an accurate mean as shown in Figure 24. The statistical uncertainties on the Monte Carlo derived efficiencies are also included in the calculation of the weighted mean and its error, but these errors are much smaller than, and conceptually similar to, the associated errors from data and are consequently not shown above.

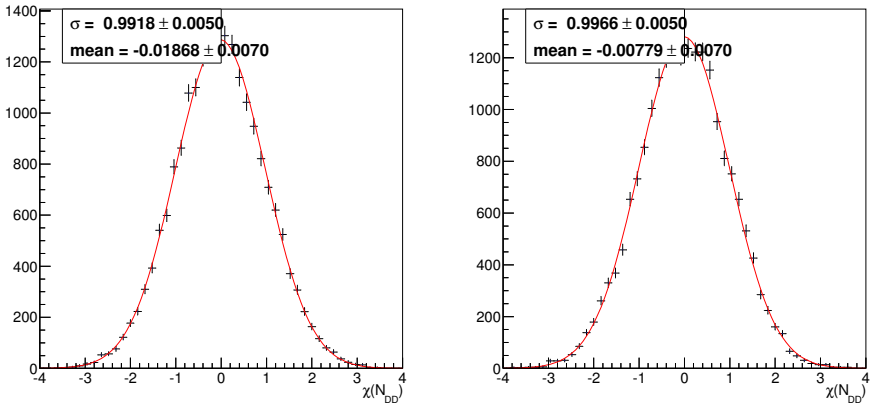

(a) $D^0\bar{D}^0$ (b) D^+D^-

Figure 24: Toy Monte Carlo plot of $(< N_{D\bar{D}measured} > -N_{D\bar{D}simulated})/\sigma_{<N_{D\bar{D}}>}$ for twenty thousand trials, with error calculated from Equation 23 and iterated using Equation 24.

For the 2.9 fb^{-1} data sample taken at 3.773 GeV, $N_{D^0\bar{D}^0} = (10,621 \pm 29(stat)) \times 10^3$ and $N_{D^+D^-} = (8,296 \pm 31(stat)) \times 10^3$. Using the integrated luminosity provided in Ref. [59], we measure $\sigma_{D^0\bar{D}^0} = (3.641 \pm 0.010\ (stat))$ nb and $\sigma_{D^+D^-} = (2.844 \pm 0.011\ (stat))$ nb. The individual measurements of $\sigma_{D\bar{D}}$ by mode used to calculate the weighted mean are shown in Figures 25-26. Also shown are the cross sections calculated from the mode-by-mode single-tag measurements, as explained in Section 6.3, Equation 13. The single-tag measurement is shown as a basis for comparison and a consistency check, but is not used in our calculations. The larger and unaccounted for systematic errors from the single-tag

method explain the slight inconsistencies with our standard double-tag method. This plot also highlights how much the systematic uncertainty of the tag-mode branching fractions mitigates any potential statistical gain when using the single-tag method compared to the double-tag method.

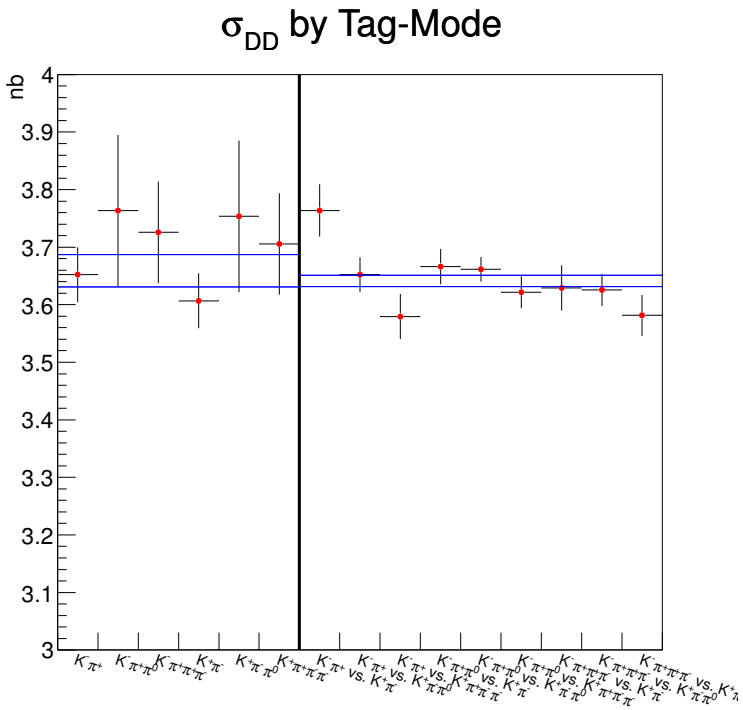

Figure 25: Plot of $\sigma_{D^0\bar{D}^0}$ comparing the single-tag method (to the left of the thick dividing line) and the standard double-tag method (to the right of the line) on a mode-by-mode basis. Only statistical and branching fraction (single-tag method only) errors are shown. The PDG branching fractions of $D^0 \to K^-K_s\pi^+, K_s \to \pi^+\pi^-$ has been added to the exclusive PDG branching fractions for the associated tag mode used in the single-tag calculation. The error-weighted means of these measurements are represented by a one σ band.

6.8 Consistency Checks

To demonstrate the stability and reliability of our $D\bar{D}$ cross section measurement, we perform a Monte Carlo "In vs. Out" test and also show consistency by dividing the data and performing our cross section measurement on these subdivisions. For the "In vs. Out" test,

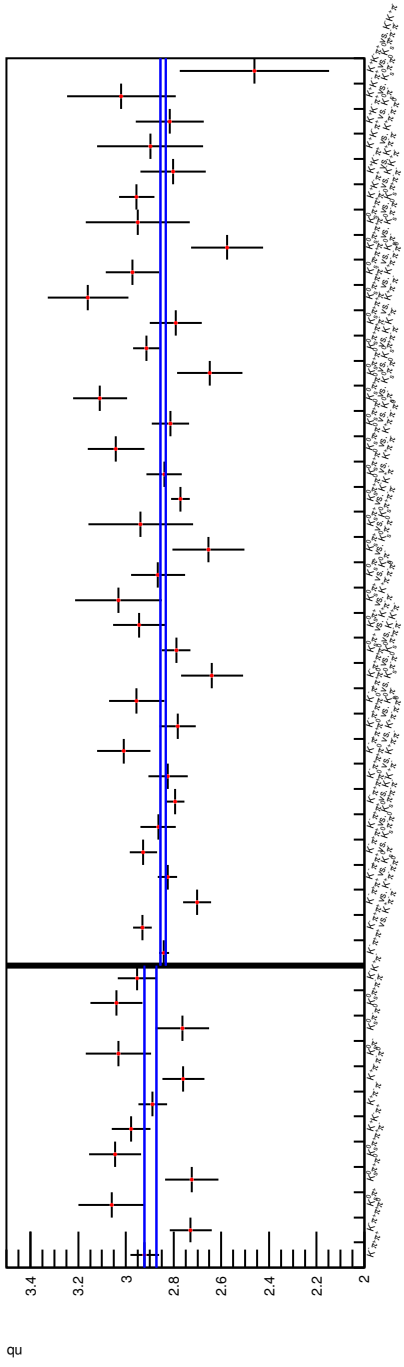

Figure 26: Plot of $\sigma_{D^+D^-}$ comparing the single-tag method (to the left of the thick dividing line) and the standard double-tag method (to the right of the line) on a mode-by-mode basis. Only statistical and branching fraction (single-tag method only) errors are shown. The PDG branching fractions of $D^+ \to K^*(892)^+K_s, K^*(892)^+ \to K_s\pi+, K_s \to \pi^+\pi^-$ has been added to the exclusive PDG branching fractions for the associated tag mode used in the single-tag calculation. The error-weighted means of these measurements are represented by a one σ band.

we randomly divided the 3.773 GeV Monte Carlo described in Section 5, including generic $D\bar{D}$ and the various background samples, into ten sets which were each approximately data-sized. We then determined single- and double-tag yields from this Monte Carlo in the same way in which we determine them for data and use these to calculate $N_{D\bar{D}}$ for each of the ten Monte Carlo sets. We compared the measured values of $N_{D\bar{D}}$ to the known values obtained from the Monte Carlo generator information and divided by the statistical error of the measurement to determine the deviation of the measurement from the true value. These deviations are summarized in Table 9. The χ^2/DoF is 10.685/10 for $N_{D^0\bar{D}^0}$, and for $N_{D^+D^-}$ it is 12.389/10. The results of the "In vs. Out" test show that we are able to reliably calculate $N_{D\bar{D}}$ and estimate its error.

	Deviation of measured $N_{D\bar{D}}$ from true value									
Set	1	2	3	4	5	6	7	8	9	10
$N_{D^0\bar{D}^0}$	1.14	-0.71	-0.91	0.83	1.16	0.65	0.10	1.01	-2.13	0.22
$N_{D^+D^-}$	-0.58	0.68	0.91	-2.65	0.96	-0.60	-1.10	-0.62	0.90	0.28

Table 9: Monte Carlo "In vs. Out" test results. The deviation is defined as the simulated number of $D\bar{D}$ events subtracted from the measured number of $D\bar{D}$ events and divided by the statistical error on the measured number of $D\bar{D}$ events.

For the data consistency check, we divided the data into six chunks of approximately 0.5 fb^{-1} apiece and independently measured $\sigma_{D^0\bar{D}^0}$ and $\sigma_{D^+D^-}$ in each of the chunks. We then calculated the error-weighted mean of these cross sections using the six measured values and calculated the deviation from the mean for each chunk of data. The results of these measurements are shown in Table 10. For the six measurements of $\sigma_{D^0\bar{D}^0}$ we measured a χ^2/DoF of 5.36/5, and 6.02/5 for $\sigma_{D^+D^-}$. Both of these values are quite reasonable and demonstrate good consistency.

We also compared the ratio of the cross sections in the six chunks in a similar manner. The results of this measurement are also summarized in Table 10. The χ^2/DoF of these measurements is 0.93/5. Although the χ^2/DoF is quite low, the probability for this is 0.9676, which is high, but not unreasonably so. Thus we demonstrate the reliability of our method in an integrated-luminosity-independent way as well.

		$\sigma_{\mathbf{D^0\bar{D}^0}}$(nb)			$\sigma_{\mathbf{D^+D^-}}$(nb)			$\sigma_{\mathbf{D^0\bar{D}^0}}/\sigma_{\mathbf{D^+D^-}}$		
Runs*	$\mathcal{L}$ **(pb^{-1})**	**Value**	**Error**	χ	**Value**	**Error**	χ	**Value**	**Error**	χ
11414-13025	464.16	3.659	0.025	-0.6042	2.836	0.027	-0.9467	1.290	0.015	0.4145
13026-20447*	462.76	3.661	0.025	-0.5403	2.836	0.028	-0.9558	1.291	0.015	0.4580
20448-21430	506.36	3.679	0.024	0.2058	2.857	0.026	-0.2093	1.288	0.014	0.2841
21431-22080	510.40	3.722	0.024	2.0030	2.915	0.026	2.0381	1.277	0.014	-0.5126
22081-22790	475.51	3.660	0.024	-0.5966	2.864	0.027	0.0759	1.278	0.015	-0.4137
22791-23454	486.66	3.662	0.024	-0.5413	2.859	0.031	-0.1021	1.281	0.016	-0.1957
Weighted Mean	-	3.675	-	-	2.862	-	-	1.284	-	-

*Only the runs described in Section 5 were used

Table 10: The full $\psi(3770)$ data set was divided into six roughly equal chunks and then $\sigma_{D^0\bar{D}^0}$ and $\sigma_{D^+D^-}$ were measured in each chunk. The individual measurements were then compared against the error-weighted mean to check consistency. $\frac{\sigma_{D^0\bar{D}^0}}{\sigma_{D^+D^-}}$ was also compared as a integrated-luminosity-independent cross-check.

6.9 $\sigma_{D\bar{D}}$ Systematics

6.9.1 Cancelling Systematics

Due to the double-tag technique employed in this analysis, many of the systematic errors of $\sigma_{D\bar{D}}$ will cancel because they are present in both the single and double tags. Tag-side resonant sub-structure and the ΔE cut are among the physics-based systematic effects that occur similarly in both single and double tags. Detector effects such as π^0 and K_s^0 reconstruction, particle identification, and tracking are also present in single and double tags and cancel accordingly. To verify that these effects do indeed cancel in the manner proposed, we imposed harsh cuts on a few representative variables in the Monte Carlo sample only and noted the change in the $\frac{\epsilon_i \epsilon_j}{\epsilon_{ij}}$ ratio.

As a stand in for detector effects, we used the R_0 variable, the distance of a track's closest approach to the interaction point in the transverse direction. By default, this is cut at 1 cm for charged tracks comprising the D-tag, and on a mode-by-mode and particle (charged kaons or pions) basis we imposed a stricter R_0 cut that reduced the single-tag reconstruction efficiency by 0.5% per charged track, a number typical of the tracking systematic error [61]. The changes in the $\frac{\epsilon_i \epsilon_j}{\epsilon_{ij}}$ ratio were negligible. The variable used as a stand-in for physics effects was ΔE. We reduced the ΔE window by 0.5σ on both the low and high-side, and again observed negligible changes in $\frac{\epsilon_i \epsilon_j}{\epsilon_{ij}}$. These two studies confirm that dependence on the ratio $\frac{\epsilon_i \epsilon_j}{\epsilon_{ij}}$ results in cancellation of many systematic errors.

6.9.2 Fitting Systematics

We examine potential systematic effects associated with fitting even though we fit both single and double tags to obtain yields and efficiencies. The differences between one- and two-dimensional fits and the relative cleanliness of the double-tag m_{BC} distributions compared to the single-tag distributions are enough to warrant treatment of the fitting systematic error. We take excursions of the efficiency-corrected yields under alternatative methods as our systematic uncertainty associated with fitting. We choose efficiency-corrected yields, and not yields and efficiencies separately, because of the similar treatment of data and MC which we expect to result in some cancellation of the excursions.

To test the uncertainty due to the background shape used in single-tag fitting, we use a Monte Carlo derived background shape instead of the analytic ARGUS function, and observe the change in efficiency-corrected yields after fitting. Similarly, we gauge the effect of the signal-shape by fitting with a single-Gaussian convolved signal-shape, as opposed to the standard double-Gaussian convolved shape. The differences between the efficiency-

corrected yields obtained with these two shapes and our standard fit shapes are taken to be the systematic error associated with single-tag fitting, as seen in Table 11.

Tag Mode	**Signal-Shape (%)**	**Background-Shape (%)**
$D^0 \to K^-\pi^+$	0.27	0.19
$D^0 \to K^-\pi^+\pi^0$	0.1	0.59
$D^0 \to K^-\pi^+\pi^+\pi^-$	0.47	0.5
$D^+ \to K^-\pi^+\pi^+$	0.2	0.31
$D^+ \to K^-\pi^+\pi^+\pi^0$	0	1.1
$D^+ \to K^0_s\pi^+$	0.17	0.13
$D^+ \to K^0_s\pi^+\pi^0$	0.29	1.82
$D^+ \to K^0_s\pi^+\pi^+\pi^-$	0.17	3.11
$D^+ \to K^+K^-\pi^+$	0.74	1.18

Table 11: The systematic error due to the single-tag fitting procedure, for both the signal and background shapes.

In order to test our double-tag fitting procedure, we obtain double-tag yields and efficiencies with an alternative sideband-subtraction method, originally used in [62]. We divide the two-dimensional m_{BC} plane into several sections representing the signal and various background components, shown in Figure 21.

The signal area is the same as that used when fitting, a horizontal and vertical band are used to represent one correctly reconstructed D and one incorrectly reconstructed D, a diagonal band represents the background from completely reconstructed continuum events or mispartitioned $D\bar{D}$ events, and two triangles are used to represent the remaining mostly flat background. These areas are further defined in Table 12. An estimate of the flat background is scaled with the relative size of the patches into each of the other background regions and subtracted off to obtain the estimate of each of the non-flat backgrounds in the locations in which they predominate. These backgrounds are then scaled with area and ARGUS background parameters obtained from single-tag fits into the signal area and subtracted to obtain the signal yield, as follows:

$$Yield = (S - D \cdot \frac{a_S}{a_D}) - s_A \cdot (A - D \cdot \frac{a_A}{a_D}) - s_B \cdot (B - D \cdot \frac{a_B}{a_D}) - s_C \cdot (C - D \cdot \frac{a_C}{a_D}).$$

The capital letters represent the raw counts in the various regions, the lower-case a_i,

where i indexes the region, are the areas of the corresponding regions, and the lowercase s_i are the ratios of the fitted single-tag ARGUS background in the signal region to the ARGUS background in the background region, for the appropriate tag mode. The difference in efficiency-corrected double-tag yields between this method and the standard double-tag fitting method is taken as the uncertainty on the double-tag fitting method, shown in Tables 13-14.

The cosmic and lepton veto serves to suppress cosmic ray and QED events in the $K\pi$ mode, our only two track mode. However, this veto may not entirely eliminate the cosmic and lepton background, as seen in Figure 14, which is not present in Monte Carlo, nor well described by the ARGUS background shape. The cosmic ray events are formed from only a single particle with the incorrect assumption that it is made of two particles of opposite charge that causes the net momentum of the two tracks to be close to zero. Similarly, QED events have a net momentum close to zero. The low net momentum causes the m_{BC} of such events to be approximately equal to the beam energy and consequently hard to fit if they are not successfully rejected by the cosmic and lepton veto. To assess the effect of the fitting uncertainty, the single-tag fits for $K\pi$ were done only up to an m_{BC} of 1.88 GeV, excluding the range where cosmic and QED events can distort the fits. The resulting difference from the standard fits was found to be 0.18% and taken to be the uncertainty due to this effect.

6.9.3 Other $D\bar{D}$ Systematics

The lineshape of the $\psi(3770)$ is also a cause of a potential difference between data and Monte Carlo occuring in both single and double tags. While it is thus subject to some cancellation, we treat this effect separately because it affects yields and efficiencies in opposite directions and also causes correlations in the double-tag fits that are not present in the single-tag fits. The effect of initial-state radiation (ISR) allows the lineshape to enter our measurement at the $\psi(3770)$ peak by determining the cross section of $\psi(3770)$ production at the energy to which the photons radiate. The Monte Carlo efficiencies are affected through the ΔE cuts that select against large initial state radiation, because the calculation of ΔE assumes that the energy available to the D is the full beam energy. The data yields are affected via the m_{BC} fit shape, whose asymmetric high-side tail's shape is influenced by production of $\psi(3770)$ via ISR. More initial-state radiation causes a larger high-side tail in both the single- and double-tag signal shapes. Additionally, because both D mesons lose energy when initial state radiation occurs, double-tag events that include ISR will have a correlated shift in m_{BC}. This correlated shift causes such events to follow along the diagonal to the high-

$D^0\bar{D}^0$ Region	m_{BC1} (GeV)	m_{BC2} (GeV)	Other (GeV)
Signal	$1.858 \leq m_{BC1} \leq 1.874$	$1.858 \leq m_{BC2} \leq 1.874$	
A (Bkg vs. Signal)	$1.83 \leq m_{BC1} \leq 1.855$	$1.858 \leq m_{BC2} \leq 1.874$	
B (Signal vs. Bkg)	$1.858 \leq m_{BC1} \leq 1.874$	$1.83 \leq m_{BC2} \leq 1.855$	
C (Mispartition)	$1.83 \leq m_{BC1} \leq 1.855$	$1.83 \leq m_{BC2} \leq 1.855$	$\lvert m_{BC1} m_{BC2} \rvert \leq 4.25$ MeV
D (Bkg vs. Bkg)	$1.83 \leq m_{BC1} \leq 1.855$	$1.83 \leq m_{BC2} \leq 1.855$	$\lvert m_{BC1} m_{BC2} \rvert \geq 5.75$ MeV

D^+D^- Region	m_{BC1}	m_{BC2}	Other
Signal	$1.8628 \leq m_{BC1} \leq 1.8788$	$1.8628 \leq m_{BC2} \leq 1.8788$	
A (Bkg vs. Signal)	$1.83 \leq m_{BC1} \leq 1.86$	$1.8628 \leq m_{BC2} \leq 1.8788$	
B (Signal vs. Bkg)	$1.8628 \leq m_{BC1} \leq 1.8788$	$1.83 \leq m_{BC2} \leq 1.86$	
C (Mispartition)	$1.83 \leq m_{BC1} \leq 1.86$	$1.83 \leq m_{BC2} \leq 1.86$	$\lvert m_{BC1} m_{BC2} \rvert \leq 4.25$ MeV
D (Bkg vs. Bkg)	$1.83 \leq m_{BC1} \leq 1.86$	$1.83 \leq m_{BC2} \leq 1.86$	$\lvert m_{BC1} m_{BC2} \rvert \geq 5.75$ MeV

Table 12: The cuts defining the various double-tag sideband-subtraction regions.

side of the signal region in the two-dimensional m_{BC} plane. A change in the $\psi(3770)$ lineshape used to generate Monte Carlo pulls the data yields and Monte Carlo efficiencies in opposite directions. This is because a higher cross section after significant initial-state radiation lowers Monte Carlo efficiency due to more events failing the ΔE cut, while raising the yields obtained from data by effectively broadening the signal fit-shape.

Using data taken with beam energy spanning the $\psi(3770)$ resonance, Nick Smith measured and fit the $\psi(3770)$ lineshape [63]. We use this preliminary measurement to re-weight the Monte Carlo and repeat the D-counting procedure with the re-weighted Monte Carlo being used to determine both the efficiencies, and the fit-shapes used to extract data yields. We take the variations on mode-dependent measurements of $N_{D\bar{D}}$ as the error associated with the $\psi(3770)$ lineshape for that double-tag mode.

Tag Mode	**Lineshape Systematic (%)**	**Double-Tag Fit Systematic (%)**
$D^0 \to K^-\pi^+$ vs. $\bar{D}^0 \to K^+\pi^-$	0.18	0.05
$D^0 \to K^-\pi^+$ vs. $\bar{D}^0 \to K^+\pi^-\pi^0$	0.1	0.53
$D^0 \to K^-\pi^+$ vs. $\bar{D}^0 \to K^+\pi^+\pi^-\pi^-$	0.46	0.27
$D^0 \to K^-\pi^+\pi^0$ vs. $\bar{D}^0 \to K^+\pi^-$	0.15	0.18
$D^0 \to K^-\pi^+\pi^0$ vs. $\bar{D}^0 \to K^+\pi^-\pi^0$	0.48	0.99
$D^0 \to K^-\pi^+\pi^0$ vs. $\bar{D}^0 \to K^+\pi^+\pi^-\pi^-$	0.53	0.58
$D^0 \to K^-\pi^+\pi^+\pi^-$ vs. $\bar{D}^0 \to K^+\pi^-$	0.09	0.85
$D^0 \to K^-\pi^+\pi^+\pi^-$ vs. $\bar{D}^0 \to K^+\pi^-\pi^0$	0.36	0.72
$D^0 \to K^-\pi^+\pi^+\pi^-$ vs. $\bar{D}^0 \to K^+\pi^+\pi^-\pi^-$	0.24	0.76

Table 13: The systematic error associated with the $\psi(3770)$ lineshape and the double-tag fitting procedure, by $D^0\bar{D}^0$ double-tag mode.

The Monte Carlo modelling of final-state radiation (FSR) may give rise to a systematic difference between data and Monte Carlo tag reconstruction efficiencies. Final-state radiation affects our measurement from the tag-side, and so any systematic effect will also have some cancellation. To assess the error due to FSR we create signal MC both with and without Monte Carlo modelling of FSR and observe the change in tag reconstruction efficiency. The largest difference was in the $D^0 \to K^-\pi^+$ mode, where the change in single-tag reconstruction efficiency was 4%, relative. The $D^0 \to K^-\pi^+, \bar{D}^0 \to K^+\pi^-$ double-tag reconstruction efficiency also changed when FSR modelling was turned off, but cancellations were not quite exact. The ratio of Monte Carlo efficiencies changed by 1.2%. The variation of turning on and off the FSR modelling is quite extreme, so we take 25% of this

Tag Mode	**Lineshape Systematic (%)**	**Double-Tag Fit Systematic (%)**
$D^+ \to K^-\pi^+\pi^+$ vs. $D^- \to K^+\pi^-\pi^-$	0.76	0.22
$D^+ \to K^-\pi^+\pi^+$ vs. $D^- \to K^+\pi^-\pi^-\pi^0$	0.92	0.73
$D^+ \to K^-\pi^+\pi^+$ vs. $D^- \to K^0_S\pi^-$	0.64	0.86
$D^+ \to K^-\pi^+\pi^+$ vs. $D^- \to K^0_S\pi^-\pi^0$	0.64	0.8
$D^+ \to K^-\pi^+\pi^+$ vs. $D^- \to K^0_S\pi^+\pi^-\pi^-$	0.58	0.02
$D^+ \to K^-\pi^+\pi^+$ vs. $D^- \to K^+K^-\pi^-$	0.41	0.37
$D^+ \to K^-\pi^+\pi^+\pi^0$ vs. $D^- \to K^+\pi^-\pi^-$	0.64	0.51
$D^+ \to K^-\pi^+\pi^+\pi^0$ vs. $D^- \to K^+\pi^-\pi^-\pi^0$	2.27	4.54
$D^+ \to K^-\pi^+\pi^+\pi^0$ vs. $D^- \to K^0_S\pi^-$	0.39	0.3
$D^+ \to K^-\pi^+\pi^+\pi^0$ vs. $D^- \to K^0_S\pi^-\pi^0$	1.21	1.13
$D^+ \to K^-\pi^+\pi^+\pi^0$ vs. $D^- \to K^0_S\pi^+\pi^-\pi^-$	0.97	1.75
$D^+ \to K^-\pi^+\pi^+\pi^0$ vs. $D^- \to K^+K^-\pi^-$	1.47	2
$D^+ \to K^0_S\pi^+$ vs. $D^- \to K^+\pi^-\pi^-$	0.93	0.54
$D^+ \to K^0_S\pi^+$ vs. $D^- \to K^+\pi^-\pi^-\pi^0$	0.18	0.06
$D^+ \to K^0_S\pi^+$ vs. $D^- \to K^0_S\pi^-$	1.31	0.3
$D^+ \to K^0_S\pi^+$ vs. $D^- \to K^0_S\pi^-\pi^0$	0.29	0.38
$D^+ \to K^0_S\pi^+$ vs. $D^- \to K^0_S\pi^+\pi^-\pi^-$	0.36	1.5
$D^+ \to K^0_S\pi^+$ vs. $D^- \to K^+K^-\pi^-$	0.06	2.38
$D^+ \to K^0_S\pi^+\pi^0$ vs. $D^- \to K^+\pi^-\pi^-$	0.45	1.07
$D^+ \to K^0_S\pi^+\pi^0$ vs. $D^- \to K^+\pi^-\pi^-\pi^0$	0.92	0.27
$D^+ \to K^0_S\pi^+\pi^0$ vs. $D^- \to K^0_S\pi^-$	0.58	0.51
$D^+ \to K^0_S\pi^+\pi^0$ vs. $D^- \to K^0_S\pi^-\pi^0$	0.05	0.33
$D^+ \to K^0_S\pi^+\pi^0$ vs. $D^- \to K^0_S\pi^+\pi^-\pi^-$	0.11	1.77
$D^+ \to K^0_S\pi^+\pi^0$ vs. $D^- \to K^+K^-\pi^-$	0.67	3.28
$D^+ \to K^0_S\pi^+\pi^+\pi^-$ vs. $D^- \to K^+\pi^-\pi^-$	0.5	0.81
$D^+ \to K^0_S\pi^+\pi^+\pi^-$ vs. $D^- \to K^+\pi^-\pi^-\pi^0$	1.34	1.33
$D^+ \to K^0_S\pi^+\pi^+\pi^-$ vs. $D^- \to K^0_S\pi^-$	0.71	5.21
$D^+ \to K^0_S\pi^+\pi^+\pi^-$ vs. $D^- \to K^0_S\pi^-\pi^0$	0.19	2.11
$D^+ \to K^0_S\pi^+\pi^+\pi^-$ vs. $D^- \to K^0_S\pi^+\pi^-\pi^-$	0.06	9.11
$D^+ \to K^0_S\pi^+\pi^+\pi^-$ vs. $D^- \to K^+K^-\pi^-$	0.98	3.57
$D^+ \to K^+K^-\pi^+$ vs. $D^- \to K^+\pi^-\pi^-$	0	0.27
$D^+ \to K^+K^-\pi^+$ vs. $D^- \to K^+\pi^-\pi^-\pi^0$	1.29	0.7
$D^+ \to K^+K^-\pi^+$ vs. $D^- \to K^0_S\pi^-$	0.68	9.59
$D^+ \to K^+K^-\pi^+$ vs. $D^- \to K^0_S\pi^-\pi^0$	0.45	1.16
$D^+ \to K^+K^-\pi^+$ vs. $D^- \to K^0_S\pi^+\pi^-\pi^-$	2.16	9.66
$D^+ \to K^+K^-\pi^+$ vs. $D^- \to K^+K^-\pi^-$	1.17	7.91

Table 14: The systematic error associated with the $\psi(3770)$ lineshape and the double-tag fitting procedure, by D^+D^- double-tag mode.

difference as our systematic error due to FSR modelling, 0.3% relative error on the Monte Carlo reconstruction efficiency ratio. We conservatively take the largest disagreement, from the $D^0 \to K^-\pi^+$ mode, as the systematic error for all modes.

The environment in which D-tagging is conducted affects the tagging efficiency because higher charged track or π^0 multiplicities serve to lower the tagging efficiency, and cause differences in efficiency of up to about 5%, absolute. In particular, differences between the other-side multiplicity between data and Monte Carlo can lead to systematic differences in the nominal efficiency obtained from Monte Carlo and the efficiency in true data. The method to calculate this effect is the same for tracks as it is for π^0s. The two measurements are done separately, but identically. In this study, when charged tracks/particles are mentioned, it follows similarly for π^0s, and so π^0s will not be mentioned explicitly.

The tag reconstruction efficiency can be written as

$$\epsilon_{Tot} = \sum_{i=0}^{N_{Gen}} \mathfrak{n}_i \cdot \epsilon_i, \tag{25}$$

where i is the number of charged particles generated on the other side, $\mathfrak{n}_i$ is the fraction of events generated with the appropriate tag-side decay and i other-side charged particles, and ϵ_i is the tagging efficiency for events with the same. The limit of the summation, N_{Gen} is the largest number of generated potential other-side charged particles and is 10. These quantities can all be measured directly in Monte Carlo using truth-tagging and decay-tree information.

To assess the differences between data and Monte Carlo due to other-side multiplicity, we would like to make a similar measurement in data. The tagging efficiency as a function of other-side multiplicity is assumed to be the same for data and Monte Carlo, while the fraction of events of each multiplicity is assumed to cause the difference in total tagging efficiency. Decay-tree information is not available in data, and so we must use reconstructed quantities instead. To obtain the $\mathfrak{n}_i$ values for data, we use

$$\mathfrak{n}_i = \sum_{j=0}^{N_{Rec}} M_{ij} \cdot n_j, \tag{26}$$

where j is the number of reconstructed tracks that pass the track selection cuts, besides PID, described in Section 6.2.1, n_j is the fraction of events with j reconstructed other-side tracks, and M_{ij} is a matrix obtained from Monte Carlo with columns normalized to unity corresponding to the fraction of events generated with i other-side charged particles and j

well-reconstructed other-side tracks. The number of events with reconstructed other-side multiplicity greater than N_{Rec} is small, but non-zero, and all such events are treated as having $j = 12$. After obtaining the $\mathfrak{n}_i$ for data as described in Equation 26, these are used in Equation 25 to obtain the tagging efficiency after accounting for differences in the other-side multiplicity spectra between data and Monte Carlo. This is done separately for each tag mode, and the difference between this and the nominal efficiency is used as the systematic error, as summarized in Table 15.

Tag Mode	**Other-side Tracks (%)**	**Other-side π^0s (%)**
$D^0 \to K^-\pi^+$	0	0
$D^0 \to K^-\pi^+\pi^0$	0	0
$D^0 \to K^-\pi^+\pi^+\pi^-$	0	0
$D^+ \to K^-\pi^+\pi^+$	0	0
$D^+ \to K^-\pi^+\pi^+\pi^0$	0.66	0.18
$D^+ \to K^0_s\pi^+$	0	0
$D^+ \to K^0_s\pi^+\pi^0$	0.5	0.12
$D^+ \to K^0_s\pi^+\pi^+\pi^-$	1.1	0.14
$D^+ \to K^+K^-\pi^+$	0.3	0

Table 15: Systematic error due to differences in other-side multiplicity between data and Monte Carlo, for both charged tracks and π^0s.

To resolve multiple-candidate events when choosing single-tag events, the best event is chosen based on the ΔE that is most consistent with the single tag having the same energy as the beam. However, this selection is not perfect, and sometimes the wrong candidate is chosen. This has the effect of lowering the efficiency of multiple-candidate events when compared with single-candidate events, because despite a correct reconstruction being available, it is not always chosen in multiple-candidate events. Although a best-candidate selection is also made in double tags when events have multiple double-tag candidates, the smaller number of multiple candidates in double tags, along with the selection variable, $\frac{m_{BC1}+m_{BC2}}{2}$, make the double-tag best-candidate selection less prone to systematic error. Thus, only best-candidate selection for single tags will be considered.

To assess the potential differences between data and Monte Carlo for best-candidate selection, we can define ϵ_s, the efficiency of single-candidate events, ϵ_m the efficiency of multiple candidate events, and F, the fraction of the reconstructed single-tag yield that

comes from multiple-candidate events. The denominators of ϵ_s and ϵ_m are not well-defined because it is impossible to know whether an unreconstructed event would have been a single- or multiple-candidate event, but these quantities are still useful for examining best-candidate selection. The total single-tag efficiency can be written with these quantities as

$$\frac{1}{\epsilon} = \frac{F}{\epsilon_m} + \frac{1-F}{\epsilon_s}. \tag{27}$$

If the difference between data and Monte Carlo efficiencies is assumed to be due to a difference in F, while the efficiencies ϵ_s and ϵ_m are the same, then

$$\Delta\epsilon = \epsilon_{MC} - \epsilon_{data} = (F_{data} - F_{MC})(\epsilon_s - \epsilon_m)\frac{\epsilon_{MC}\epsilon_{data}}{\epsilon_s\epsilon_m}. \tag{28}$$

If F is small, then $\epsilon_{data} \approx \epsilon_s$, and thus

$$\frac{\Delta\epsilon}{\epsilon_{MC}} \approx (F_{data} - F_{MC})(\frac{\epsilon_s}{\epsilon_m} - 1) = (\frac{F_{data}}{F_{MC}} - 1)(\frac{\epsilon_s}{\epsilon_{MC}} - 1). \tag{29}$$

Therefore, a bias is only possible when both the multiple-candidate rate is different between data and Monte Carlo and the single- and multiple-candidate efficiencies are different. F_{data} and F_{MC} can both be measured directly in data and Monte Carlo, and ϵ_{MC} may also be measured with truth-tagging in Monte Carlo. To estimate ϵ_s, we measure the efficiency in Monte Carlo of events with a very low multiple-candidate rate. We choose events that have either $D^0 \to K^-\pi^+$ or $D^+ \to K^-\pi^+\pi^+$, as appropriate, opposite the signal mode to satisfy this criterion. Regardless of the multiple-candidate reconstruction efficiency, the systematic effect is limited by $|F_{MC} - F_{data}|$, so the smaller value between $|F_{MC} - F_{data}|$ and $\Delta\epsilon/\epsilon_{MC}$ is taken as the systematic error associated with best-candidate selection, shown in Table 16.

When taking into account the systematic errors on the mode-dependent measurements of $N_{D\bar{D}}$, we measure $N_{D^0\bar{D}^0} = (10,621 \pm 29(stat) \pm 87(sys)) \times 10^3$ and $N_{D^+D^-} = (8,296 \pm 31(stat) \pm 64(sys)) \times 10^3$. Combining these numbers with the integrated luminosity and its error gives $\sigma_{D^0\bar{D}^0} = (3.641 \pm 0.010(stat) \pm 0.047(sys))$ nb and $\sigma_{D^+D^-} = (2.844 \pm 0.011(stat) \pm 0.036(sys))$ nb.

Tag Mode	$\mathbf{F_{MC}}(\%)$	$\mathbf{F_{data}}(\%)$	$\mathbf{F_{MC} - F_{data}}(\%)$	$\mathbf{\Delta\epsilon/\epsilon_{MC}}(\%)$	**Sys**$(\%)$
$D^0 \to K^-\pi^+$	0.1 ± 0	0.07 ± 0	-0.02 ± 0	-0.23 ± 0.05	0.02
$D^0 \to K^-\pi^+\pi^0$	19.93 ± 0.01	18.97 ± 0.03	-0.96 ± 0	-0.38 ± 0.02	0.38
$D^0 \to K^-\pi^+\pi^+\pi^-$	10.11 ± 0.01	11.76 ± 0.03	1.65 ± 0.01	0.77 ± 0.03	0.77
$D^+ \to K^-\pi^+\pi^+$	1.13 ± 0	1.35 ± 0.01	0.22 ± 0	-0.07 ± 0.02	0.07
$D^+ \to K^-\pi^+\pi^+\pi^0$	24.22 ± 0.02	24.21 ± 0.06	-0.02 ± 0	0 ± 0.01	0
$D^+ \to K^0_s\pi^+$	0.36 ± 0.01	0.39 ± 0.02	0.03 ± 0	-0.09 ± 0.06	0.03
$D^+ \to K^0_s\pi^+\pi^0$	18.51 ± 0.02	18.05 ± 0.06	-0.45 ± 0	-0.04 ± 0.01	0.04
$D^+ \to K^0_s\pi^+\pi^+\pi^-$	22.51 ± 0.03	24.63 ± 0.08	2.12 ± 0.01	0.11 ± 0.03	0.11
$D^+ \to K^+K^-\pi^+$	1.65 ± 0.01	1.81 ± 0.04	0.15 ± 0	-0.02 ± 0.03	0.02

Table 16: The fraction of the single-tag yield that comes from multiple candidate events for both Monte Carlo and data, and the subsequent relative efficiency difference caused by this and the differing single- and multiple-candidate efficiencies. The smaller of $|F_{MC} - F_{data}|$ and $|\Delta\epsilon/\epsilon_{MC}|$ is then taken as the systematic error associated with best-candidate selection.

7 Hadronic Cross Section Measurement

7.1 Hadron selection Cuts

To select hadronic events, we impose a set of cuts designed to reduce backgrounds from sources such as QED events ($e^+e^- \to l\bar{l}, \gamma\gamma$), cosmic rays, beam-gas interactions, and beam-wall interactions. These selection cuts utilize the definition of good tracks and showers as follows:

1. Good charged tracks are required to pass within 1 cm of the interaction point (determined run-by-run) in the plane transverse to the beam direction, and within 10 cm in the direction of the beam axis. They are also required to have $|cos\theta| < 0.93$, where θ is the polar angle in the MDC.

2. Good photons are required to have a minimum energy deposited in the EMC of 25 MeV in the barrel region ($|cos\theta| < 0.8$), and a minimum of 50 MeV in the end cap region ($0.86 < |cos\theta| < 0.92$), and must pass a TDC timing cut (0 ns $\leq time \leq 14 \cdot 50$ ns).

All events are subjected to a set of cuts to reject backgrounds from Bhabha and two-photon fusion events, summarized in Table 17. The polar angle cuts take advantage of the charge asymmetry of the colliding beams and the fact that Bhabha and two-photon events are likely to change the momenta of the beam particles by only a small amount. The E/p cuts are able to discriminate between electrons and other charged particles because only electrons deposit the majority of their energy in the EMC. The p/E_{beam} cuts veto Bhabha and two-photon fusion events because the majority of the beam-energy will be kept by the beam particles in such events, while other kinds of events will have a higher multiplicity and spread the beam-energy more evenly between several particles. The cuts are looser for events with more than two good tracks because Bhabha and two-photon fusion events are low multiplicity events.

After applying the Bhabha/two-photon fusion rejection, we apply three additional sets of cuts to select hadronic events, with varying levels of stringency. The intermediate set of cuts is the standard hadronic event selection (SHAD) and is used to determine the central value of our measurement. The other two sets of cuts are looser (LHAD) and tighter (THAD) than our standard hadronic event selection cuts and are used to evaluate the systematic error associated with hadronic event selection. These selection criteria are summarized in Table 18. These cuts are designed to primarily suppress QED events, beam-gas interactions and beam-wall interactions. Beam-gas and beam-wall interactions are suppressed through

$\mathbf{N_{Trk}}$	**Bhabha/two-photon rejection**
2	$\cos\theta^+ < 0.8$, $\cos\theta^- > -0.8$, $(E/p)^+_{Trk1} < 0.8$ or $(E/p)^+_{Trk1} > 1.1$, $(E/p)^-_{Trk1} < 0.8$ or $(E/p)^-_{Trk1} > 1.1$
3,4	$\cos\theta^+ < 0.8$ or $p^+_{Trk1}/E_{beam} > 0.8$, $\cos\theta^- > -0.8$ or $p^-_{Trk1}/E_{beam} > 0.8$, $(E/p)^-_{Trk1} < 0.8$ or $(E/p)^-_{Trk1} > 1.1$, $(E/p)^+_{Trk1} < 0.8$ or $(E/p)^+_{Trk1} > 1.1$

Table 17: Events are rejected if they do not meet the requirements above. E_{beam} is the beam energy, $\cos\theta^{\pm}$ corresponds to the cosine of the polar angles of the most energetic positive and negative charged tracks, and $p^{\pm}_{Trk1}$ and $E^{\pm}_{Trk1}$ are the momenta from the MDC and energies deposited in the EMC, respectively, of the highest energy positive and negative charged tracks.

a variety of cuts that take advantage of the fact that such events will be missing the energy and momentum of one of the beams and also have a large net momentum in the z-direction. QED events are limited mainly by the good track multiplicity requirements. Requirements that a single particle not contain most of the beam energy/momentum also suppress QED events. The hadronic selection cuts are increasingly loose as a function of good track multiplicity because hadronic events are typically higher multiplicity events. The largest difference between the various hadronic selection cuts is the good track multiplicity required to pass that particular set of cuts.

7.2 Determination of Background Cross Sections

We must determine the cross section of the various events used in our Monte Carlo samples to model the data, both to provide the normalization of the backgrounds described in Section 4 that will be subtracted based on Monte Carlo, and to insure that we understand our data well.

Although we will not be using $q\bar{q}$ MC in our final analysis, determination of its cross section is important for an initial comparison of data and Monte Carlo. We estimate the observed $q\bar{q}$ cross section at $E_{cm} = 3.65$ GeV using the following formula:

$$R(3650) = \frac{\sigma_{q\bar{q}}}{(1+\delta) * \sigma^0_{\mu\mu}}, \tag{30}$$

where $R(3650) = 2.2$ is the R value taken from the PDG [3] at 3.65 GeV, $1+\delta = 1.319840$ is the radiative correction at 3.65 GeV taken from the KKMC generator output and $\sigma^0_{\mu\mu} = 6.52$

$\mathbf{N_{Trk}}$	**SHAD**
0,1	rejected
2	rejected
3	$E_{vis}/E_{cm} > 0.3$, $E_{EMC}/E_{cm} > 0.25$, $E_{EMC}/E_{cm} < 0.75$ or $E_{Shw1}/E_{beam} < 0.75$, $\lvert p_z/E_{vis}\rvert < 0.6$
4	$E_{vis}/E_{cm} > 0.3$, $E_{EMC}/E_{cm} > 0.15$, $E_{EMC}/E_{cm} < 0.75$ or $E_{Shw1}/E_{beam} < 0.75$, $\lvert p_z/E_{vis}\rvert < 0.6$
4+	$E_{vis}/E_{cm} > 0.3$

$\mathbf{N_{Trk}}$	**LHAD**
0,1	rejected
2	$E_{vis}/E_{cm} > 0.4$, $0.25 < E_{EMC}/E_{cm} < 0.75$, $E_{Shw1}/E_{beam} < 0.5$, $p_{Trk1}/E_{beam} < 0.75$, $\lvert p_z/E_{vis}\rvert < 0.3$
3	$E_{vis}/E_{cm} > 0.3$, $E_{EMC}/E_{cm} > 0.25$, $E_{EMC}/E_{cm} < 0.75$ or $E_{Shw1}/E_{beam} < 0.75$, $\lvert p_z/E_{vis}\rvert < 0.6$
4	$E_{vis}/E_{cm} > 0.3$, $E_{EMC}/E_{cm} > 0.15$, $E_{EMC}/E_{cm} < 0.75$ or $E_{Shw1}/E_{beam} < 0.75$, $\lvert p_z/E_{vis}\rvert < 0.6$
4+	$E_{vis}/E_{cm} > 0.3$

$\mathbf{N_{Trk}}$	**THAD**
0,1	rejected
2,	rejected
3,	rejected
4	$E_{vis}/E_{cm} > 0.4$, $E_{EMC}/E_{cm} > 0.15$, $E_{EMC}/E_{cm} < 0.75$ or $E_{Shw1}/E_{beam} < 0.75$, $\lvert p_z/E_{vis}\rvert < 0.6$
5	$E_{vis}/E_{cm} > 0.4$, $E_{EMC}/E_{cm} < 0.75$ or $E_{Shw1}/E_{beam} < 0.75$
5+	$E_{vis}/E_{cm} > 0.4$

Table 18: Event selection requirements for SHAD, LHAD and THAD: N_{Trk} is the number of good tracks in the event, E_{cm} is the center of mass energy, E_{beam} is the beam energy, E_{vis} is the visible energy (both charged and neutral), E_{EMC} is the sum of energy in the EMC for good photons and good tracks, E_{Shw1} is the shower energy for the most energetic shower from among the good photons and good tracks, p_z is the net visible momentum (both charged and neutral) in the z-direction, and E_{Trk1} is the highest track momentum.

pb is the $\mu\bar{\mu}$ Born cross section, determined from

$$\sigma^0_{\mu\mu} = \frac{4\pi\alpha^2}{3s} = \frac{86.8 \text{ nb}}{s \text{ (GeV}^2)}, \tag{31}$$

where s is the center-of-mass energy squared, and α is the electromagnetic coupling constant.

The cross sections of $\tau\bar{\tau}$, Bhabha, $\mu\bar{\mu}$, $\gamma\gamma$ and two-photon fusion events are taken directly from the output of the Babayaga and KKMC generators used to create these Monte Carlo samples.

The cross section of radiative return to $\psi(3686)$ at 3.773 GeV is derived from a data-driven method. We take the cross section of $e^+e^- \to \gamma\psi(3686), \psi(3686) \to \pi^+\pi^- J/\psi$, $(1036 \pm 13 \pm 23)$ pb, measured by CLEO-c [22] and the branching ratio of $\psi(3686) \to \pi^+\pi^- J/\psi$, $(34.43 \pm 0.30)\%$, calculated by averaging the PDG world average [3] and the recent BESIII measurement [64] to obtain the cross section of $e^+e^- \to \gamma\psi(3686)$ at 3.773 GeV with

$$\sigma_{\gamma\psi(3686)} = \frac{\sigma_{\gamma\psi(3686),\psi(3686)\to\pi^+\pi^- J/\psi}}{\mathcal{B}(\psi(3686) \to \pi^+\pi^- J/\psi)} = 3009 \pm 81 \text{ pb}. \tag{32}$$

We also theoretically calculate the cross sections of radiative return to J/ψ and $\psi(3686)$ based on Ref. [65]. The theoretical cross section of J/ψ is used in the background subtractions. The theoretical cross section of $\psi(3686)$ is used to study the systematic error of the data-driven calculation. The Breit–Wigner formula for these cross sections is given by

$$\sigma_B(s) \ = \frac{12\pi\Gamma^0_{ee}\Gamma}{(s - M^2)^2 + \Gamma^2 M^2}, \tag{33}$$

where M and Γ are the mass and total width of the respective resonance; Γ^0_{ee} is the partial width to e^+e^- of the respective resonance. The radiatively corrected resonance cross section is then given by

$$\sigma_{res}(s) = \int_0^1 dx \ F(x,s) \frac{12\pi\Gamma^{exp}_{ee}\Gamma}{(s - M^2)^2 + \Gamma^2 M^2}. \tag{34}$$

Here we calculate $F(x,s)$ in terms of a series expansion:

$$\begin{aligned} F(x,s) &= \beta x^{\beta-1}\left[1+\frac{3}{4}\beta+\frac{\alpha}{\pi}\left(\frac{\pi^2}{3}-\frac{1}{2}\right)+\beta^2\left(\frac{9}{32}-\frac{\pi^2}{12}\right)\right] \\ &\quad +x^{\beta}\left(-\beta-\frac{\beta^2}{4}\right)+x^{\beta+1}\left(\frac{\beta}{2}-\frac{3}{8}\beta^2\right)+O(x^{\beta+2}\beta^2) \\ &= \beta x^{\beta-1}\delta^{V+S}+\delta^{H}, \end{aligned} \tag{35}$$

with

$$\delta^{H} = x^{\beta}\left(-\beta-\frac{\beta^2}{4}\right)+x^{\beta+1}\left(\frac{\beta}{2}-\frac{3}{8}\beta^2\right). \tag{36}$$

7.3 Data/MC Comparison at 3.65 GeV

Using the Monte Carlo samples described in Section 5, and normalizing them to the cross sections described in Section 7.2, we can probe our data/MC consistency, both before and after our hadronic selection cuts for the 2009 data at 3.65 GeV. Figures 27-31 show the comparisons between data and MC for the cut variables used in our hadronic event selection cuts, described in Section 7.1, before any hadronic event selection cuts are applied. The plots are divided into bins based on good charged track multiplicity and show contributions from the various Monte Carlo physics processes. Figure 32 shows the good charged track multiplicity spectrum. The Bhabha/two-photon fusion rejection has been applied to all figures. The excess of data over Monte Carlo is attributable to beam-gas and beam-wall interactions that are not simulated in Monte Carlo.

Figures 33-37 show the same distributions as Figures 27-31, with the additional requirement of passing the loose hadronic event selection (LHAD) cuts. The LHAD set of cuts is chosen in this case because it is the only set of cuts that allows a good track multiplicity of two. These plots show that our hadronic event selection cuts successfully reject QED backgrounds and the unsimulated beam-gas and beam-wall backgrounds.

Figure 38 shows the data/MC comparisons for the good charged track multiplicity spectra, for the SHAD, LHAD, and THAD hadronic event selection cuts after applying the Bhabha/two-photon fusion rejection. Table 19 shows the Monte Carlo efficiencies and expected number of events for the various physics processes for each set of hadronic selection cuts.

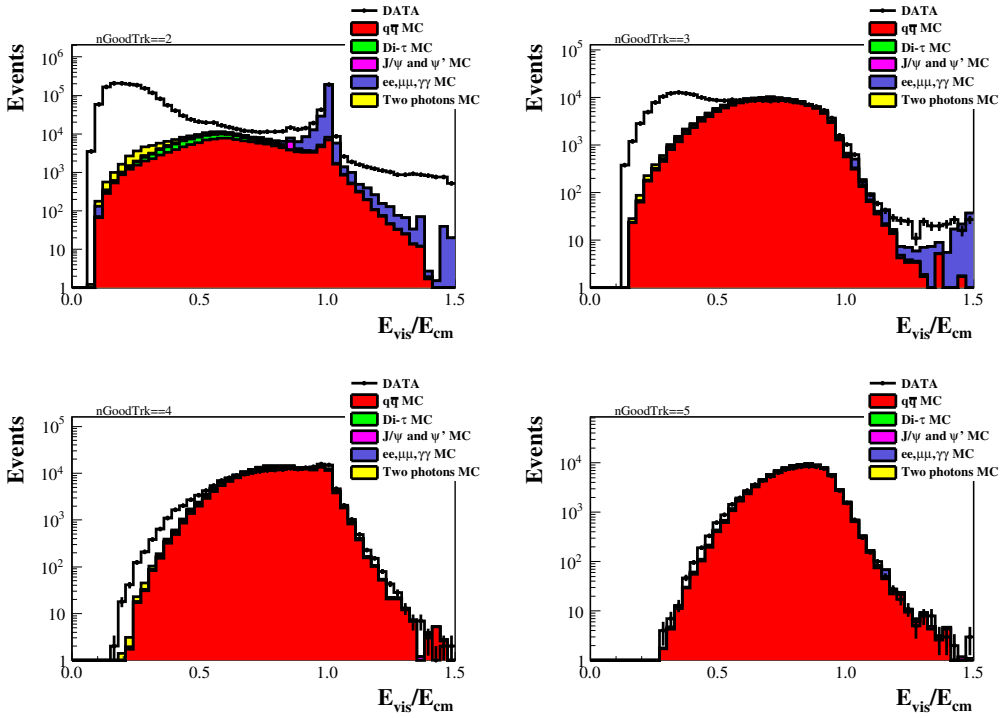

Figure 27: E_{vis}/E_{cm} by good charged track multiplicity for 2009 data at 3.65 GeV, only Bhabha/two-photon fusion cuts applied.

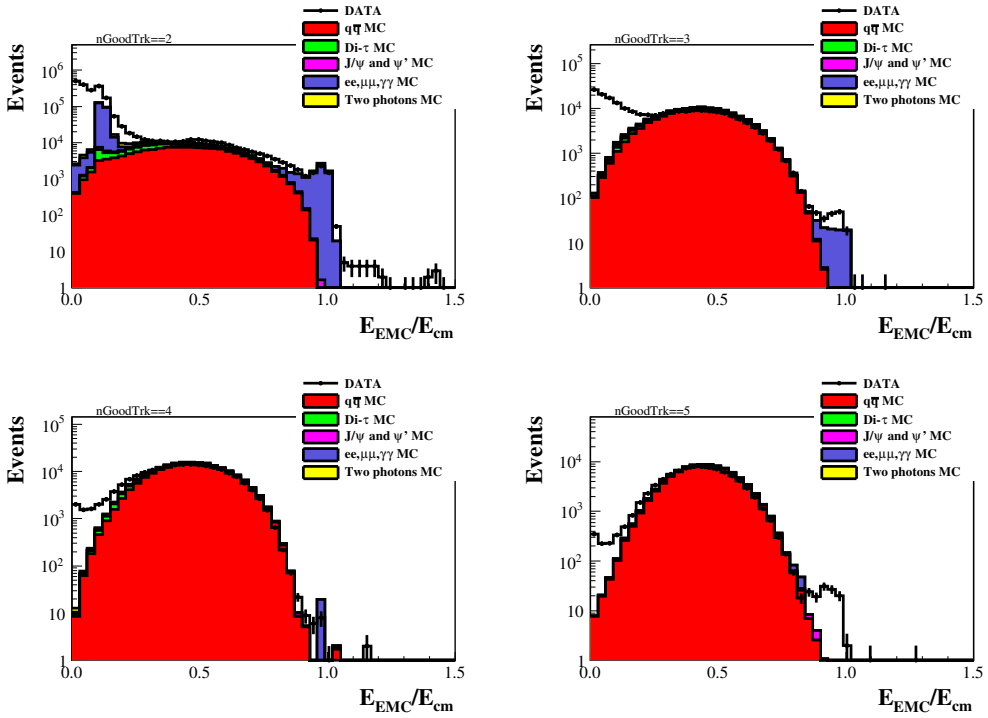

Figure 28: E_{EMC}/E_{cm} by good charged track multiplicity for 2009 data at 3.65 GeV, only Bhabha/two-photon fusion cuts applied.

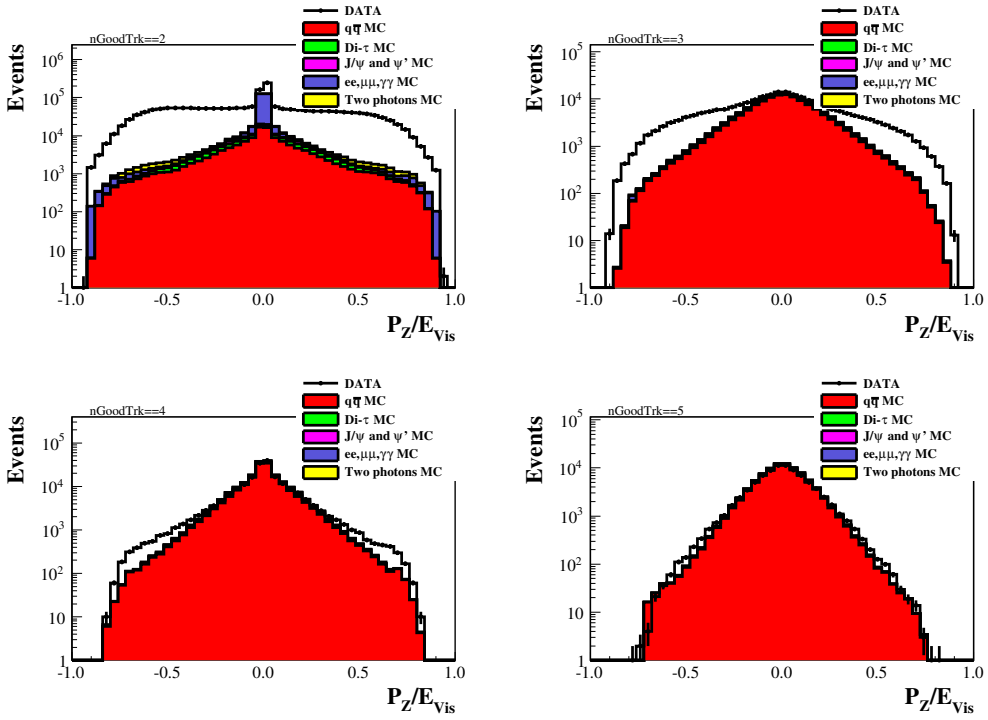

Figure 29: p_z/E_{vis} by good charged track multiplicity for 2009 data at 3.65 GeV, only Bhabha/two-photon fusion cuts applied.

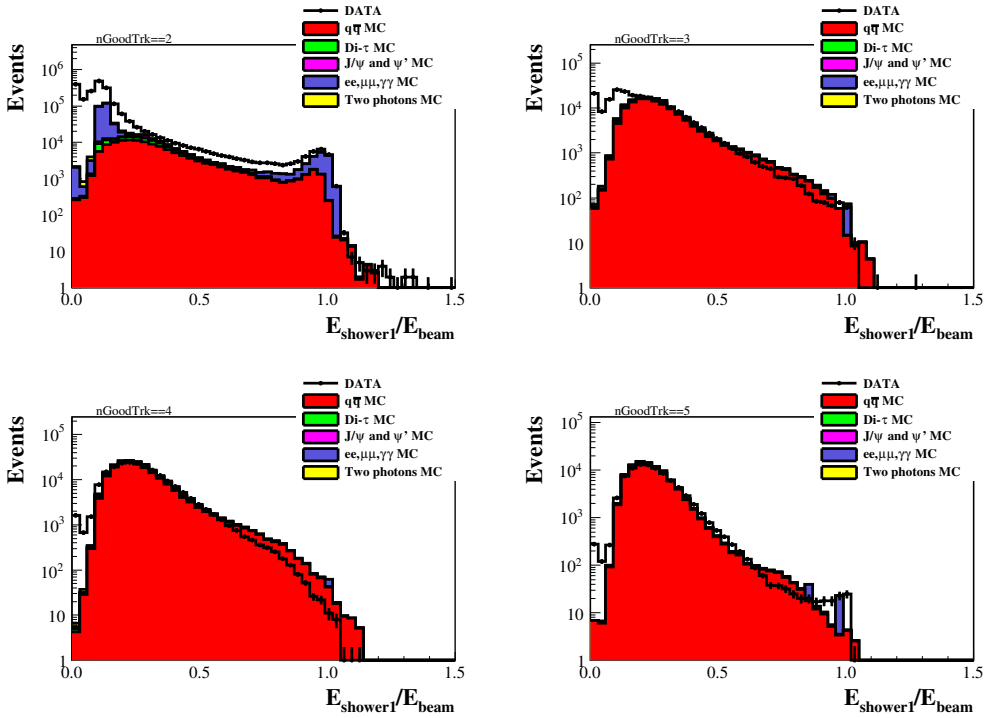

Figure 30: E_{Shw1}/E_{beam} by good charged track multiplicity for 2009 data at 3.65 GeV, only Bhabha/two-photon fusion cuts applied.

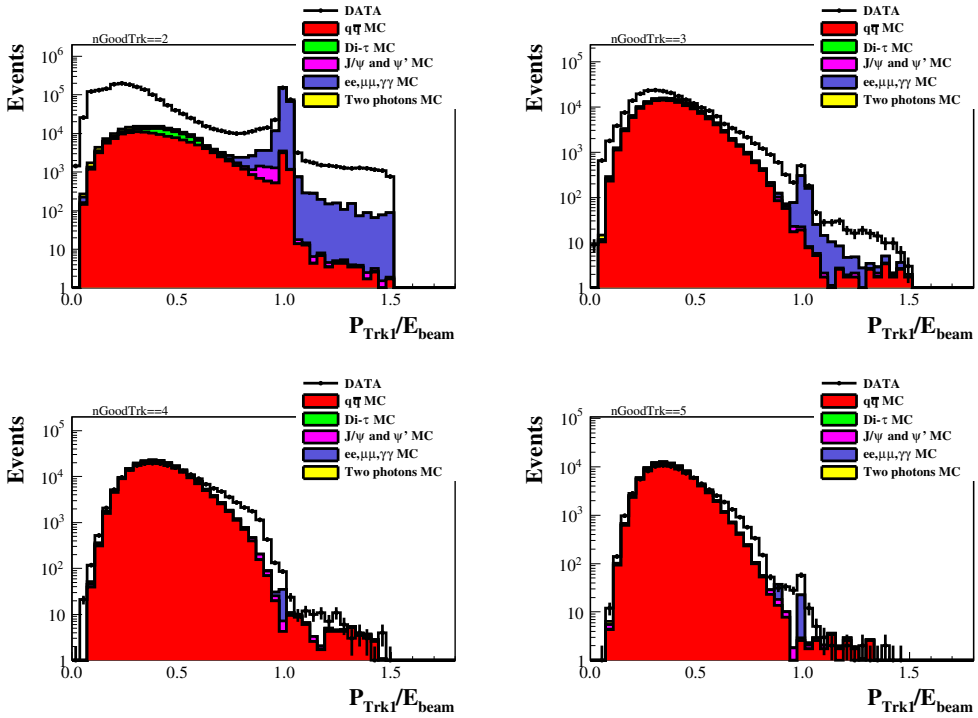

Figure 31: p_{Trk1}/E_{beam} by good charged track multiplicity for 2009 data at 3.65 GeV, only Bhabha/two-photon fusion cuts applied.

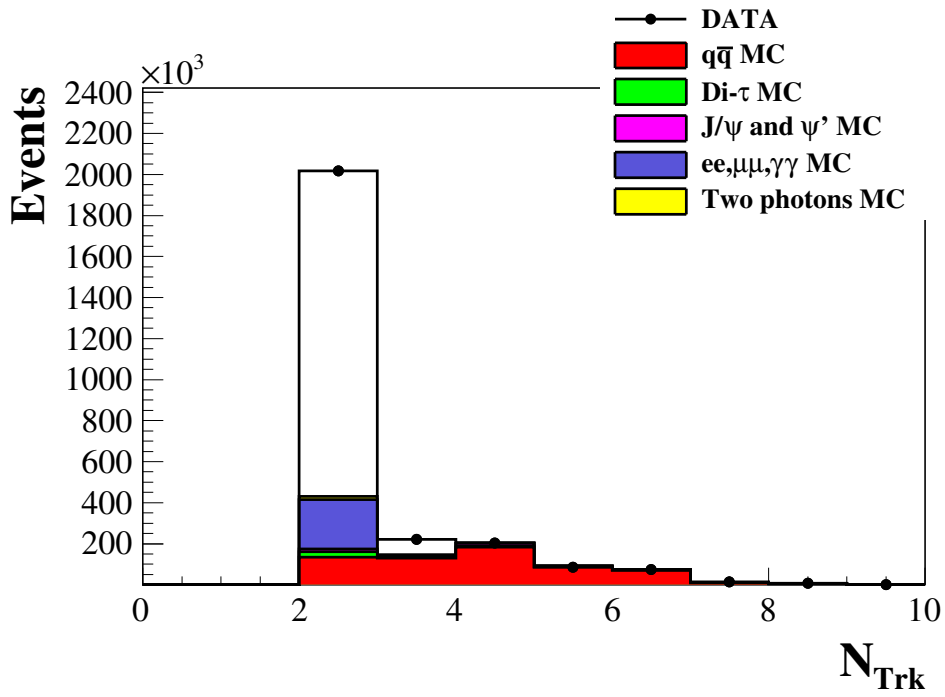

Figure 32: N_{Trk} at 3.65 GeV with only Bhabha/two-photon fusion cuts applied.

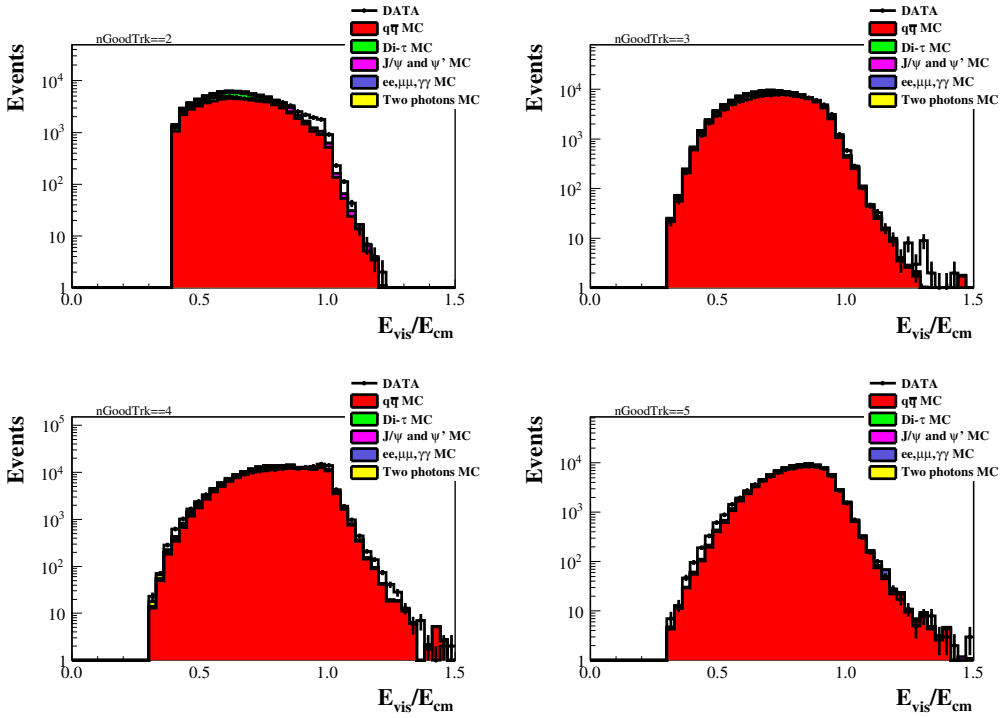

Figure 33: E_{vis}/E_{cm} by good charged track multiplicity for 2009 data at 3.65 GeV, after LHAD and Bhabha/two-photon fusion cuts are applied.

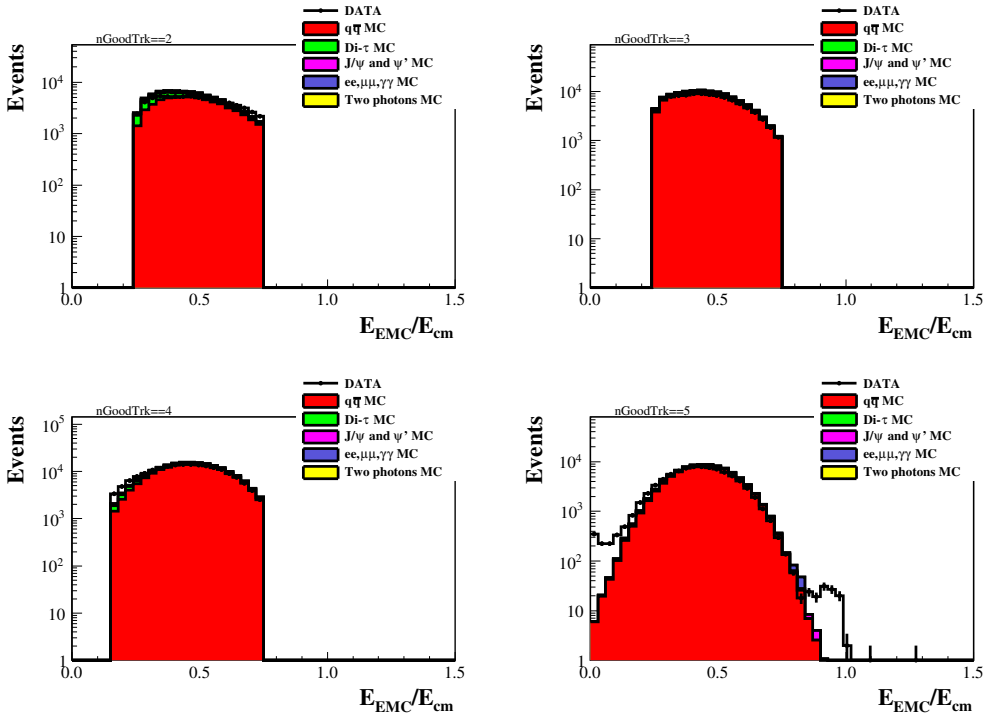

Figure 34: E_{EMC}/E_{cm} by good charged track multiplicity for 2009 data at 3.65 GeV, after LHAD and Bhabha/two-photon fusion cuts are applied.

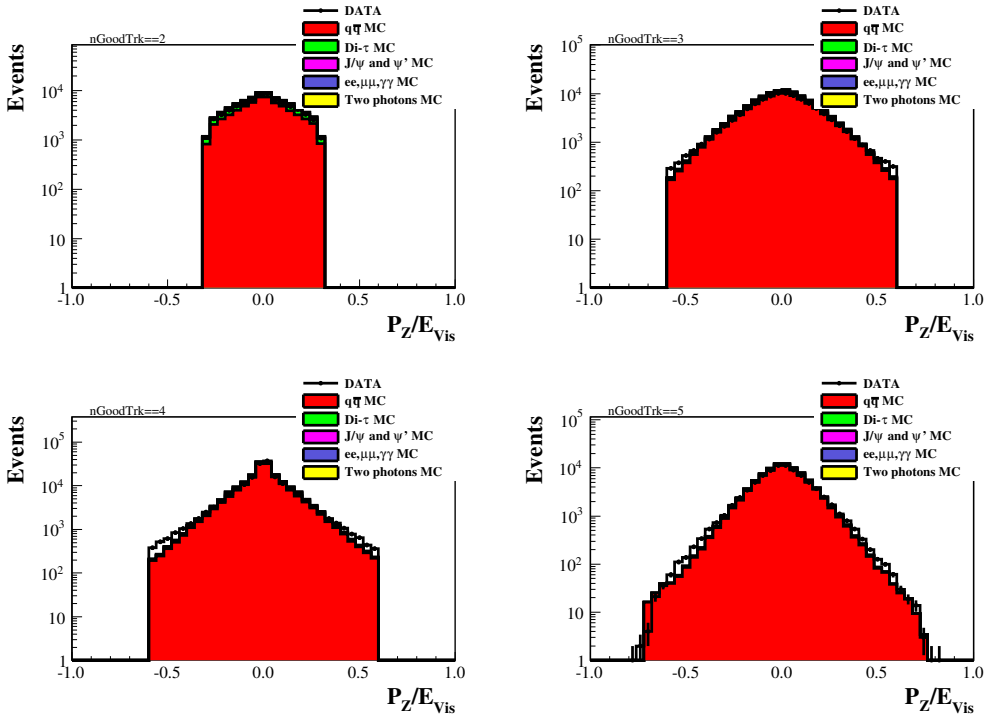

Figure 35: p_z/E_{vis} by good charged track multiplicity for 2009 data at 3.65 GeV, after LHAD and Bhabha/two-photon fusion cuts are applied.

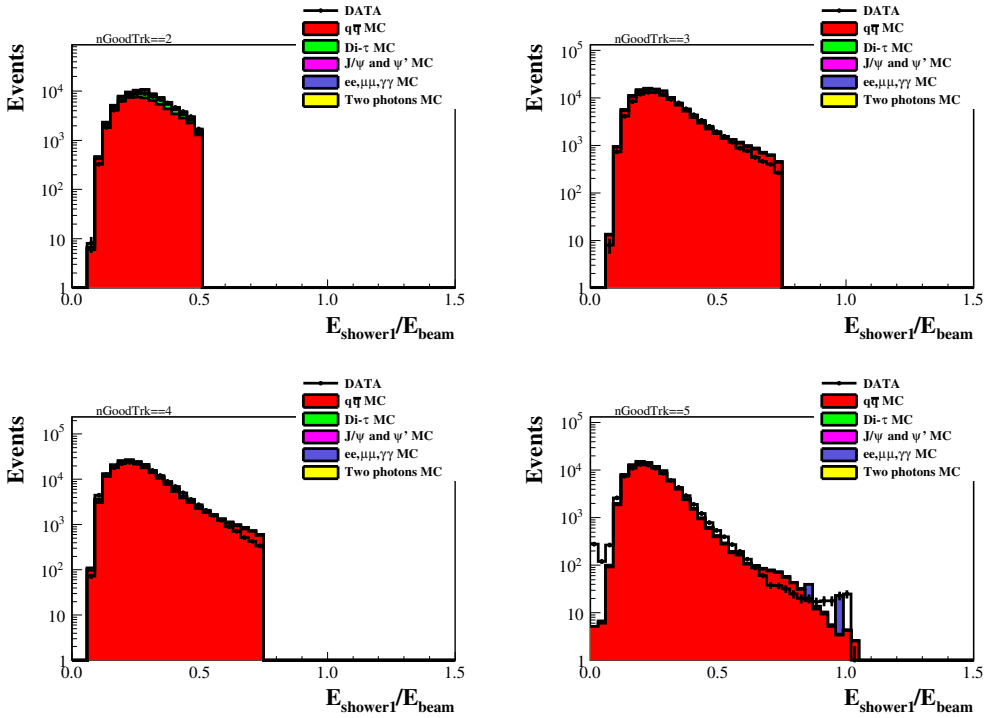

Figure 36: E_{Shw1}/E_{beam} by good charged track multiplicity for 2009 data at 3.65 GeV, after LHAD and Bhabha/two-photon fusion cuts are applied.

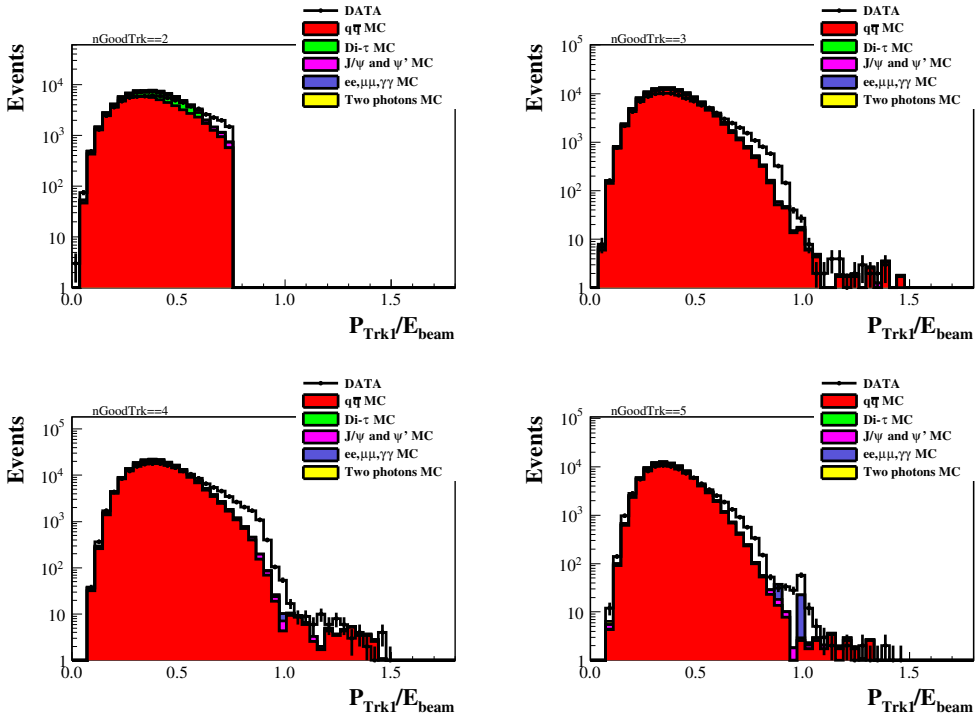

Figure 37: p_{Trk1}/E_{beam} by good charged track multiplicity for 2009 data at 3.65 GeV, after LHAD and Bhabha/two-photon fusion cuts are applied.

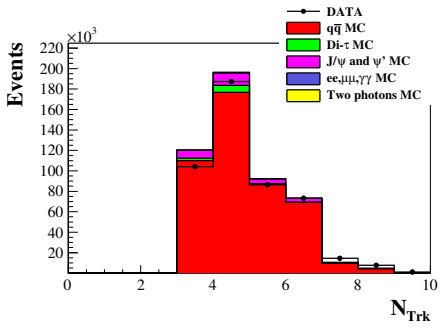

(a) SHAD

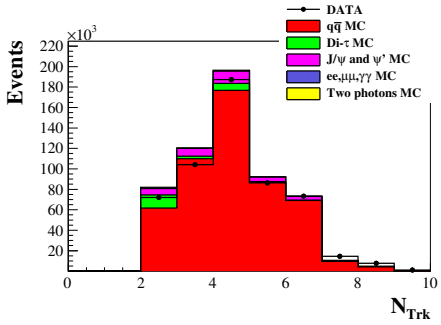

(b) LHAD

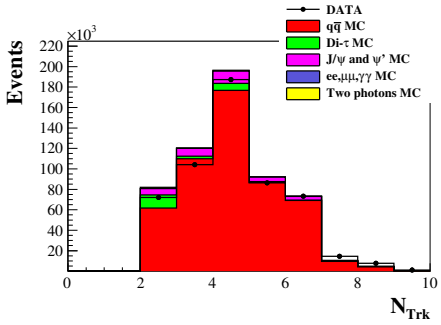

(c) THAD

Figure 38: N_{Trk} at 3.65 GeV after the various hadronic event selection cuts.

SHAD			
Channel	σ **(pb)**	**Efficiency (%)**	**Yield** ($\times\mathbf{10^3}$)
$q\bar{q}$	19.230	53.403 ± 0.050	456.89 ± 0.43
$\tau\bar{\tau}$	1.844	12.264 ± 0.033	10.059 ± 0.027
$\gamma J/\psi$	1.260	43.917 ± 0.050	24.624 ± 0.028
Bhabha	554.562	0.0003 ± 0.0002	0.058 ± 0.033
$\mu\bar{\mu}$	5.560	0.0039 ± 0.0006	0.010 ± 0.002
$\gamma\gamma$	21.530	0.0009 ± 0.0003	0.009 ± 0.003
$2\gamma - fus$	1.257	2.212 ± 0.015	1.237 ± 0.008
LHAD			
Channel	σ **(pb)**	**Efficiency (%)**	**Yield** ($\times\mathbf{10^3}$)
$q\bar{q}$	19.230	60.618 ± 0.049	518.61 ± 0.42
$\tau\bar{\tau}$	1.844	27.904 ± 0.045	22.887 ± 0.037
$\gamma J/\psi$	1.260	54.468 ± 0.050	30.540 ± 0.028
Bhabha	554.562	0.0005 ± 0.0002	0.096 ± 0.043
$\mu\bar{\mu}$	5.560	0.0047 ± 0.0007	0.012 ± 0.002
$\gamma\gamma$	21.530	0.0010 ± 0.0003	0.010 ± 0.003
$2\gamma - fus$	1.257	4.395 ± 0.021	2.458 ± 0.011
THAD			
Channel	σ **(pb)**	**Efficiency (%)**	**Yield** ($\times\mathbf{10^3}$)
$q\bar{q}$	19.230	40.468 ± 0.049	346.22 ± 0.42
$\tau\bar{\tau}$	1.844	9.215 ± 0.029	7.560 ± 0.024
$\gamma J/\psi$	1.260	30.994 ± 0.046	17.378 ± 0.026
Bhabha	554.562	0.0001 ± 0.0001	0.019 ± 0.019
$\mu\bar{\mu}$	5.560	0.0032 ± 0.0006	0.008 ± 0.001
$\gamma\gamma$	21.530	0.0006 ± 0.0002	0.006 ± 0.002
$2\gamma - fus$	1.257	1.488 ± 0.012	0.832 ± 0.007

Table 19: Hadronic event selection efficiencies and expected number of background events for the various hadronic event selection criteria for the 3.65 GeV continuum from 2009.

7.4 $\frac{1}{s}$ Efficiency Extrapolation

7.4.1 Motivation

Along with $\psi(3770) \to D\bar{D}$, $q\bar{q}$ is the dominant background in this analysis, so special care must be taken when subtracting this background. We use a data-driven method to scale the 2009 continuum data taken at 3.65 GeV to the 3.773 GeV energy point where we are measuring $\mathcal{B}(\psi(3770) \to non - D\bar{D})$, as shown in Equation 11. The 3.65 GeV energy point is chosen because it does not have contamination from radiative return to $\psi(3686)$, nor from the $\psi(3770)$ resonance. This data also has sufficient statistics and run conditions similar to the first round of $\psi(3770)$ data that make it a good data set from which to estimate our $q\bar{q}$ contribution.

Because of its small value [3], the branching ratio for non-$D\bar{D}$ is sensitive to the ratio used to scale the $q\bar{q}$ contribution. Unfortunately, neither of the two $q\bar{q}$ Monte Carlo generators used at BESIII model our data very well. The two $q\bar{q}$ generators are also inconsistent with each other when used to obtain the hadronic event selection efficiency ratio, differing by $\sim 4\%$. Given that the cross section of $q\bar{q}$ is about double that of $D\bar{D}$, an inconsistency in this efficiency ratio leads to a large systematic uncertainty in $\mathcal{B}(\psi(3770) \to non - D\bar{D})$, exceeding all the other systematic sources. With this level of uncertainty we can neither confirm nor exclude non-zero non-$D\bar{D}$. For this reason, we use additional continuum data to extrapolate the $q\bar{q}$ efficiency as a function of energy.

7.4.2 Method Validation

The hadronic event selection efficiency of $\frac{1}{s}$ background events as a function of E_{cm} is a smooth curve, so we can use continuum data away from resonances and fit for the relative efficiency ratios, then extrapolate to 3773 MeV. For a certain energy point with $E_{cm} = x$ MeV, the efficiency ratio can be determined as

$$\frac{\epsilon(x)}{\epsilon(3650)} = \frac{N(x)/\mathcal{L}(x)}{N(3650)/\mathcal{L}(3650)} \cdot \frac{x^2}{3650^2}, \tag{37}$$

where $N(x)$ is the selected number of hadronic events and $\mathcal{L}(x)$ is the integrated luminosity at $E_{cm} = x$ MeV.

To validate our method, we simulate Monte Carlo for five energy points each with an integrated luminosity of 4 pb^{-1}, apply hadronic event selection cuts, and then fit to the ratio of efficiencies. This validation study was done before the five points of data were taken, so the integrated luminosities in this study are not quite the same as those in our

data. In particular, the middle point only has an integrated luminosity of 0.4 pb^{-1}. The E_{cm} values for these energy points are 3500 MeV, 3542 MeV, 3600 MeV, 3650 MeV, and 3671 MeV. There are no points above $E_{cm} = 3686$ MeV because the radiative return to $\psi(3686)$ would introduce an additional large background.

Figure 39 shows the performance of linear and quadratic extrapolations using MC with five energy points. From the 2009 continuum data at 3.65 GeV, we concluded that 4 pb^{-1} for each energy point would provide about 4×10^4 hadronic events passing our standard selection, and the statistical errors for each energy point in this MC study were set accordingly. The $\chi^2/d.o.f.$ of the linear fit is 1.9/3 and the statistical error for the extrapolation to 3773 MeV is 0.6%. The value of $\frac{\epsilon(3773)}{\epsilon(3650)}$ calculated directly from Monte Carlo is consistent with the extrapolation within error. The statistical error of this extrapolation leads to a systematic error in the branching ratio of non-$D\bar{D}$ about twice as large. The $\chi^2/d.o.f.$ of the alternative quadratic fit is 1.8/2 and the difference between the linear and the quadratic fit at 3773 MeV is 0.3%, which is assigned as a systematic error.

7.4.3 Bhabha Integrated Luminosity Calculation

To use the five continuum data points taken in 2013 and described in Section 5, we must have an accurate and consistent measurement of our samples' integrated luminosities. We also measure the integrated luminosity of the $\psi(3770)$ and 2009 continuum data samples, despite availability of official integrated luminosity measurements for these samples, in order to have a measurement of integrated luminosity that is consistent across all of the data we use. The Bhabha scattering process ($e^+e^- \to e^+e^-$) provides a high statistics, clean and theoretically well understood process to perform such a measurement. To select Bhabha events, we impose selection criteria as described below.

- Two good tracks with matched EMC clusters.
- The polar angle of each track satisfies $|\cos\theta| < 0.8$
- The energy deposited in the EMC for each track is greater than 0.2 GeV.
- $\frac{E_{EMC}}{p} > 0.7$, for each track.
- The angle between the EMC clusters of the two tracks is greater than 165°.

The integrated luminosity is then calculated as

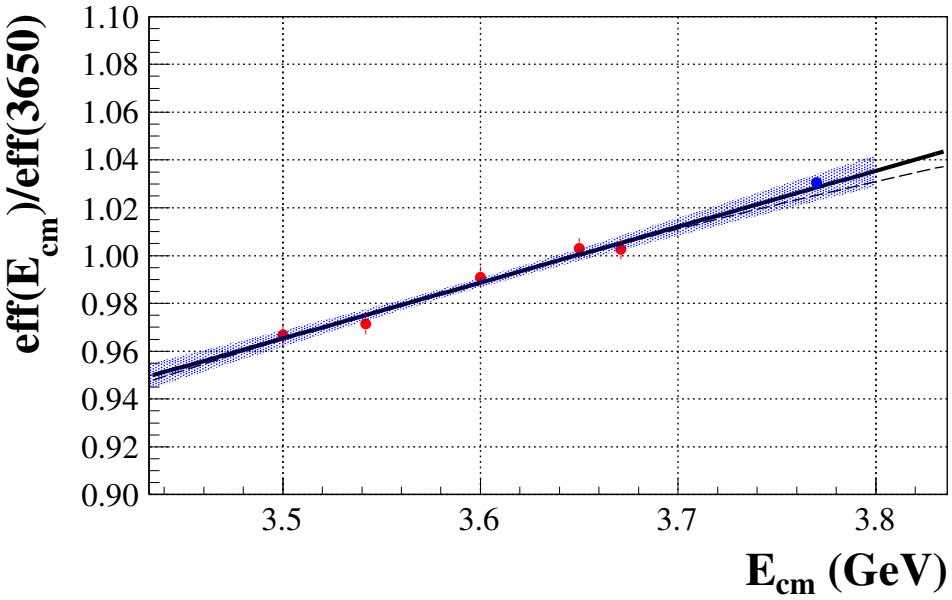

Figure 39: The selection-efficiency ratio in MC with five energy points are fit using linear (solid) and quadratic (dashed) fits and extrapolated to the 3.773 GeV MC point. The one sigma statistical error band is shown for the linear fit.

$$\mathcal{L} = \frac{N_{Bhabha}}{\sigma_{Bhabha}\epsilon_{Bhabha}}, \tag{38}$$

where N_{Bhabha} is the number of events passing the Bhabha selection criteria, ϵ_{Bhabha} is determined from the MC described in Section 5, and σ_{Bhabha} is the cross section obtained directly from the Babayaga output used to generate the Monte Carlo.

As an example, a data/MC overlay for the angle between e^+ and e^- clusters at 3.65 GeV in the 2013 continuum sample is shown in Figure 40. The results of this integrated luminosity measurement are listed in Table 20. The integrated luminosity measurements for the 3.65 GeV continuum data taken in 2009, and the first and second rounds of $\psi(3770)$ data are consistent with the official integrated luminosity measurement [59] at the 0.5% level.

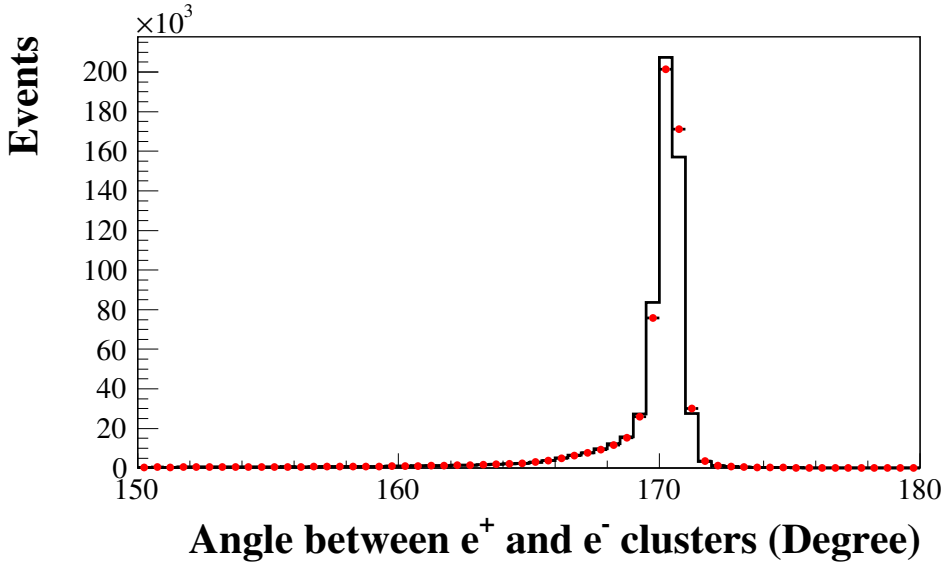

Figure 40: The angle between e^+ and e^- clusters at 3.65 GeV in the 2013 continuum sample is plotted. Data is represented by points, and Monte Carlo by the histogram. Although the agreement is imperfect, it does not introduce an appreciable systematic uncertainty with the selection criteria that are used.

$\mathbf{E_{cm}}$ **(GeV)**	$\mathbf{N_{Bhabha}}(\times\mathbf{10^3})$	$\sigma_{\mathbf{Bhabha}}$ **(pb)**	$\epsilon_{\mathbf{Bhabha}}(\%)$	$\mathcal{L}$ **(pb^{-1})**
3.500	422.51 ± 0.65	602.729	19.048 ± 0.039	3.680 ± 0.009
3.542	503.00 ± 0.71	588.401	19.079 ± 0.039	4.4806 ± 0.009
3.600	42.99 ± 0.21	569.943	19.102 ± 0.039	0.395 ± 0.019
3.650	574.50 ± 0.76	554.562	19.115 ± 0.039	5.420 ± 0.009
3.671	489.87 ± 0.70	548.173	19.141 ± 0.039	4.669 ± 0.009
3.650 from 2009	4705.32 ± 2.17	554.562	19.138 ± 0.039	44.334 ± 0.093
First round $\psi(3770)$	91444.2 ± 9.56	518.607	19.023 ± 0.039	926.922 ± 0.094
Second round $\psi(3770)$	197739 ± 14.06	518.607	19.268 ± 0.039	1978.92 ± 0.091

Table 20: The integrated luminosity by data sample is shown. The first five points are from the 2013 continuum data.

7.4.4 Extrapolation Results

To extrapolate our hadronic event selection efficiency across the five continuum points taken in 2013 and scale to the continuum data from 2009, we must measure the number of events passing the hadronic event selection cuts and subtract off the appropriate backgrounds. To measure the number of events passing hadronic selection cuts, we apply the SHAD cuts (and later the LHAD and THAD for determination of systematic error) and then fit the average track V_z, where V_z is the point of closest approach to the interaction point in the z-direction. The fit provides a means to separate the contribution of non-physics events like cosmic rays and beam backgrounds from the hadronic events we want to measure. We use a double Gaussian to describe the signal shape and a 2^{nd} order polynomial to describe the background shape. Because the five continuum data points are taken in the same period, the background level and shape should be similar among the energy points. Accordingly, we simultaneously fit to the five points of the new continuum data, using the same signal and background shapes while floating signal and background yields for each point. We independently fit the 3.65 GeV continuum data from 2009. The fits to the average track V_z for these samples with SHAD cuts are found in Figure 41. The extracted hadron yields and signal to background ratios under SHAD, LHAD and THAD are found in Table 21. The background levels ($N(signal)/N(total)$) are fairly consistent across the 2013 continuum data points.

Once the vertex distributions are fitted, we then subtract off the radiative return to

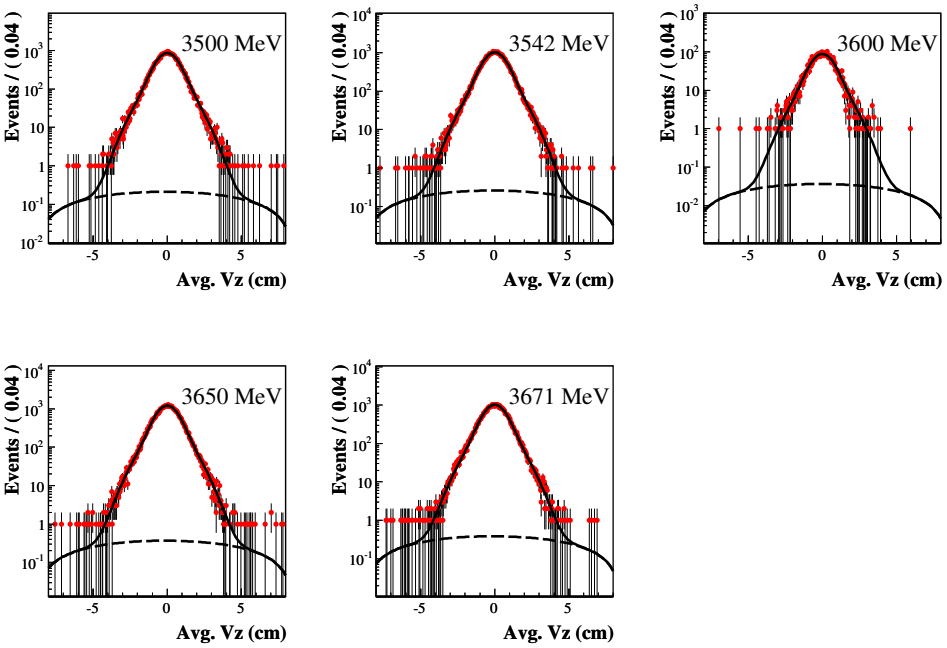

(a) Five continuum energy points taken in 2013

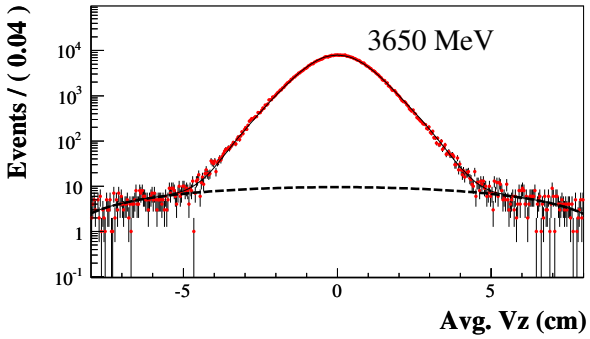

(b) 3.65 GeV data taken in 2009

Figure 41: Fit of average V_z. Simultaneous fits to the five energy points from 2013 continuum data (a) and the independent fit for 3.65 GeV data taken in 2009 (b). SHAD and Bhabha/two-photon cuts have been applied.

SHAD		
E_{cm} (GeV)	**N(signal)**	**N(signal)/N(total)**
3.500	41987 ± 196	0.9986 ± 0.0047
3.542	50107 ± 208	0.9985 ± 0.0041
3.600	4302 ± 63	0.9976 ± 0.0146
3.650	58557 ± 239	0.9982 ± 0.0041
3.671	49805 ± 218	0.9978 ± 0.0044
3.650 old	471759 ± 687	0.9939 ± 0.0003

LHAD		
E_{cm} (GeV)	**N(signal)**	**N(signal)/N(total)**
3.500	47794 ± 220	0.9965 ± 0.0046
3.542	56616 ± 240	0.9965 ± 0.0042
3.600	4964 ± 71	0.9952 ± 0.0142
3.650	66829 ± 260	0.9963 ± 0.0039
3.671	56786 ± 240	0.9959 ± 0.0042
3.650 from 2009	542242 ± 765	0.9919 ± 0.0004

THAD		
E_{cm} (GeV)	**N(signal)**	**N(signal)/N(total)**
3.500	32891 ± 186	0.9986 ± 0.0056
3.542	39341 ± 195	0.9987 ± 0.0050
3.600	3428 ± 58	0.9988 ± 0.0169
3.650	46370 ± 229	0.9987 ± 0.0049
3.671	39432 ± 191	0.9983 ± 0.0048
3.650 from 2009	367156 ± 599	0.9938 ± 0.0003

Table 21: Fitted hadronic event yields for the five 2013 continuum points and the 2009 3.65 GeV data with each of the hadronic event selection cuts.

J/ψ background that does not scale as $\frac{1}{s}$, as well as the $\tau\bar{\tau}$ background that is only kinematically possible for the three points above $\tau\bar{\tau}$ production threshold. The contribution from two-photon fusion is negligible after the Bhabha/two-photon fusion rejection. The details of the background subtractions for the various hadronic event selection cuts at our continuum energy points are shown in Tables 22-24. After subtracting these backgrounds, only events that scale as $\frac{1}{s}$ remain. The events which scale as $\frac{1}{s}$ are then fitted to extrapolate the efficiency ratio as a function of energy. Figures 42-45 show background-subtracted distributions after SHAD for the 2013 continuum data at $E_{cm} = 3542$ MeV and $E_{cm} = 3650$ MeV. There is no significant evidence of inconsistent beam backgrounds nor for inconsistency in tracking efficiency in these distributions. The differences in the N_{Trk} comparison are consistent with the change in E_{cm}.

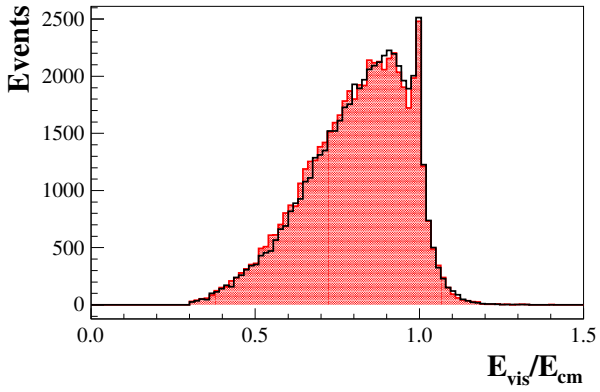

Figure 42: Background subtracted E_{Vis}/E_{cm} distributions for 2013 continuum data at $E_{cm} = 3542$ MeV (solid line) and $E_{cm} = 3650$ MeV (hatched histogram), scaled to each other by $\mathcal{L} \cdot \frac{1}{s}$.

Figures 46-48 show the extrapolation of efficiency ratios under SHAD, LHAD and THAD determined from the 2013 continuum data sets. More severe hadronic event selection cuts cause more energy dependence in the efficiency and thus a larger slope in the extrapolation. For the first round of $\psi(3770)$ data we use a linear fit to the five continuum data points taken in 2013 to obtain the slope of the extrapolation and then scale it to the 3.65 GeV continuum data taken in 2009 to calculate $\epsilon(3770round1)/\epsilon(3650)$. Here we assume the data taking conditions are similar for the first round of $\psi(3770)$ data and the 2009 3.65 GeV continuum

	σ (pb)	Efficiency	Yield ($\times 10^3$)
3.600 GeV			
Fit to data	–	–	41.99 ± 0.20
$\gamma J/\psi$	1.83115	0.4424 ± 0.0005	2.9815 ± 0.0033
$q\bar{q}$ in data	–	–	39.01 ± 0.20
3.542 GeV			
Fit to data	–	–	50.11 ± 0.21
$\gamma J/\psi$	1.63178	0.4424 ± 0.0005	3.2342 ± 0.0036
$q\bar{q}$ in data	–	–	46.87 ± 0.21
3.600 GeV			
Fit to data	–	–	4.301 ± 0.063
$\tau\bar{\tau}$	1.26249	0.1231 ± 0.0003	0.0614 ± 0.0002
$\gamma J/\psi$	1.41197	0.4420 ± 0.0005	0.2465 ± 0.0003
$q\bar{q}$ in data	–	–	3.994 ± 0.063
3.650 GeV			
Fit to data	–	–	58.56 ± 0.24
$\tau\bar{\tau}$	1.84358	0.1233 ± 0.0003	1.2321 ± 0.0033
$\gamma J/\psi$	1.26028	0.4406 ± 0.0005	3.0092 ± 0.0034
$q\bar{q}$ in data	–	–	54.32 ± 0.24
3.671 GeV			
Fit to data	–	–	49.81 ± 0.22
$\tau\bar{\tau}$	2.02614	0.1234 ± 0.0003	1.1678 ± 0.0031
$\gamma J/\psi$	1.20469	0.4405 ± 0.0005	2.4774 ± 0.0028
$q\bar{q}$ in data	–	–	46.16 ± 0.22
2009 3.650 GeV			
Fit to data	–	–	471.76 ± 0.69
$\tau\bar{\tau}$	1.84358	0.1224 ± 0.0003	10.008 ± 0.027
$\gamma J/\psi$	1.26028	0.4392 ± 0.0005	24.537 ± 0.028
$q\bar{q}$ in data	–	–	437.22 ± 0.69

Table 22: Background subtraction in continuum - SHAD.

	σ (pb)	Efficiency	Yield ($\times 10^3$)
3.600 GeV			
Fit to data	–	–	47.79 ± 0.22
$\gamma J/\psi$	1.83115	0.5459 ± 0.0005	3.6789 ± 0.0034
$q\bar{q}$ in data	–	–	44.12 ± 0.22
3.542 GeV			
Fit to data	–	–	56.62 ± 0.24
$\gamma J/\psi$	1.63178	0.5471 ± 0.0005	4.0000 ± 0.0036
$q\bar{q}$ in data	–	–	52.62 ± 0.24
3.600 GeV			
Fit to data	–	–	4.964 ± 0.071
$\tau\bar{\tau}$	1.26249	0.2834 ± 0.0005	0.1413 ± 0.0002
$\gamma J/\psi$	1.41197	0.5473 ± 0.0005	0.3052 ± 0.0003
$q\bar{q}$ in data	–	–	4.518 ± 0.071
3.650 GeV			
Fit to data	–	–	66.83 ± 0.26
$\tau\bar{\tau}$	1.84358	0.2806 ± 0.0004	2.8033 ± 0.0045
$\gamma J/\psi$	1.26028	0.5468 ± 0.0005	3.7351 ± 0.0034
$q\bar{q}$ in data	–	–	60.29 ± 0.26
3.671 GeV			
Fit to data	–	–	56.79 ± 0.24
$\tau\bar{\tau}$	2.02614	0.2794 ± 0.0004	2.6427 ± 0.0042
$\gamma J/\psi$	1.20469	0.5469 ± 0.0005	3.0758 ± 0.0028
$q\bar{q}$ in data	–	–	51.07 ± 0.24
2009 3.650 GeV			
Fit to data	–	–	542.24 ± 0.77
$\tau\bar{\tau}$	1.84358	0.2786 ± 0.0004	22.770 ± 0.037
$\gamma J/\psi$	1.26028	0.5447 ± 0.0005	30.432 ± 0.028
$q\bar{q}$ in data	–	–	489.04 ± 0.77

Table 23: Background subtraction in continuum - LHAD.

	σ (pb)	Efficiency	Yield ($\times 10^3$)
3.600 GeV			
Fit to data	–	–	32.90 ± 0.19
$\gamma J/\psi$	1.83115	0.3147 ± 0.0005	2.1210 ± 0.0031
$q\bar{q}$ in data	–	–	30.77 ± 0.19
3.542 GeV			
Fit to data	–	–	39.34 ± 0.20
$\gamma J/\psi$	1.63178	0.3150 ± 0.0005	2.3030 ± 0.0034
$q\bar{q}$ in data	–	–	37.04 ± 0.20
3.600 GeV			
Fit to data	–	–	3.428 ± 0.058
$\tau\bar{\tau}$	1.26249	0.0933 ± 0.0003	0.0465 ± 0.0001
$\gamma J/\psi$	1.41197	0.3144 ± 0.0005	0.1753 ± 0.0003
$q\bar{q}$ in data	–	–	3.206 ± 0.058
3.650 GeV			
Fit to data	–	–	46.37 ± 0.23
$\tau\bar{\tau}$	1.84358	0.0933 ± 0.0003	0.9325 ± 0.0029
$\gamma J/\psi$	1.26028	0.3135 ± 0.0005	2.1416 ± 0.0032
$q\bar{q}$ in data	–	–	43.30 ± 0.23
3.671 GeV			
Fit to data	–	–	39.43 ± 0.19
$\tau\bar{\tau}$	2.02614	0.0934 ± 0.0003	0.8832 ± 0.0028
$\gamma J/\psi$	1.20469	0.3135 ± 0.0005	1.7635 ± 0.0026
$q\bar{q}$ in data	–	–	36.79 ± 0.19
2009 3.650 GeV			
Fit to data	–	–	367.16 ± 0.60
$\tau\bar{\tau}$	1.84358	0.092 ± 0.0003	7.519 ± 0.024
$\gamma J/\psi$	1.26028	0.3099 ± 0.0005	17.316 ± 0.026
$q\bar{q}$ in data	–	–	342.32 ± 0.60

Table 24: Background subtraction in continuum - THAD.

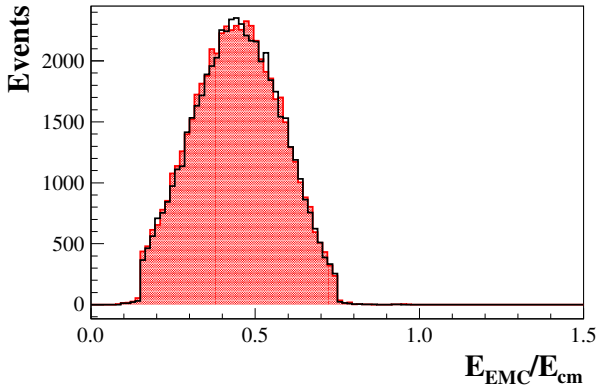

Figure 43: Background subtracted E_{EMC}/E_{cm} distributions for 2013 continuum data at $E_{cm} = 3542$ MeV (solid line) and $E_{cm} = 3650$ MeV (hatched histogram), scaled to each other by $\mathcal{L} \cdot \frac{1}{s}$.

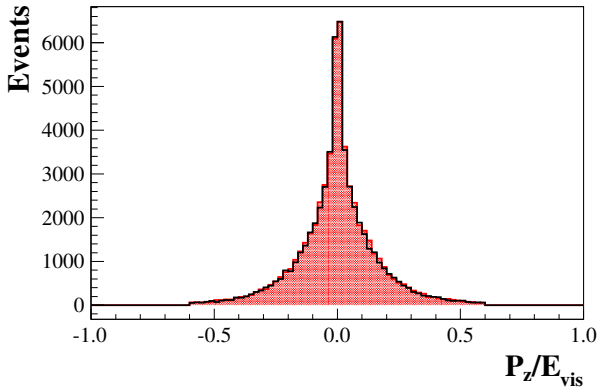

Figure 44: Background subtracted p_z/E_{cm} distributions for 2013 continuum data at $E_{cm} = 3542$ MeV (solid line) and $E_{cm} = 3650$ MeV (hatched histogram), scaled to each other by $\mathcal{L} \cdot \frac{1}{s}$.

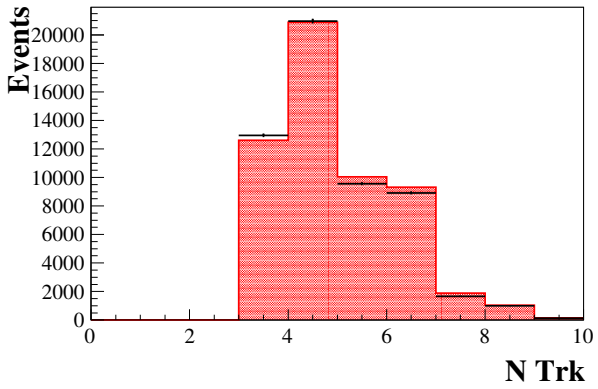

Figure 45: Background subtracted N_{Trk} distributions for 2013 continuum data at E_{cm} = 3542 MeV (solid line) and E_{cm} = 3650 MeV (hatched histogram), scaled to each other by $\mathcal{L} \cdot \frac{1}{s}$.

data. For the second round of $\psi(3770)$ data, we see a slightly increased hadronic selection efficiency across the board, as seen in Tables 28-29. To account for this, we use $q\bar{q}$ Monte Carlo samples to determine the efficiency difference between the two rounds of $\psi(3770)$ data taking and then correct the extrapolation with

$$\frac{\epsilon(3770round2)}{\epsilon(3650)} = \frac{\epsilon(3770round2)_{MC}}{\epsilon(3770round1)_{MC}} \cdot \frac{\epsilon(3770round1)}{\epsilon(3650)}. \tag{39}$$

The extrapolation results for the various hadronic event selection cuts are found in Table 25. The errors shown are statistical only, which are the quadratic sums of the statistical error of the slope in the linear fit to the 2013 continuum data points and the relative statistical errors of the hadron counting for the 3.65 GeV continuum data taken in 2009.

7.5 Hadronic Events at 3.773 GeV

To determine the number of hadronic events at the 3.773 GeV energy point, we fit the average V_z of the events that pass the hadronic event selection cuts, as we did for the continuum data described in Section 7.4.4. The fits are shown in Figure 49 and summarized in Table 26.

We use the data-driven extrapolation described in Section 7.4.4 to subtract the $\frac{1}{s}$ back-

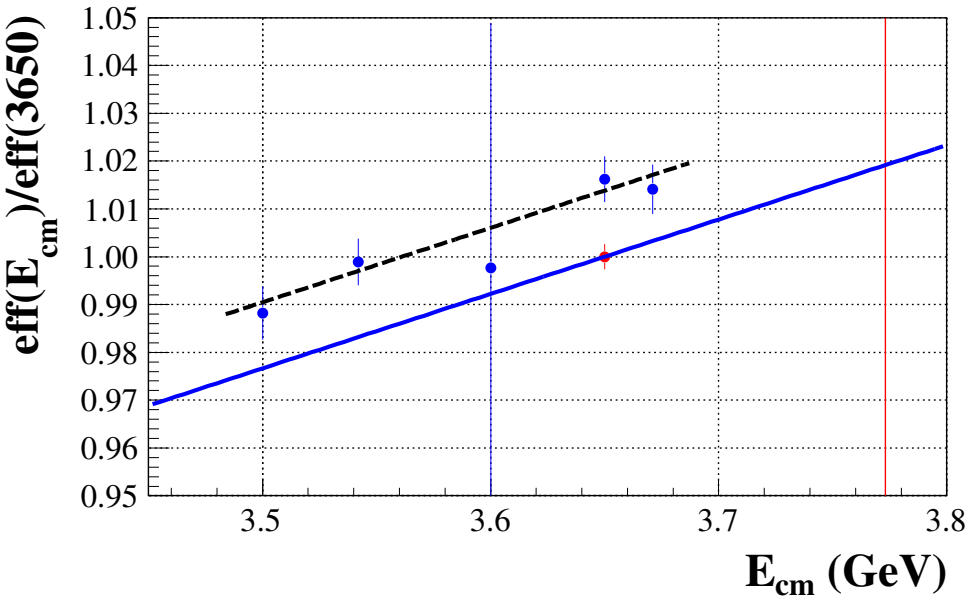

Figure 46: Extrapolation for SHAD. The points represent the continuum data taken in 2013, except the lower point at 3.65 GeV, which represents the continuum data taken in 2009. The dashed line is the linear fit to the 2013 data points, the solid line is the fit scaled to the 2009 continuum data.

Hadronic Event Selection	ϵ(**3770round1**)/ϵ(**3650**)	ϵ(**3770round2**)/ϵ(**3650**)
SHAD	1.0192 ± 0.0052	1.0290 ± 0.0052
LHAD	1.0042 ± 0.0052	1.0114 ± 0.0052
THAD	1.0275 ± 0.0059	1.0404 ± 0.0059

Table 25: Efficiency ratio extrapolation for the first and second rounds of $\psi(3770)$ data.

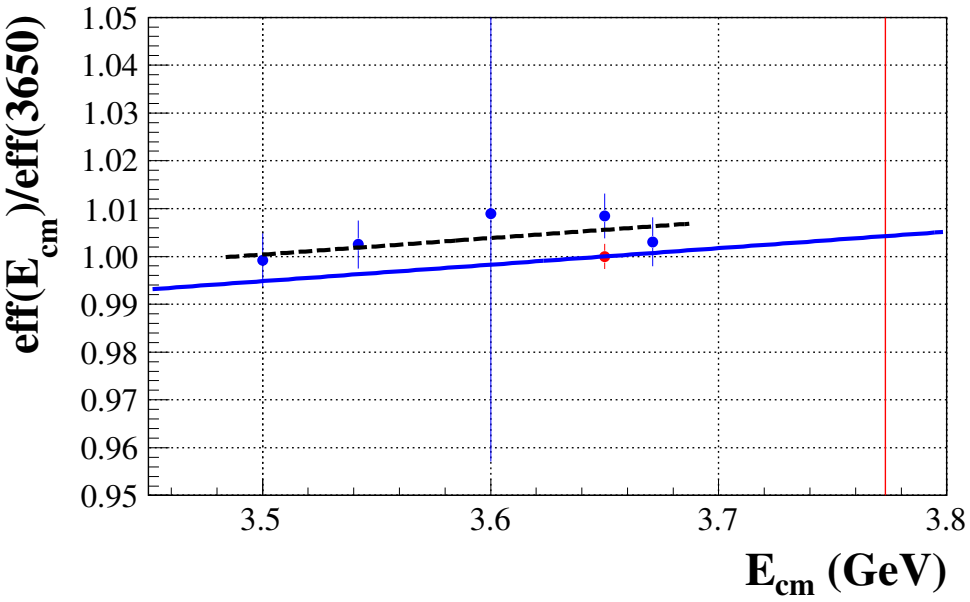

Figure 47: Extrapolation for LHAD. The points represent the continuum data taken in 2013, except the lower point at 3.65 GeV, which represents the continuum data taken in 2009. The dashed line is the linear fit to the 2013 data points, the solid line is the fit scaled to the 2009 continuum data.

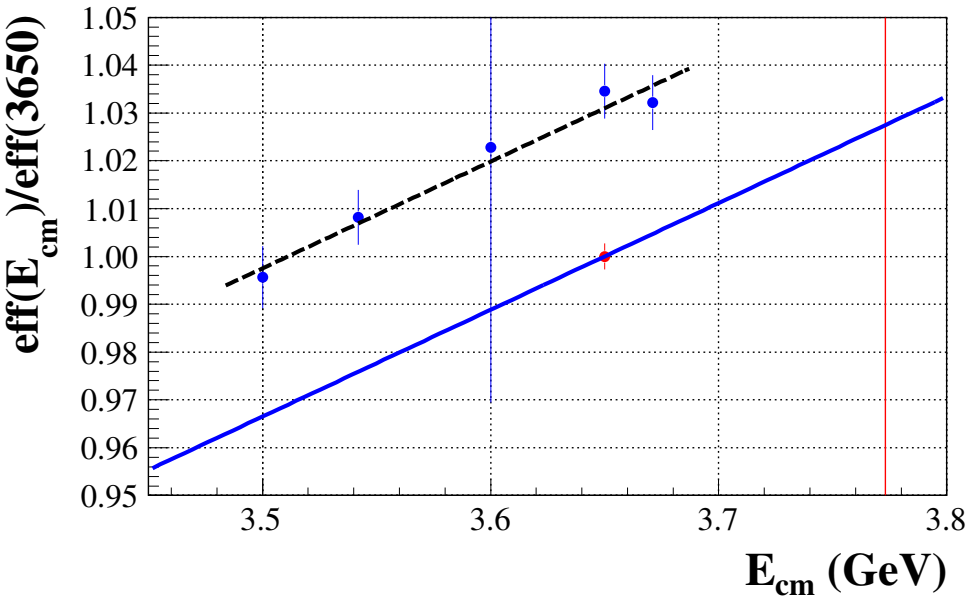

Figure 48: Extrapolation for THAD. The points represent the continuum data taken in 2013, except the lower point at 3.65 GeV, which represents the continuum data taken in 2009. The dashed line is the linear fit to the 2013 data points, the solid line is the fit scaled to the 2009 continuum data.

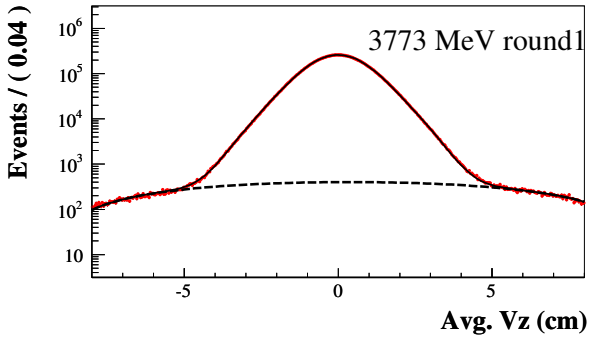

(a) First round

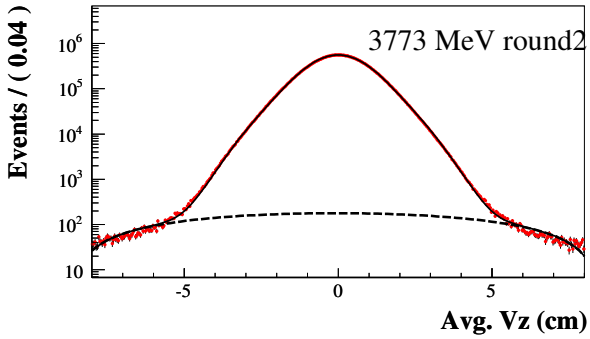

(b) Second round

Figure 49: Fits to the average V_z of events for the two rounds of $\psi(3770)$ data with SHAD cuts applied.

SHAD		
Data Set	**N(signal)** ($\times\mathbf{10^6}$)	**N(signal)/N(total)**
First round of $\psi(3770)$	15.5285 ± 0.0040	0.99214 ± 0.00006
Second round of $\psi(3770)$	33.5616 ± 0.0058	0.99850 ± 0.00002
LHAD		
Data Set	**N(signal)** ($\times\mathbf{10^6}$)	**N(signal)/N(total)**
First round of $\psi(3770)$	17.5943 ± 0.0042	0.98927 ± 0.00007
Second round of $\psi(3770)$	37.9827 ± 0.0062	0.99721 ± 0.00003
THAD		
Data Set	**N(signal)** ($\times\mathbf{10^6}$)	**N(signal)/N(total)**
First round of $\psi(3770)$	12.3330 ± 0.0034	0.99312 ± 0.00006
Second round of $\psi(3770)$	26.7942 ± 0.0052	0.99880 ± 0.00002

Table 26: Fitted hadron yields for the first and second rounds of $\psi(3770)$ data with the various hadronic event selection cuts.

grounds ($q\bar{q}$, e^+e^-, $\mu\bar{\mu}$, and $\gamma\gamma$) by scaling from the 2009 sample of 3.65 GeV continuum data to the $\psi(3770)$ data sets. We subtract the remaining backgrounds from $D\bar{D}$ and radiative returns to J/ψ and $\psi(3686)$ using the cross sections calculated in Sections 6 and 7.2, respectively, along with Monte Carlo derived efficiencies.

It is especially important to get the Monte Carlo hadronic event selection efficiency for $D\bar{D}$ events correct because this background cannot rely on cancellations between energy points as we do for the $q\bar{q}$ and other $\frac{1}{s}$ backgrounds and it is a much larger component than the $\tau\bar{\tau}$ and radiative return backgrounds. We improve our knowledge of the hadronic event selection efficiency in data by using D-tags in both data and MC. We use D-tags to measure the $D\bar{D}$ multiplicity spectrum, which is one of the largest factors in determing their hadronic event selection efficiency. If we know the multiplicity of a single generic D decay, we can predict the multiplicity of a $D\bar{D}$ event if we treat the D decays as uncorrelated and take a direct product of the single-D multiplicities. We choose the $D^0 \to K^-\pi^+$ and $D^+ \to K^-\pi^+\pi^+$ tag modes for this study due to their cleanliness and good statistics. After tagging a D, we infer the multiplicity of a generic $\bar{D}$ decay from the remaining tracks not used in the tag. We then convolve the two other-side D multiplicity distributions with a toy Monte Carlo technique to obtain a simulated event multiplicity for a complete $D\bar{D}$ event.

Hadronic event selection cuts SHAD, LHAD and THAD are simplified as requiring $N_{Trk} > 2$, $N_{Trk} > 1$ and $N_{Trk} > 3$, respectively, for this simulated multiplicity distribution in both data and MC. The efficiency ratios $\epsilon(data)/\epsilon(MC)$ under these three cuts are assigned as the corrections to the MC $D\bar{D}$ hadronic event selection efficiencies. The multiplicities for $D\bar{D}$ events which we use to correct the $D\bar{D}$ hadronic event selection efficiencies are shown in Figures 50-53. The resulting hadronic event selection efficiency corrections for $D\bar{D}$ events can be found in Table 27. The efficiency correction factors are relatively close to one and show good consistency between the two rounds of data taking. The $D^0\bar{D}^0$ events require more correction than the D^+D^- events because of the relatively large discrepancy between data and Monte Carlo in the zero other-side multiplicity bin, which is dominated by decays into all neutral final-state particles.

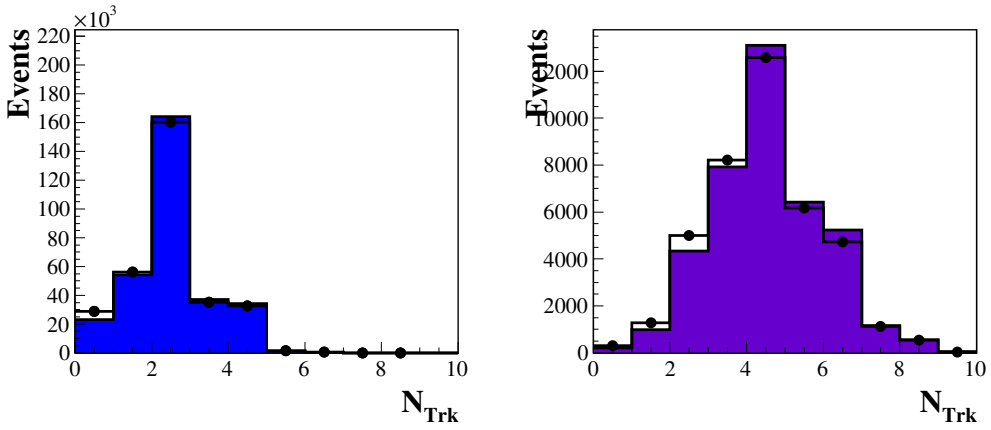

Figure 50: $D^0\bar{D}^0$ multiplicities used in the $D\bar{D}$ hadronic event selection efficiency correction for the first round of $\psi(3770)$ data. Left: data (points) and MC (histogram) of the other-side D multiplicity; right: data (points) and MC (histogram) of the convoluted $D\bar{D}$ event multiplicity.

Tables 28-29 show the results of the V_z fits, and the cross sections, efficiencies, and numbers of events used to subtract the backgrounds to obtain $N_{non-D\bar{D}}$, as shown in Equations 10 and 12. Figure 54 compares data to the extrapolated $q\bar{q}$ and other MC backgrounds by good track multiplicity after the various hadronic event selection cuts are applied for both rounds of $\psi(3770)$ data.

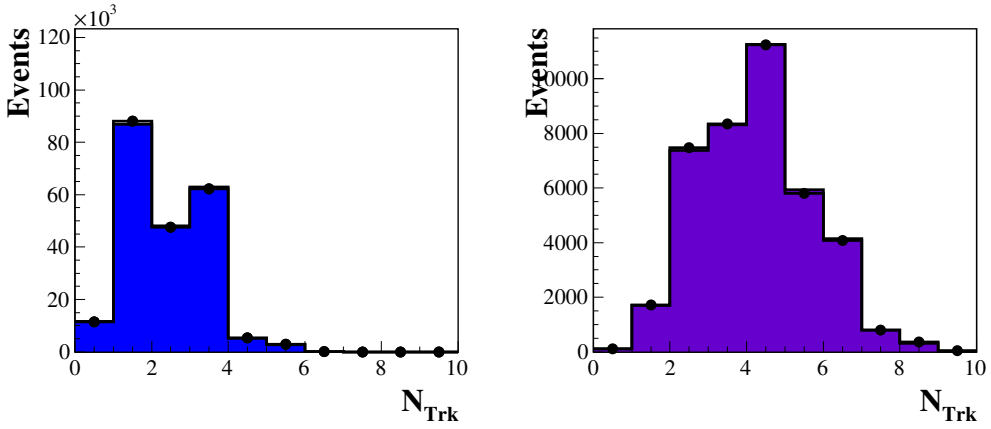

Figure 51: D^+D^- multiplicities used in the $D\bar{D}$ hadronic event selection efficiency correction for the first round of $\psi(3770)$ data. Left: data (points) and MC (histogram) of the other-side D multiplicity; right: data (points) and MC (histogram) of the convoluted $D\bar{D}$ event multiplicity.

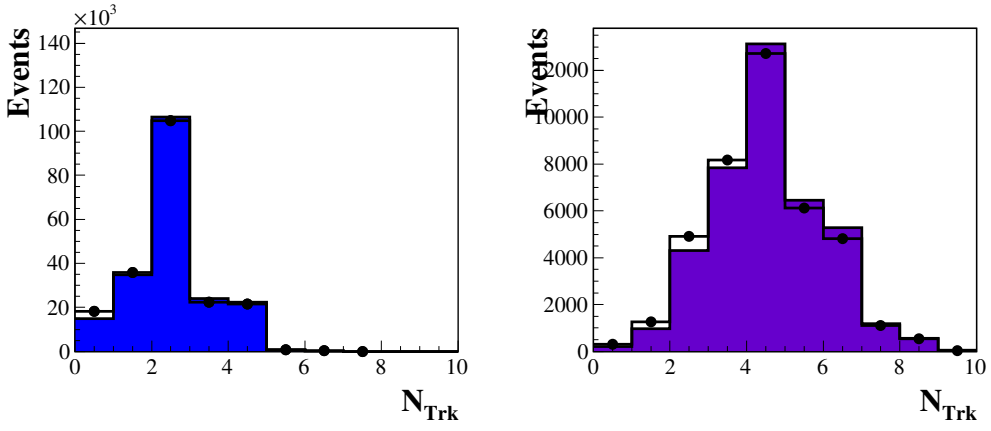

Figure 52: $D^0\bar{D}^0$ multiplicities used in the $D\bar{D}$ hadronic event selection efficiency correction for the second round of $\psi(3770)$ data. Left: data (points) and MC (histogram) of the other-side D multiplicity; right: data (points) and MC (histogram) of the convoluted $D\bar{D}$ event multiplicity.

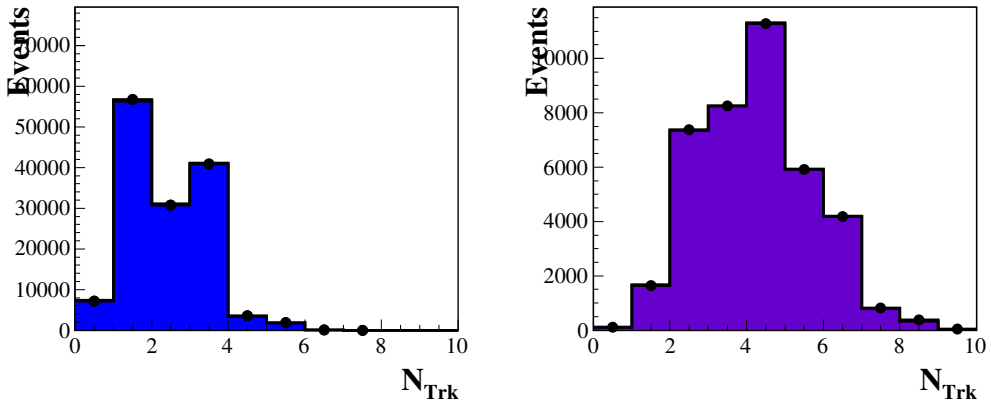

Figure 53: D^+D^- multiplicities used in the $D\bar{D}$ hadronic event selection efficiency correction for the second round of $\psi(3770)$ data. Left: data (points) and MC (histogram) of the other-side D multiplicity; right: data (points) and MC (histogram) of the convoluted $D\bar{D}$ event multiplicity.

First Round		
Hadronic Event Selection	$\epsilon(D^0\bar{D}^0)_{data}/\epsilon(D^0\bar{D}^0)_{MC}$	$\epsilon(D^+D^-)_{data}/\epsilon(D^+D^-)_{MC}$
SHAD	0.96953	0.99823
LHAD	0.98979	0.99980
THAD	0.94928	0.99753
Second Round		
Hadronic Event Selection	$\epsilon(D^0\bar{D}^0)_{data}/\epsilon(D^0\bar{D}^0)_{MC}$	$\epsilon(D^+D^-)_{data}/\epsilon(D^+D^-)_{MC}$
SHAD	0.97118	0.99985
LHAD	0.98993	1.00026
THAD	0.95074	0.99985

Table 27: $D\bar{D}$ efficiency correction for the two rounds of $\psi(3770)$ data.

SHAD			
	σ (pb)	**Efficiency**	**Yield ($\times 10^3$)**
Fit to data	–	–	15528.5 ± 4.0
$D\bar{D}$	6.485	0.66609 ± 0.00006	4003.95 ± 0.35
$q\bar{q}$ in data	–	–	8719 ± 14
$\tau\bar{\tau}$	2.652	0.12317 ± 0.00033	302.73 ± 0.81
$\gamma\psi(3686)$	3.009	0.61993 ± 0.00012	1729.05 ± 0.33
$\gamma J/\psi$	0.986	0.43821 ± 0.00050	400.34 ± 0.45
Excess hadronic events	–	–	374 ± 14
LHAD			
	σ (pb)	**Efficiency**	**Yield ($\times 10^3$)**
Fit to data	–	–	17594.3 ± 4.2
$D\bar{D}$	6.485	0.74087 ± 0.00005	4453.44 ± 0.32
$q\bar{q}$ in data	–	–	9610 ± 15
$\tau\bar{\tau}$	2.652	0.27482 ± 0.00045	675.5 ± 1.1
$\gamma\psi(3686)$	3.009	0.69049 ± 0.00011	1925.86 ± 0.31
$\gamma J/\psi$	0.986	0.54335 ± 0.00050	496.38 ± 0.46
Excess hadronic events	–	–	434 ± 16
THAD			
	σ (pb)	**Efficiency**	**Yield ($\times 10^3$)**
Fit to data	–	–	12333.0 ± 3.5
$D\bar{D}$	6.485	0.53200 ± 0.00006	3197.92 ± 0.37
$q\bar{q}$ in data	–	–	6882 ± 12
$\tau\bar{\tau}$	2.652	0.09267 ± 0.00029	227.76 ± 0.71
$\gamma\psi(3686)$	3.009	0.50122 ± 0.00012	1397.97 ± 0.34
$\gamma J/\psi$	0.986	0.31136 ± 0.00046	284.44 ± 0.42
Excess hadronic events	–	–	343 ± 13

Table 28: Excess hadronic events for the first round of $\psi(3770)$ data after subtracting off $D\bar{D}$ events and other backgrounds. Such events are attributed to non-$D\bar{D}$ decays of $\psi(3770)$. The excess is measured using the various hadronic event selection cuts.

SHAD			
	σ (pb)	**Efficiency**	**Yield ($\times 10^3$)**
Fit to data	–	–	33561.6 ± 5.8
$D\bar{D}$	6.485	0.67359 ± 0.00006	8644.40 ± 0.73
$q\bar{q}$ in data	–	–	18793 ± 30
$\tau\bar{\tau}$	2.652	0.12809 ± 0.00033	672.1 ± 1.8
$\gamma\psi(3686)$	3.009	0.62223 ± 0.00048	3705.0 ± 2.9
$\gamma J/\psi$	0.986	0.45389 ± 0.00050	885.22 ± 0.97
Excess hadronic events	–	–	862 ± 30
LHAD			
	σ (pb)	**Efficiency**	**Yield ($\times 10^3$)**
Fit to data	–	–	37982.7 ± 6.2
$D\bar{D}$	6.485	0.74716 ± 0.00005	9588.54 ± 0.68
$q\bar{q}$ in data	–	–	20661 ± 32
$\tau\bar{\tau}$	2.652	0.28124 ± 0.00045	1475.7 ± 2.4
$\gamma\psi(3686)$	3.009	0.69414 ± 0.00046	4133.1 ± 2.7
$\gamma J/\psi$	0.986	0.55693 ± 0.00050	1086.19 ± 0.97
Excess hadronic events	–	–	1038 ± 33
THAD			
	σ (pb)	**Efficiency**	**Yield ($\times 10^3$)**
Fit to data	–	–	26794.2 ± 5.2
$D\bar{D}$	6.485	0.53950 ± 0.00006	6923.56 ± 0.78
$q\bar{q}$ in data	–	–	14877 ± 26
$\tau\bar{\tau}$	2.652	0.09953 ± 0.00030	522.2 ± 1.6
$\gamma\psi(3686)$	3.009	0.50157 ± 0.00050	2986.5 ± 3.0
$\gamma J/\psi$	0.986	0.33155 ± 0.00047	646.62 ± 0.92
Excess hadronic events	–	–	838 ± 27

Table 29: Excess hadronic events for the second round of $\psi(3770)$ data after subtracting off $D\bar{D}$ events and other backgrounds. Such events are attributed to non-$D\bar{D}$ decays of $\psi(3770)$. The excess is measured using the various hadronic event selection cuts.

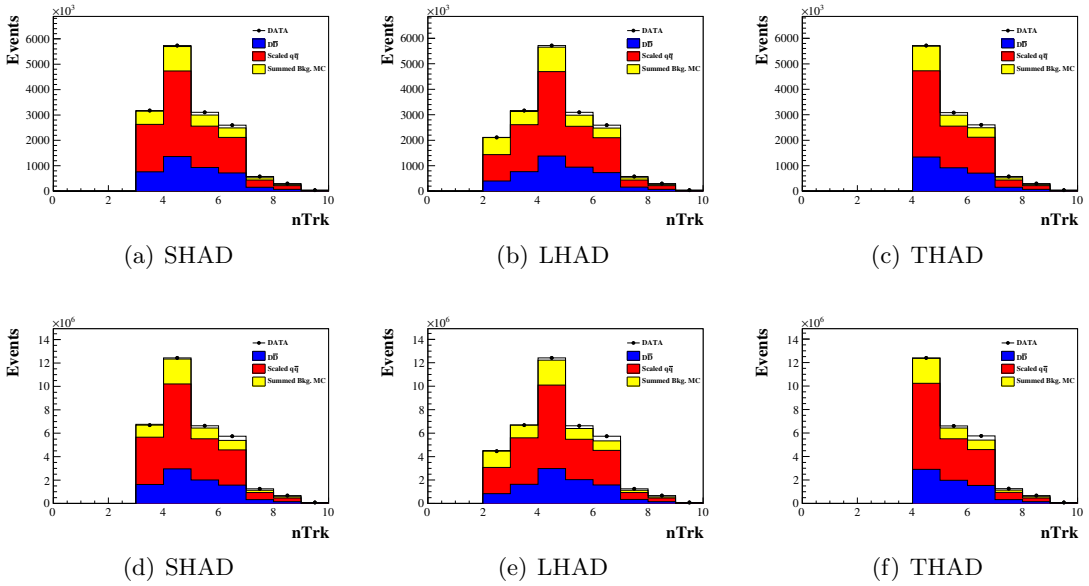

(a) SHAD (b) LHAD (c) THAD

(d) SHAD (e) LHAD (f) THAD

Figure 54: N_{Trk} for the listed hadronic event selection cuts. The first round of $\psi(3770)$ data is on the top row, the second round is on the bottom row.

7.6 Hadron Counting Systematics

We evaluate several sources of systematic error associated with the hadronic event counting that impact our measurement of $\mathcal{B}(\psi(3770) \to non - D\bar{D})$. The dominant systematic error is from hadronic event selection. We estimate this systematic error with the alternative hadronic event selection cuts (LHAD and THAD) described in Section 7.1. The good track multiplicity criteria of the hadronic event selection cuts is the largest difference between the sets of cuts. The maximum difference between the standard set of cuts and the alternate cuts is taken as the systematic error due to hadronic event selection. This systematic error and the others described below are summarized in Table 30.

The determination of the cross sections used to subtract the backgrounds that are not accounted for by extrapolation ($D\bar{D}$ and radiative returns to $\psi(3686)$ and J/ψ) also give rise to systematic errors. We vary the $D\bar{D}$ cross section by the total error (statistical and systematic) on this measurement, as described in Section 6.7 and take the difference from the central value as the systematic error due to the $D\bar{D}$ cross section.

The total error on the cross section at 3.773 GeV of radiative return to $\psi(3686), \psi(3686) \to \pi^+\pi^- J/\psi$ in [22] is 26 pb and the combined total error of $\psi(3686) \to \pi^+\pi^- J/\psi$ is 0.30% (averaged from PDG [3] and the recent BESIII measurement [64]). Propagating these two

errors, the total error of the cross section of radiative return to $\psi(3686)$ at 3.773 GeV is 2.66%. We vary the input cross section of radiative return to $\psi(3686)$ within this error and take the resulting change as the systematic error.

We take the relative difference in $\sigma_{\gamma\psi(3686)}$ between the theory-based and data-driven methods outlined in Section 7.2 as the relative systematic error of $\sigma_{\gamma J/\psi,data}$:

$$\Delta\sigma_{\gamma J/\psi} = \frac{\sigma_{\gamma\psi(3686),data} - \sigma_{\gamma\psi(3686),theory}}{\sigma_{\gamma\psi(3686),theory}} \cdot \sigma_{\gamma J/\psi,theory}. \quad (40)$$

We then vary the cross section of radiative return to J/ψ by $\Delta\sigma_{\gamma J/\psi}$ to measure the effect on our measurement of $N_{non-D\bar{D}}$.

The subtraction of backgrounds determined from the extrapolation from continuum give rise to systematic errors due to the statistics of the continuum data and from the shape used to extrapolate the continuum data points. We vary the $\epsilon(3773)/\epsilon(3650)$ value within the statistical error of the extrapolation shown in Table 25. The statistical error of the efficiency extrapolation is the quadratic sum of the statistical error of the slope in the linear fit to the five continuum data points taken in 2013 and the statistical error of the hadron counting for the 3.65 GeV continuum taken in 2009. We take the difference of $\epsilon(3773)/\epsilon(3650)$ between the linear and quadratic fits to the five MC continuum points (0.3%, as shown in Section 7.4.2) as the systematic error of the extrapolation.

To evaluate the systematic error due to the integrated luminosity measurement, we vary the integrated luminosity within the systematic error of the integrated luminosity in Ref. [59], which is a 1% relative error. We recalculate $\sigma_{non-D\bar{D}}$ and $\mathcal{B}(\psi(3770) \to non-D\bar{D})$ with the integrated luminosity varied by 1% and then take this difference as the systematic error due to the integrated luminosity measurement. The integrated luminosity systematic error has already been included in the total error on the $D\bar{D}$ cross section and consequently in the systematic error for non-$D\bar{D}$ due to the $D\bar{D}$ cross section. Therefore we do not vary the integrated luminosity when calculating the $D\bar{D}$ contribution to the integrated luminosity systematic error.

Source of systematic error	**Systematic error on** $\sigma_{\psi(\mathbf{3770})\to\mathbf{non-D\bar{D}}}$ **(pb)**	**Systematic error on** $\mathcal{B}(\psi(\mathbf{3770}) \to \mathbf{non - D\bar{D}})$
Hadronic event selection	0.126	0.016
$\gamma\psi(3686)$	0.081	0.010
$\gamma J/\psi$	0.039	0.005
$D\bar{D}$	0.090	0.012
Extrapolation stat.	0.078	0.010
Extrapolation syst.	0.046	0.006
Integrated Luminosity	0.049	0.006
Total	0.206	0.026

Table 30: Summary of the systematic errors for $\psi(3770) \to non - D\bar{D}$.

8 $\mathcal{B}(\psi(3770) \to non - D\bar{D})$ Results and Systematics

We review here the method to measure $\mathcal{B}(\psi(3770) \to non - D\bar{D})$. For a more detailed discussion of this calculation, see Section 4. To calculate this branching fraction, we divide the $\psi(3770) \to non - D\bar{D}$ cross section by the total $\psi(3770)$ cross section,

$$\mathcal{B}(\psi(3770) \to non - D\bar{D}) = \frac{\sigma_{non-D\bar{D}}}{\sigma_{\psi(3770)}}, \tag{41}$$

where the cross sections are determined from

$$\sigma_{non-D\bar{D}} = \frac{N_{non-D\bar{D}}}{\mathcal{L}^{3.773}\epsilon_{non-D\bar{D}}} \text{ and } \sigma_{\psi(3770)} = \frac{N_{\psi(3770)}}{\mathcal{L}^{3.773}\epsilon_{\psi(3770)}}. \tag{42}$$

The integrated luminosity is measured in Section 7.4.3 and summarized in Table 20. The efficiency of $\psi(3770)$ events passing hadronic selection cuts is a cross-section-weighted average of the $D\bar{D}$ and non-$D\bar{D}$ hadronic event selection efficiencies. The $D\bar{D}$ efficiency is obtained from Monte Carlo and corrected with the ratios shown in Table 27. The non-$D\bar{D}$ events are assumed to be similar to $\psi(3686)$ events and so their hadronic event selection efficiency is taken from radiative return to $\psi(3686)$ Monte Carlo at the 3.773 GeV energy point.

We measure the number of $\psi(3770)$ events passing hadronic event selection cuts as

$$\begin{aligned} N_{\psi(3770)} = N_{had}^{3.773} \\ -(N_{q\bar{q}}^{3.773} + N_{e\bar{e}}^{3.773} + N_{\mu\bar{\mu}}^{3.773} + N_{\gamma\gamma}^{3.773} + N_{2\gamma-fus}^{3.773}) \\ -N_{\tau\bar{\tau}}^{3.773} - N_{\gamma\psi(3686)}^{3.773} - N_{\gamma J/\psi}^{3.773}. \end{aligned} \tag{43}$$

The number of hadronic events at 3.773 GeV is measured by fitting the average vertex of events that pass hadronic event selection cuts, shown in Table 26. The $\tau\bar{\tau}$, $\gamma\psi(3686)$, and $\gamma J/\psi$ backgrounds are estimated from Monte Carlo, while the other backgrounds are extrapolated from the 2009 continuum data using

$$\begin{aligned} (N_{q\bar{q}}^{3.773} + N_{e\bar{e}}^{3.773} + N_{\mu\bar{\mu}}^{3.773} + N_{\gamma\gamma}^{3.773} + N_{2\gamma-fus}^{3.773}) = \\ (N_{had}^{3.65} - N_{\tau\bar{\tau}}^{3.65} - N_{\psi(3686)}^{3.65} - N_{\gamma J/\psi}^{3.65}) \frac{\epsilon(3.773)}{\epsilon(3.65)} \frac{\mathcal{L}^{3.773}}{\mathcal{L}^{3.65}} \frac{3.65^2}{3.773^2}. \end{aligned} \tag{44}$$

The number of hadronic events at 3.65 GeV is measured by fitting the average vertex of events that pass hadronic event selection cuts, shown in Table 21. The number of background events are estimated from Monte Carlo and scaled by the ratio of hadronic event selection efficiencies shown in Table 25 and described in Section 7.4, the integrated lumionosities measured in Section 7.4.3 and shown in Table 20, and the center-of-mass energies.

The number of non-$D\bar{D}$ events passing hadronic event selection cuts is given by

$$N_{non-D\bar{D}} = N_{\psi(3770)} - N_{D\bar{D}}\epsilon_{D\bar{D}}, \tag{45}$$

where $N_{D\bar{D}}$ is calculated in Section 6.7. The background subtraction in continuum data is shown in Tables 22-24 and the background subtraction at 3.773 GeV is shown in Tables 28-29.

We measure the cross section and branching ratio of $\psi(3770) \to non - D\bar{D}$ with the SHAD cuts and the combination of the first and second rounds of $\psi(3770)$ data as our central value. The individual systematic uncertainties shown in Table 30 are combined in quadrature to obtain the total systematic error for the non-$D\bar{D}$ cross section and branching fraction. We measure the cross section of $\psi(3770) \to non - D\bar{D}$ to be $(0.684 \pm 0.025 \pm 0.206)$ pb and its associated branching fraction to be $(9.54 \pm 0.31 \pm 2.64)\%$, where the first errors are statistical and the second errors are systematic.

9 Conclusion

We measure $\sigma_{D\bar{D}}$ and $\sigma_{non-D\bar{D}}$ in order to better understand the nature of the $\psi(3770)$ resonance. Our measurements of $\sigma_{D^0\bar{D}^0} = (3.641 \pm 0.010(stat) \pm 0.047(sys))$ nb and $\sigma_{D^+D^-} = (2.844 \pm 0.011(stat) \pm 0.036(sys))$ nb are in good agreement with the previous measurements of CLEO-c: $\sigma_{D^0\bar{D}^0} = (3.607 \pm 0.017(stat) \pm 0.056(sys))$ nb and $\sigma_{D^+D^-} = (2.882 \pm 0.018(stat) \pm 0.042(sys))$ nb [66].

The interpretation of the non-$D\bar{D}$ branching fraction, $\mathcal{B}(\psi(3770) \to non - D\bar{D}) = (9.54 \pm 0.31 \pm 2.64)\%$, is more difficult. Observed exclusive branching fractions of $\psi(3770) \to non - D\bar{D}$ sum to only 1.4%. The measured exclusive branching fractions include many of the decay modes expected to contribute most significantly to non-$D\bar{D}$ final states, including decays to final states with a J/ψ and E1 transitions to $\gamma\chi_{cJ}$. Decays of $\psi(3770)$ to light hadrons remain as possible final states which may contribute to an excess production of non-$D\bar{D}$ which has not been ruled out by experimental measurements. Only $\mathcal{B}(\psi(3770) \to \phi\eta) = 0.031 \pm 0.006 \pm 0.003 \pm 0.001\%$ [14] has been observed, while decays to light hadrons are predicted to account for $1.72^{+1.24}_{-0.69}\%$ of $\psi(3770)$ decays [23].

Quantum mechanical interference effects also make it difficult to unambiguously interpret measurements of the non-$D\bar{D}$ cross section. We employ a similar method as CLEO-c when measuring the non-$D\bar{D}$ cross section, as we both subtract the $D\bar{D}$ cross section from the total $\psi(3770)$ cross section. Our total $D\bar{D}$ cross sections are nearly identical, and so the point of disagreement comes from the total $\psi(3770)$ cross section, and in particular the treatment of interference between resonant and continuum production of hadronic final states via a virtual photon used when subtracting the background at the $\psi(3770)$ peak differs. CLEO-c assumes the interference is the same as that of $\mu\mu$, while we do not account for interference because we believe that interference would add incoherently, or just differently, due to the many possible gluonic Feynmann diagrams that could contribute to hadronic final states. This interference effect is the main difference between our measurement and CLEO-c's measurement of $\mathcal{B}(\psi(3770) \to non - D\bar{D}) = (-3.3 \pm 1.4^{+6.6}_{-4.8})\%$. Using the data presented in Ref. [20], it is possible to calculate the non-$D\bar{D}$ branching fraction they would have measured without their assumption that there is interference between hadronic final states from non-resonant annihilation ($e^+e^- \to \gamma^* \to q\bar{q} \to$hadrons) and from resonance decays via a virtual photon ($e^+e^- \to \gamma^* \to$resonance$\to \gamma^* \to q\bar{q} \to$hadrons). With an assumption of no such interference, they would measure $\mathcal{B}(\psi(3770) \to non - D\bar{D}) \approx 7\%$, which is consistent with our measurement that assumes no interference. Previously, BESII measured $\mathcal{B}(\psi(3770) \to non - D\bar{D})$ to be 13.4–16.4% [15, 16, 17, 18] with the assumption of

no interference, and we are also consistent with these results, which all have errors of $\gtrsim 5\%$, absolute. The disagreement between inclusive measurements is almost entirely attributable to assumptions on how to treat interference.

Reconciliation of experimental results for non-$D\bar{D}$ decays of the $\psi(3770)$ resonance remains difficult. A more nuanced theoretical understanding of the interference effects between continuum and resonant production of hadronic final states via virtual photon would aid in experimentally measuring the total cross section of the $\psi(3770)$ resonance and subsequently the non-$D\bar{D}$ cross section. Further exclusive branching fraction measurements of non-$D\bar{D}$ final states may reveal other modes that contribute significantly to the decays of the $\psi(3770)$ resonance. In particular, light hadron final states are theoretically expected to be one of the larger sources of non-$D\bar{D}$ decays, but only $\eta\phi$ has been observed.

References

[1] Q. Ho-Kim, X.Y. Pham. Elementary Particles and Their Interactions. Springer-Verlag. 1998.

[2] A. Das, T. Ferbel. Introduction to Nuclear and Particle Physics. 2003.

[3] J. Beringer *et al.* [Particle Data Group Collaboration], Phys. Rev. D **86**, 010001 (2012).

[4] T. Barnes, S. Godfrey and E. S. Swanson, Phys. Rev. D **72**, 054026 (2005) [hep-ph/0505002].

[5] T. Barnes, Int. J. Mod. Phys. A **21**, 5583 (2006) [hep-ph/0608103].

[6] J. L. Rosner, Phys. Rev. D **64**, 094002 (2001) [hep-ph/0105327].

[7] J. L. Rosner, Annals Phys. **319**, 1 (2005) [hep-ph/0411003].

[8] S. Okubo, Phys. Lett. **5**, 165 (1963).

[9] G. Zweig, Developments in the Quark Theory of Hadrons, Volume 1. Edited by D. Lichtenberg and S. Rosen. pp. 22-101

[10] J. Iizuka, K. Okada and O. Shito, Prog. Theor. Phys. **35**, 1061 (1966).

[11] Y. -B. Ding, D. -H. Qin and K. -T. Chao, Phys. Rev. D **44**, 3562 (1991).

[12] E. J. Eichten, K. Lane and C. Quigg, Phys. Rev. D **69**, 094019 (2004) [hep-ph/0401210].

[13] Y. -P. Kuang and T. -M. Yan, Phys. Rev. D **41**, 155 (1990).

[14] Z. -G. He, Y. Fan and K. -T. Chao, Phys. Rev. Lett. **101**, 112001 (2008) [arXiv:0802.1849 [hep-ph]].

[15] M. Ablikim *et al.* [BES Collaboration], Phys. Lett. B **659**, 74 (2008).

[16] M. Ablikim, J. Z. Bai, Y. Ban, X. Cai, H. F. Chen, H. S. Chen, H. X. Chen and J. C. Chen *et al.*, Phys. Rev. D **76**, 122002 (2007).

[17] M. Ablikim *et al.* [BES Collaboration], Phys. Lett. B **641**, 145 (2006) [hep-ex/0605105].

[18] M. Ablikim *et al.* [BES Collaboration], Phys. Rev. Lett. **97**, 121801 (2006) [hep-ex/0605107].

[19] D. Besson *et al.* [CLEO Collaboration], 3773-MeV," Phys. Rev. Lett. **96**, 092002 (2006) [Erratum-ibid. **104**, 159901 (2010)] [hep-ex/0512038].

[20] D. Besson *et al.* [CLEO Collaboration], Phys. Rev. Lett. **104**, 159901 (2010) [arXiv:1004.1358 [hep-ex]].

[21] J. Z. Bai *et al.* [BES Collaboration], Phys. Lett. B **605**, 63 (2005) [hep-ex/0307028].

[22] N. E. Adam *et al.* [CLEO Collaboration], Phys. Rev. Lett. **96**, 082004 (2006) [hep-ex/0508023].

[23] G. S. Adams *et al.* [CLEO Collaboration], Phys. Rev. D **73**, 012002 (2006) [hep-ex/0509011].

[24] T. E. Coan *et al.* [CLEO Collaboration], Phys. Rev. Lett. **96**, 182002 (2006) [hep-ex/0509030].

[25] R. A. Briere *et al.* [CLEO Collaboration], Phys. Rev. D **74**, 031106 (2006) [hep-ex/0605070].

[26] G. S. Huang *et al.* [CLEO Collaboration], Phys. Rev. Lett. **96**, 032003 (2006) [hep-ex/0509046].

[27] M. Ablikim *et al.* [BESIII Collaboration], Phys. Rev. D **87**, 112011 (2013) [arXiv:1305.1782 [hep-ex]].

[28] M. Ablikim, J. Z. Bai, Y. Ban, J. G. Bian, X. Cai, H. F. Chen, H. S. Chen and H. X. Chen *et al.*, Phys. Rev. D **72**, 072007 (2005) [hep-ex/0507092].

[29] D. Cronin-Hennessy *et al.* [CLEO Collaboration], Phys. Rev. D **74**, 012005 (2006) [Erratum-ibid. D **75**, 119903 (2007)] [hep-ex/0603026].

[30] M. Ablikim *et al.* [BES Collaboration], Eur. Phys. J. C **66**, 11 (2010).

[31] M. B. Voloshin, Phys. Rev. D **71**, 114003 (2005) [hep-ph/0504197].

[32] H. J. Lipkin, Phys. Lett. B **179**, 278 (1986).

[33] Y. -J. Zhang, G. Li and Q. Zhao, Phys. Rev. Lett. **102**, 172001 (2009) [arXiv:0902.1300 [hep-ph]].

[34] X. Liu, B. Zhang and X. -Q. Li, Phys. Lett. B **675**, 441 (2009) [arXiv:0902.0480 [hep-ph]].

[35] G. Li, X. -h. Liu, Q. Wang and Q. Zhao, Phys. Rev. D **88**, no. 1, 014010 (2013) [arXiv:1302.1745 [hep-ph]].

[36] M. Ablikim *et al.* [BESIII Collaboration], Nucl. Instrum. Meth. A **614**, 345 (2010) [arXiv:0911.4960 [physics.ins-det]].

[37] H. Bethe and J. Ashkin, Exp. Nucl. PhysĖ. Segre, J. Wiley. (eds) 253 (1953).

[38] W. Li, *et al.*, Proc. Int. Conf. Comput. High Energy and Nucl. Phys. 225 (2006).

[39] http://linux.web.cern.ch/linux/scientific5/.

[40] G. Barrand, I. Belyaev, P. Binko, M. Cattaneo, R. Chytracek, G. Corti, M. Frank and G. Gracia *et al.*, Comput. Phys. Commun. **140**, 45 (2001).

[41] C. Arnault, "CMT: A software configuration management tool," (2000).

[42] http://www.cern.ch/gdml.

[43] http://root.cern.ch/drupal.

[44] S. Agostinelli, *et al.*, Nucl. Instr. and Meth. **506**, (3), 250 (2003); J. Allison, *et al.*, IEEE Trans. Nucl. Sci. NS **53** (1), 270 (2006); http://www.geant4.org/geant4.

[45] http://www.mysql.com/about/.

[46] Deng Zi-Yan, *et al.*, High Energy Phys. Nucl. Phys. **30** (5), 371 (2006) (in Chinese).

[47] S. Jadach , B. F. L. Ward and Z. Was, Comp. Phys. Commun. **130**, 260 (2000); S. Jadach, B. F. L. Ward and Z. Was, Phys. Rev. D **63**, 113009 (2001).

[48] S. Jadach, Z. Was, R. Decker and J. H. Kuhn, Comput. Phys. Commun. **76**, 361 (1993).

[49] http://home.thep.lu.se/torbjorn/Pythia.html.

[50] R. G. Ping, Chinese Physics C **32**, 8 (2008).

[51] D.J. Lange, Nucl. Instrum. Meth. A **462**, 152 (2001).

[52] E. Barberio, B. van Eijk and Z. Was, Comput. Phys. Commun. **66**, 115 (1991).

[53] J. C. Chen, G. S. Huang, X. R. Qi, D. H. Zhang and Y. S. Zhu, Phys. Rev. D **62**, 034003 (2000).

[54] C.M. Carloni Calame, G. Montagna, O. Nicrosini, F. Piccinini, Nucl. Phys. Proc. Suppl. **131** 48-55 (2004).

[55] D. M. Asner, T. Barnes, J. M. Bian, I. I. Bigi, N. Brambilla, I. R. Boyko, V. Bytev and K. T. Chao *et al.*, Int. J. Mod. Phys. A **24**, S1 (2009) [arXiv:0809.1869 [hep-ex]].

[56] R. M. Baltrusaitis *et al.* [MARK-III Collaboration], Phys. Rev. Lett. **56**, 2140 (1986).

[57] J. Adler *et al.* [MARK-III Collaboration], Phys. Rev. Lett. **60**, 89 (1988).

[58] Chunlei Liu (for the DTag Task Force), "DTag Event Selection at BESIII," BESIII-doc-105-v4.

[59] M. Ablikim *et al.* [BESIII Collaboration], Chinese Physics C **37**, 12 (2013):12300.

[60] H. Albrecht *et al.* [ARGUS Collaboration], Phys. Lett. B **241**, 278 (1990).

[61] Chunlei Liu, "D^0 Semileptonic Analysis at BESIII," BESIII-doc-123-v10 (2013).

[62] D. M. Asner *et al.* [CLEO Collaboration], Phys. Rev. D **78**, 012001 (2008) [arXiv:0802.2268 [hep-ex]].

[63] Dan Cronin-Hennessy, "$\psi(3770) \to D\bar{D}$ Lineshape," presented at Charm Group Meeting (August 27, 2013).

[64] M. Ablikim *et al.* [BESIII Collaboration], Phys. Rev. D **88**, 032007 (2013) [arXiv:1307.1189].

[65] N. Brambilla *et al.* [Quarkonium Working Group Collaboration], Chapter 2 Page 49, hep-ph/0412158.

[66] G. Bonvicini *et al.* [CLEO Collaboration], Phys. Rev. D **89**, 072002 (2014) [arXiv:1312.6775 [hep-ex]].

A Double-tag Fits

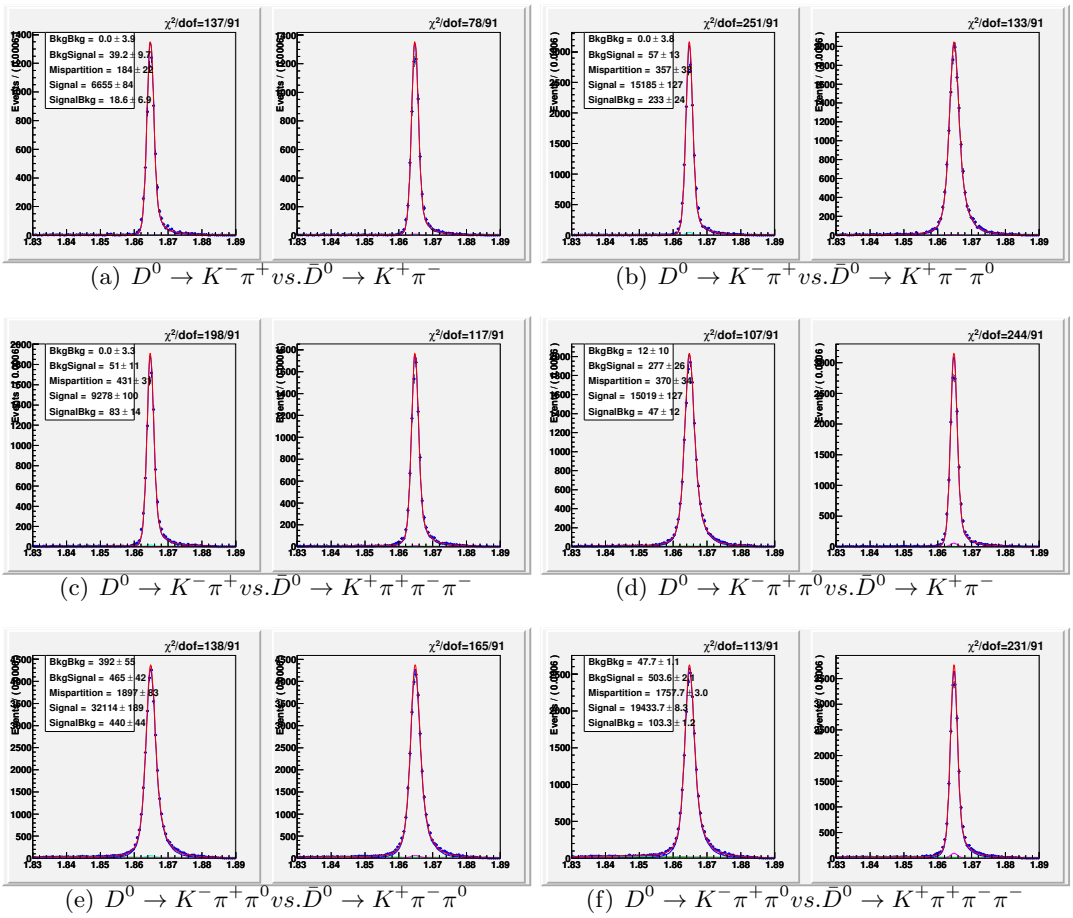

(a) $D^0 \to K^-\pi^+ vs. \bar{D}^0 \to K^+\pi^-$ (b) $D^0 \to K^-\pi^+ vs. \bar{D}^0 \to K^+\pi^-\pi^0$

(c) $D^0 \to K^-\pi^+ vs. \bar{D}^0 \to K^+\pi^+\pi^-\pi^-$ (d) $D^0 \to K^-\pi^+\pi^0 vs. \bar{D}^0 \to K^+\pi^-$

(e) $D^0 \to K^-\pi^+\pi^0 vs. \bar{D}^0 \to K^+\pi^-\pi^0$ (f) $D^0 \to K^-\pi^+\pi^0 vs. \bar{D}^0 \to K^+\pi^+\pi^-\pi^-$

Figure 55: Two-dimensional m_{BC} fits from data used to determine double-tag yields, as detailed in Section 6.5.

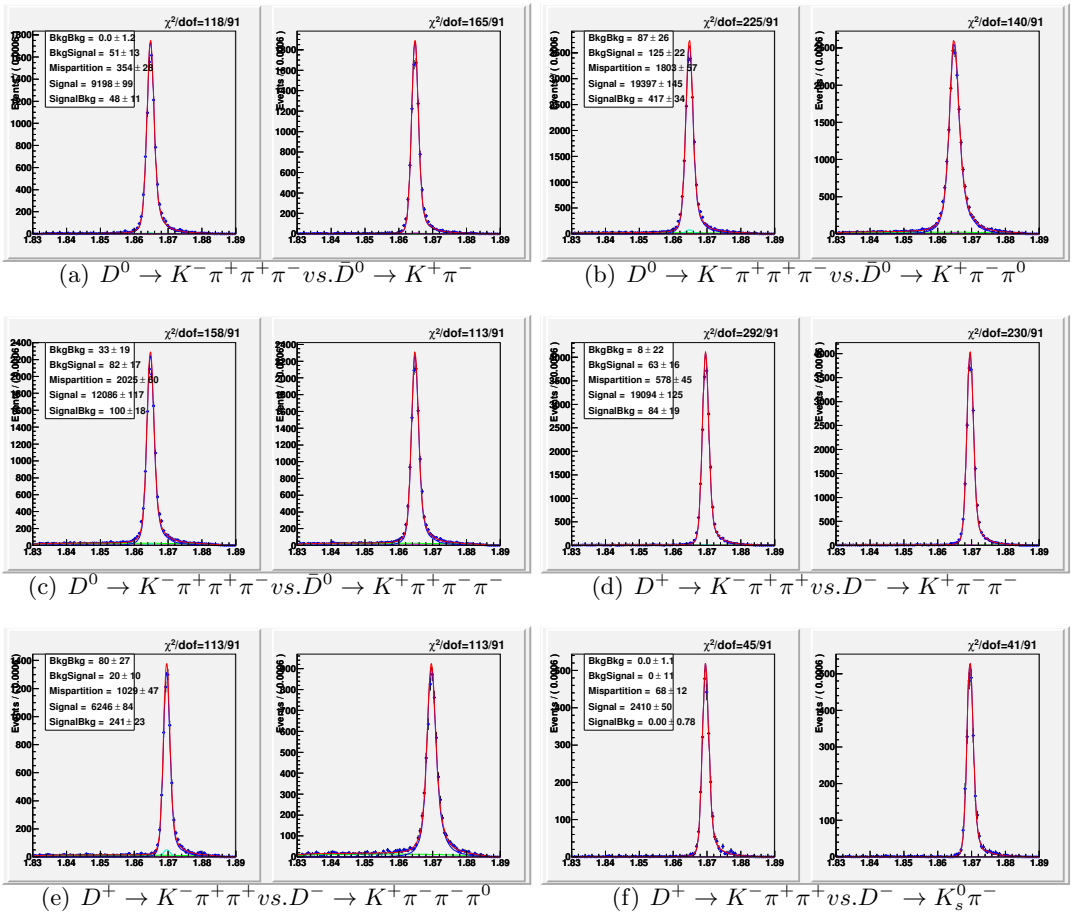

(a) $D^0 \to K^-\pi^+\pi^+\pi^- vs. \bar{D}^0 \to K^+\pi^-$ (b) $D^0 \to K^-\pi^+\pi^+\pi^- vs. \bar{D}^0 \to K^+\pi^-\pi^0$

(c) $D^0 \to K^-\pi^+\pi^+\pi^- vs. \bar{D}^0 \to K^+\pi^+\pi^-\pi^-$ (d) $D^+ \to K^-\pi^+\pi^+ vs. D^- \to K^+\pi^-\pi^-$

(e) $D^+ \to K^-\pi^+\pi^+ vs. D^- \to K^+\pi^-\pi^-\pi^0$ (f) $D^+ \to K^-\pi^+\pi^+ vs. D^- \to K^0_S\pi^-$

Figure 56: Two-dimensional m_{BC} fits from data used to determine double-tag yields, as detailed in Section 6.5.

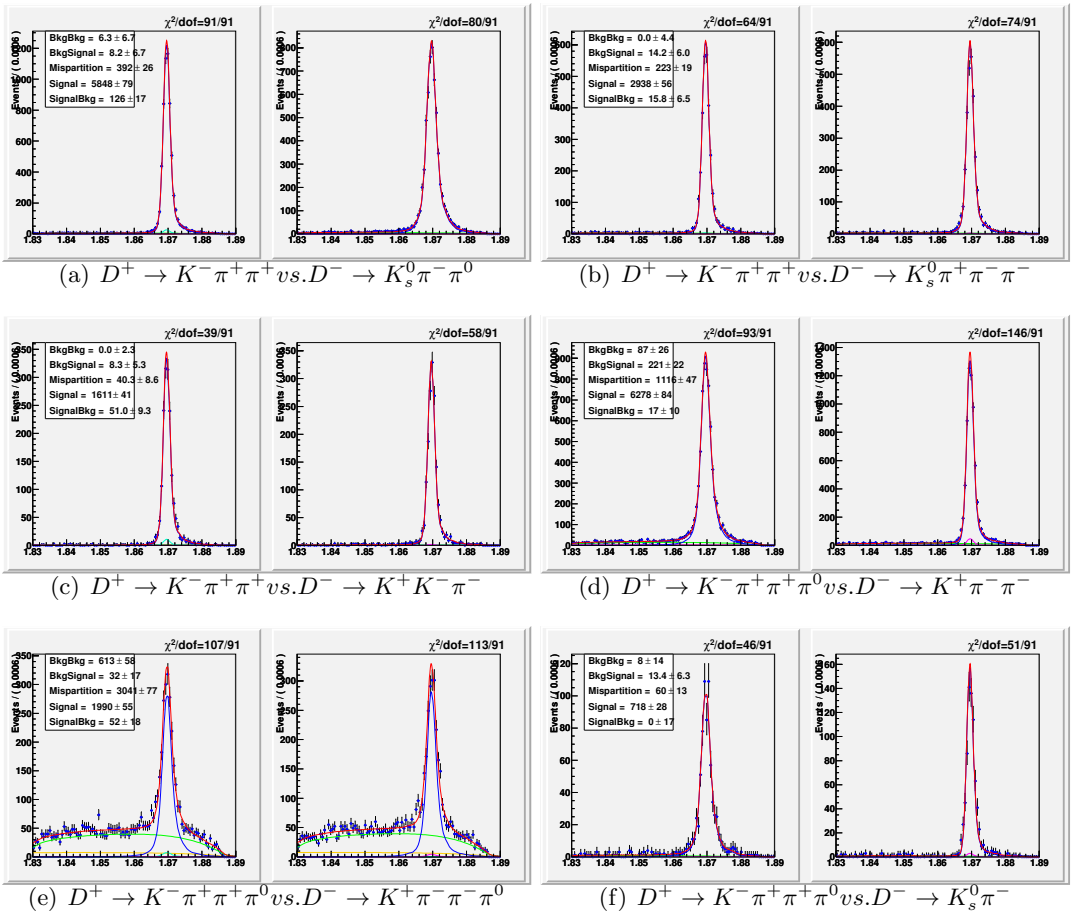

(a) $D^+ \to K^-\pi^+\pi^+ vs. D^- \to K^0_s\pi^-\pi^0$ (b) $D^+ \to K^-\pi^+\pi^+ vs. D^- \to K^0_s\pi^+\pi^-\pi^-$

(c) $D^+ \to K^-\pi^+\pi^+ vs. D^- \to K^+K^-\pi^-$ (d) $D^+ \to K^-\pi^+\pi^+\pi^0 vs. D^- \to K^+\pi^-\pi^-$

(e) $D^+ \to K^-\pi^+\pi^+\pi^0 vs. D^- \to K^+\pi^-\pi^-\pi^0$ (f) $D^+ \to K^-\pi^+\pi^+\pi^0 vs. D^- \to K^0_s\pi^-$

Figure 57: Two-dimensional m_{BC} fits from data used to determine double-tag yields, as detailed in Section 6.5.

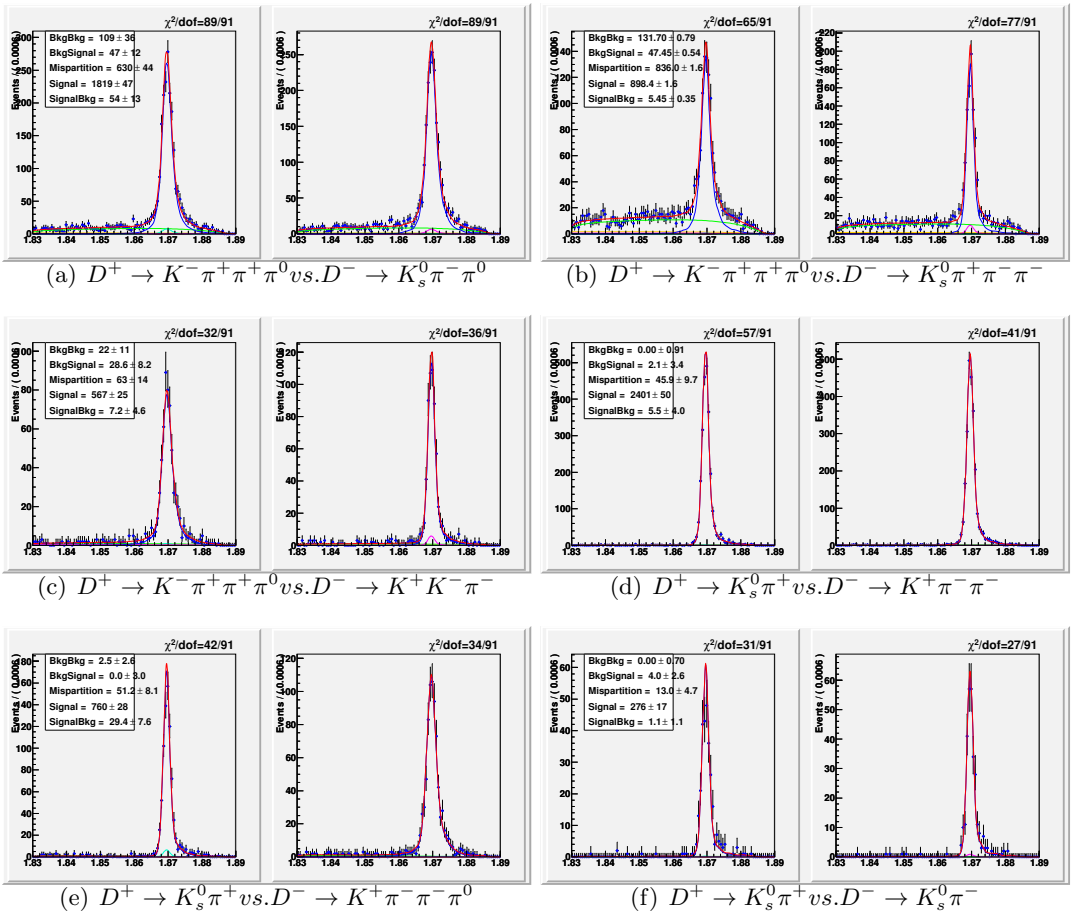

(a) $D^+ \to K^-\pi^+\pi^+\pi^0 vs. D^- \to K^0_s\pi^-\pi^0$ (b) $D^+ \to K^-\pi^+\pi^+\pi^0 vs. D^- \to K^0_s\pi^+\pi^-\pi^-$

(c) $D^+ \to K^-\pi^+\pi^+\pi^0 vs. D^- \to K^+K^-\pi^-$ (d) $D^+ \to K^0_s\pi^+ vs. D^- \to K^+\pi^-\pi^-$

(e) $D^+ \to K^0_s\pi^+ vs. D^- \to K^+\pi^-\pi^-\pi^0$ (f) $D^+ \to K^0_s\pi^+ vs. D^- \to K^0_s\pi^-$

Figure 58: Two-dimensional m_{BC} fits from data used to determine double-tag yields, as detailed in Section 6.5.

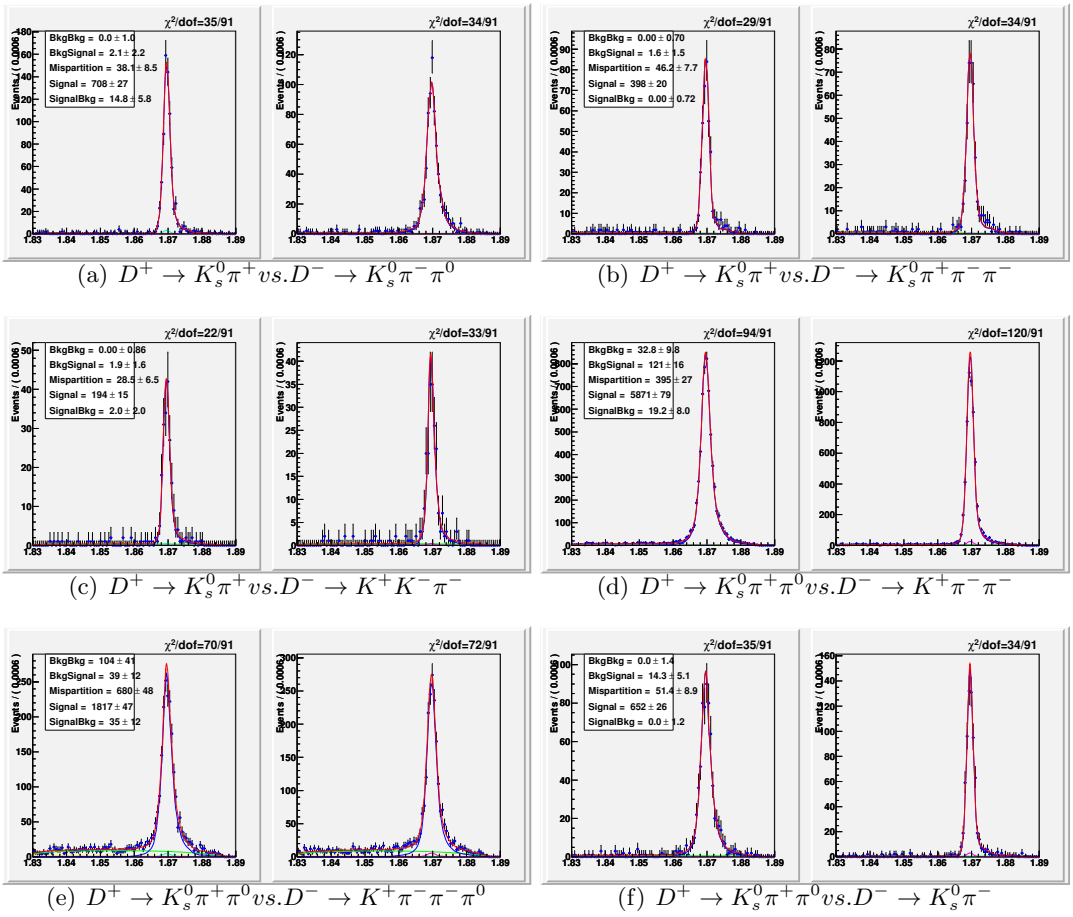

(a) $D^+ \to K^0_s\pi^+ vs. D^- \to K^0_s\pi^-\pi^0$ (b) $D^+ \to K^0_s\pi^+ vs. D^- \to K^0_s\pi^+\pi^-\pi^-$

(c) $D^+ \to K^0_s\pi^+ vs. D^- \to K^+K^-\pi^-$ (d) $D^+ \to K^0_s\pi^+\pi^0 vs. D^- \to K^+\pi^-\pi^-$

(e) $D^+ \to K^0_s\pi^+\pi^0 vs. D^- \to K^+\pi^-\pi^-\pi^0$ (f) $D^+ \to K^0_s\pi^+\pi^0 vs. D^- \to K^0_s\pi^-$

Figure 59: Two-dimensional m_{BC} fits from data used to determine double-tag yields, as detailed in Section 6.5.

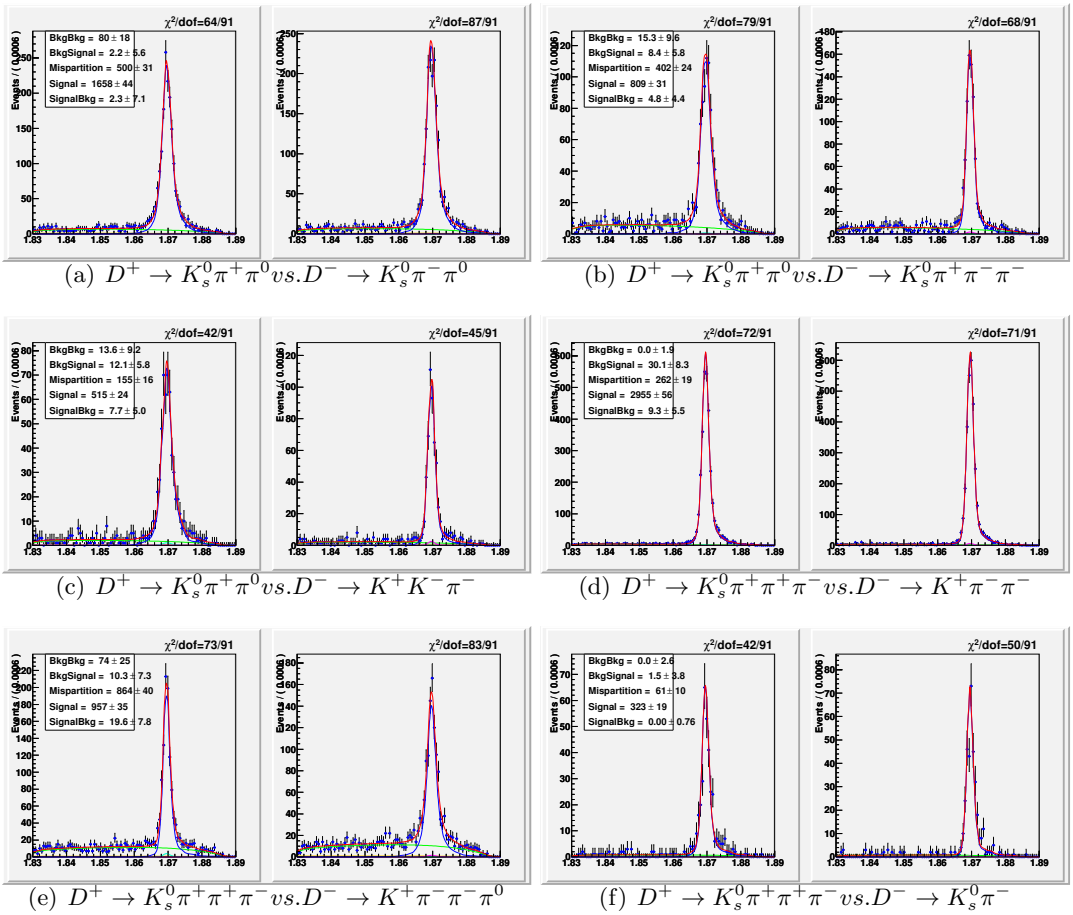

(a) $D^+ \to K^0_s\pi^+\pi^0 vs. D^- \to K^0_s\pi^-\pi^0$ (b) $D^+ \to K^0_s\pi^+\pi^0 vs. D^- \to K^0_s\pi^+\pi^-\pi^-$

(c) $D^+ \to K^0_s\pi^+\pi^0 vs. D^- \to K^+K^-\pi^-$ (d) $D^+ \to K^0_s\pi^+\pi^+\pi^- vs. D^- \to K^+\pi^-\pi^-$

(e) $D^+ \to K^0_s\pi^+\pi^+\pi^- vs. D^- \to K^+\pi^-\pi^-\pi^0$ (f) $D^+ \to K^0_s\pi^+\pi^+\pi^- vs. D^- \to K^0_s\pi^-$

Figure 60: Two-dimensional m_{BC} fits from data used to determine double-tag yields, as detailed in Section 6.5.

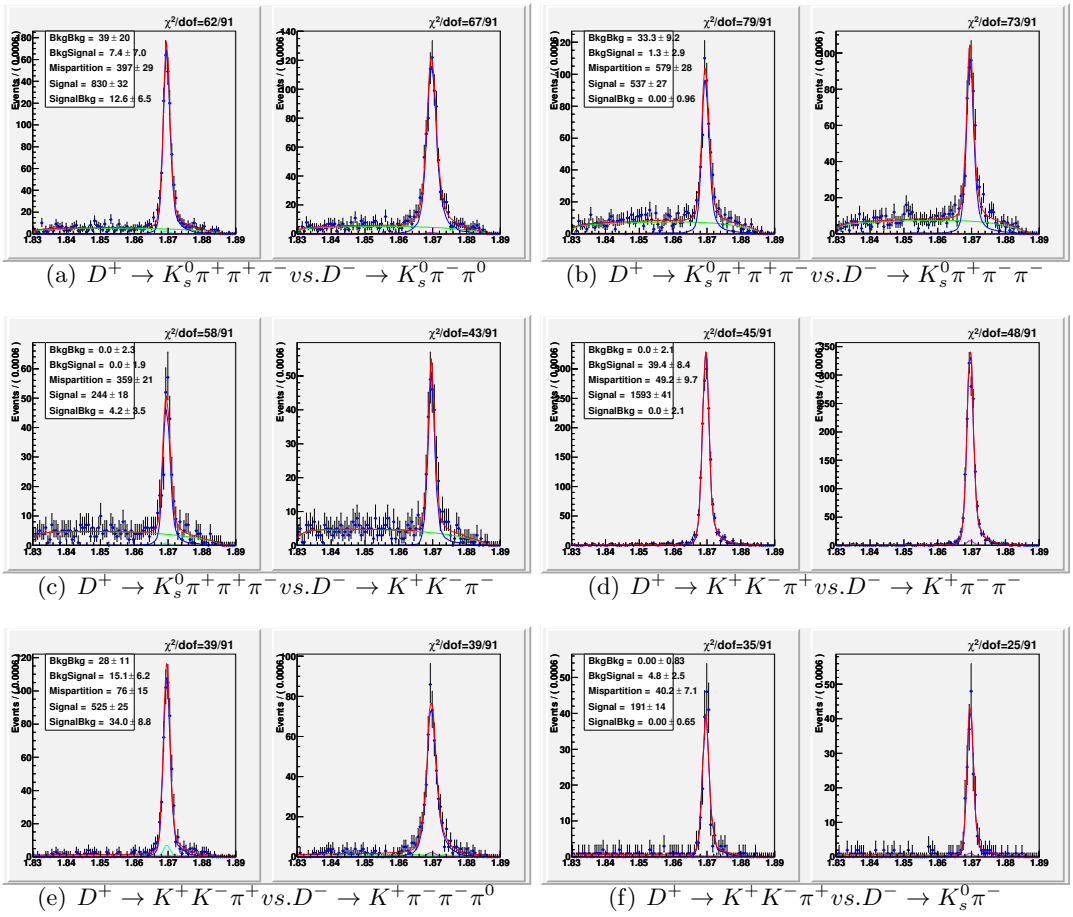

(a) $D^+ \to K^0_s\pi^+\pi^+\pi^- vs. D^- \to K^0_s\pi^-\pi^0$ (b) $D^+ \to K^0_s\pi^+\pi^+\pi^- vs. D^- \to K^0_s\pi^+\pi^-\pi^-$

(c) $D^+ \to K^0_s\pi^+\pi^+\pi^- vs. D^- \to K^+K^-\pi^-$ (d) $D^+ \to K^+K^-\pi^+ vs. D^- \to K^+\pi^-\pi^-$

(e) $D^+ \to K^+K^-\pi^+ vs. D^- \to K^+\pi^-\pi^-\pi^0$ (f) $D^+ \to K^+K^-\pi^+ vs. D^- \to K^0_s\pi^-$

Figure 61: Two-dimensional m_{BC} fits from data used to determine double-tag yields, as detailed in Section 6.5.

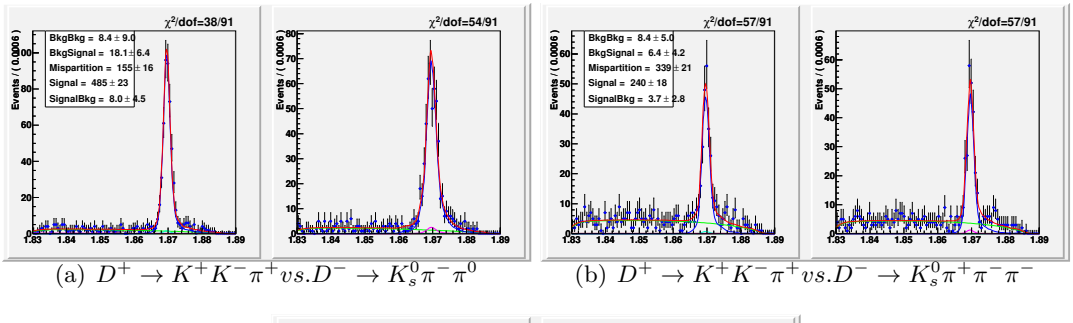

(a) $D^+ \to K^+K^-\pi^+ vs. D^- \to K^0_s\pi^-\pi^0$ (b) $D^+ \to K^+K^-\pi^+ vs. D^- \to K^0_s\pi^+\pi^-\pi^-$

(c) $D^+ \to K^+K^-\pi^+ vs. D^- \to K^+K^-\pi^-$

Figure 62: Two-dimensional m_{BC} fits from data used to determine double-tag yields, as detailed in Section 6.5.

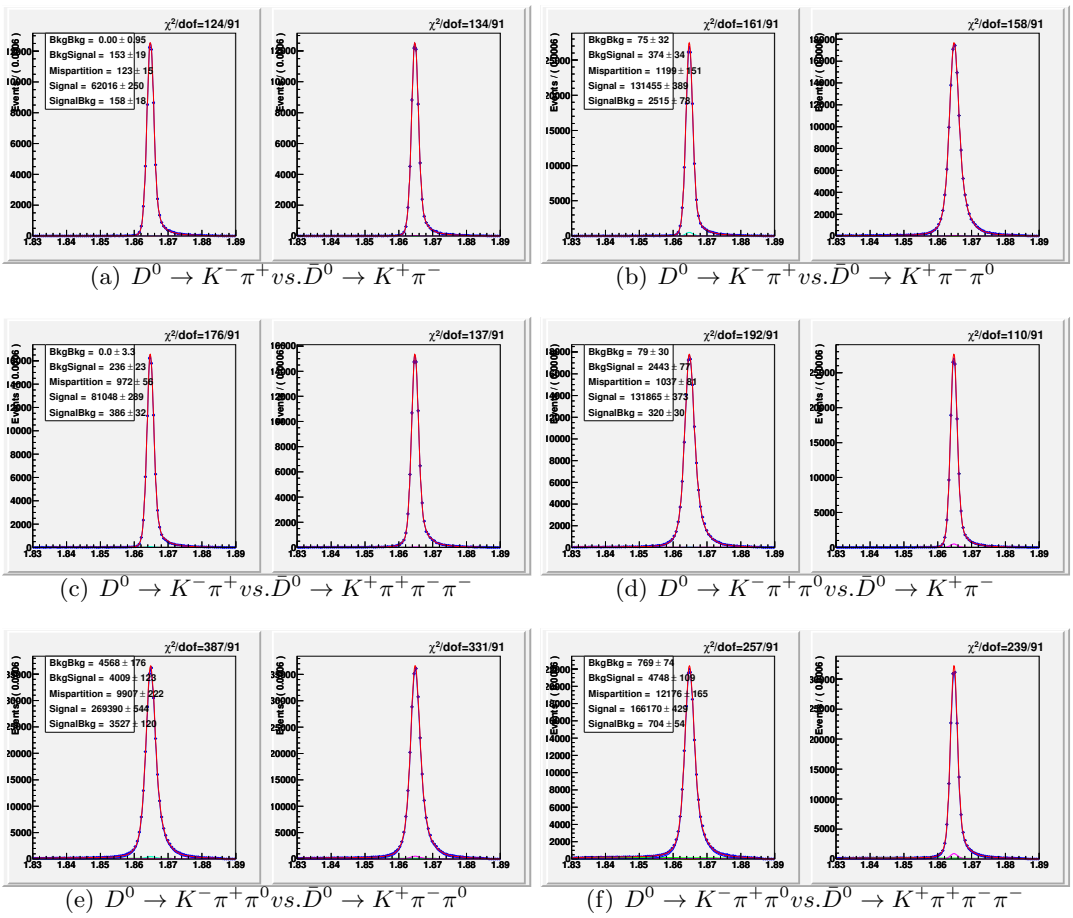

(a) $D^0 \to K^-\pi^+ vs. \bar{D}^0 \to K^+\pi^-$ (b) $D^0 \to K^-\pi^+ vs. \bar{D}^0 \to K^+\pi^-\pi^0$

(c) $D^0 \to K^-\pi^+ vs. \bar{D}^0 \to K^+\pi^+\pi^-\pi^-$ (d) $D^0 \to K^-\pi^+\pi^0 vs. \bar{D}^0 \to K^+\pi^-$

(e) $D^0 \to K^-\pi^+\pi^0 vs. \bar{D}^0 \to K^+\pi^-\pi^0$ (f) $D^0 \to K^-\pi^+\pi^0 vs. \bar{D}^0 \to K^+\pi^+\pi^-\pi^-$

Figure 63: Two-dimensional m_{BC} fits used to determine double-tag efficiencies, as detailed in Section 6.5, from a ∼10x data-sized sample of $D\bar{D}$ and background Monte Carlo sample, as described in Section 5.

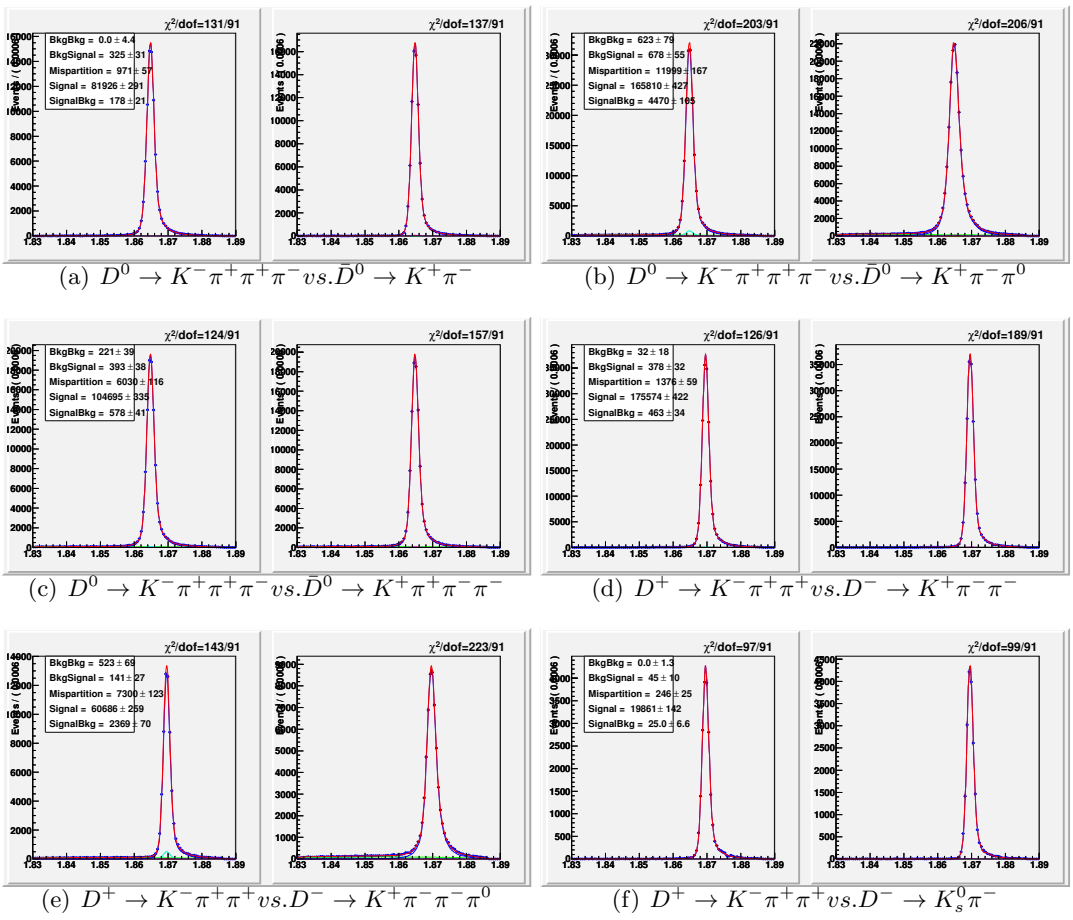

(a) $D^0 \to K^-\pi^+\pi^+\pi^- vs. \bar{D}^0 \to K^+\pi^-$ (b) $D^0 \to K^-\pi^+\pi^+\pi^- vs. \bar{D}^0 \to K^+\pi^-\pi^0$

(c) $D^0 \to K^-\pi^+\pi^+\pi^- vs. \bar{D}^0 \to K^+\pi^+\pi^-\pi^-$ (d) $D^+ \to K^-\pi^+\pi^+ vs. D^- \to K^+\pi^-\pi^-$

(e) $D^+ \to K^-\pi^+\pi^+ vs. D^- \to K^+\pi^-\pi^-\pi^0$ (f) $D^+ \to K^-\pi^+\pi^+ vs. D^- \to K^0_S\pi^-$

Figure 64: Two-dimensional m_{BC} fits used to determine double-tag efficiencies, as detailed in Section 6.5, from a ∼10x data-sized sample of $D\bar{D}$ and background Monte Carlo sample, as described in Section 5.

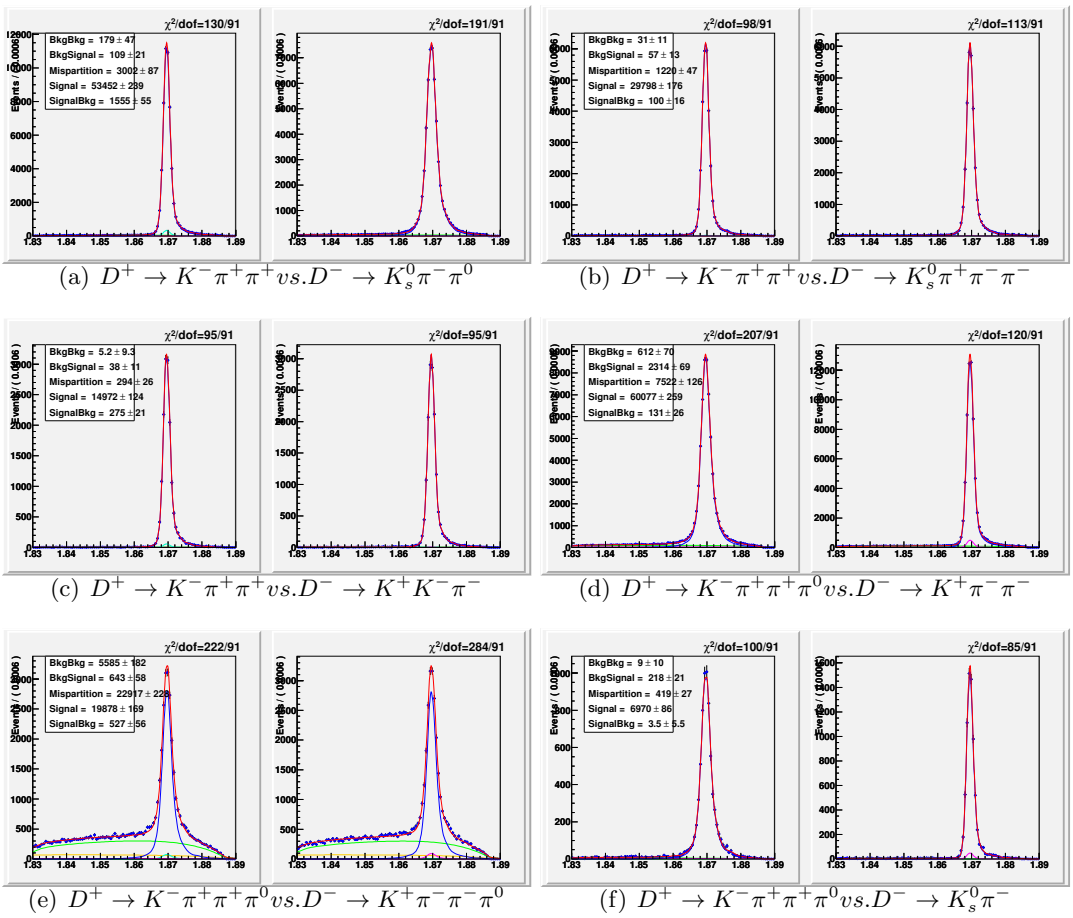

(a) $D^+ \to K^-\pi^+\pi^+ vs. D^- \to K^0_s\pi^-\pi^0$ (b) $D^+ \to K^-\pi^+\pi^+ vs. D^- \to K^0_s\pi^+\pi^-\pi^-$

(c) $D^+ \to K^-\pi^+\pi^+ vs. D^- \to K^+K^-\pi^-$ (d) $D^+ \to K^-\pi^+\pi^+\pi^0 vs. D^- \to K^+\pi^-\pi^-$

(e) $D^+ \to K^-\pi^+\pi^+\pi^0 vs. D^- \to K^+\pi^-\pi^-\pi^0$ (f) $D^+ \to K^-\pi^+\pi^+\pi^0 vs. D^- \to K^0_s\pi^-$

Figure 65: Two-dimensional m_{BC} fits used to determine double-tag efficiencies, as detailed in Section 6.5, from a ∼10x data-sized sample of $D\bar{D}$ and background Monte Carlo sample, as described in Section 5.

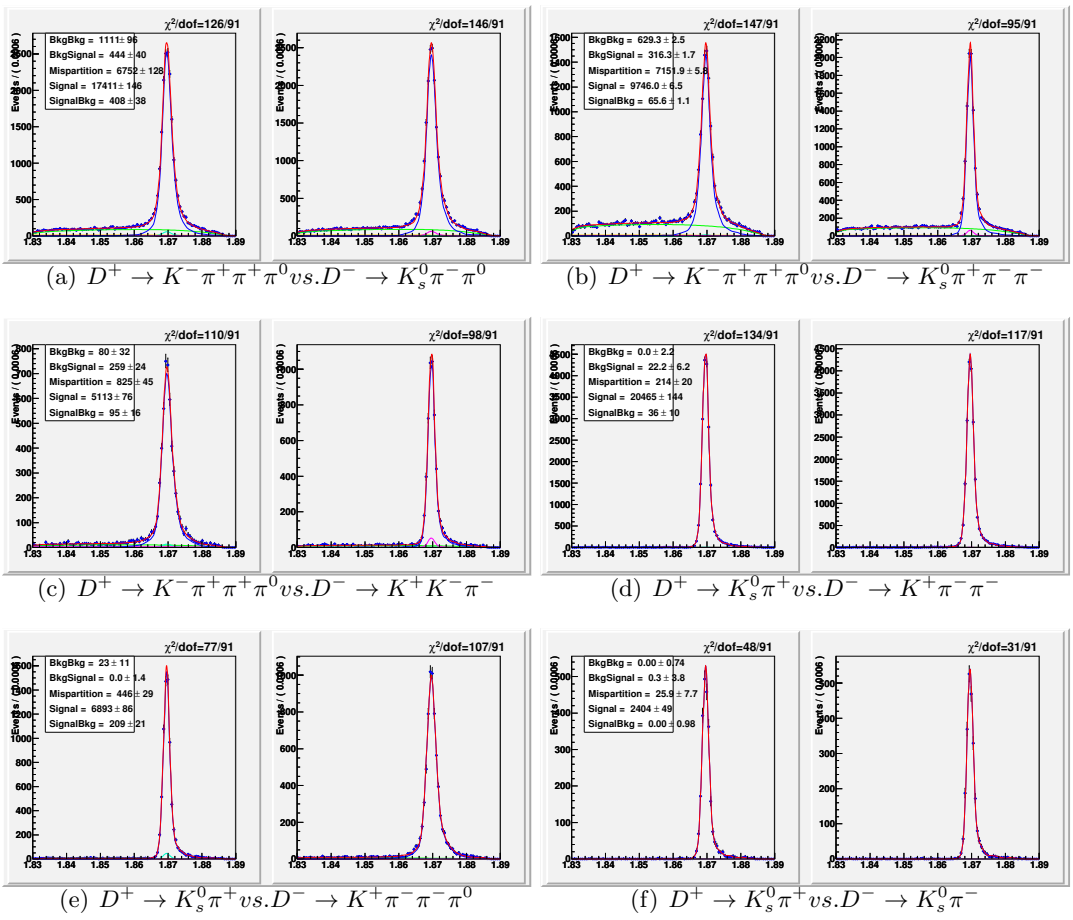

(a) $D^+ \to K^-\pi^+\pi^+\pi^0 vs. D^- \to K^0_s\pi^-\pi^0$ (b) $D^+ \to K^-\pi^+\pi^+\pi^0 vs. D^- \to K^0_s\pi^+\pi^-\pi^-$

(c) $D^+ \to K^-\pi^+\pi^+\pi^0 vs. D^- \to K^+K^-\pi^-$ (d) $D^+ \to K^0_s\pi^+ vs. D^- \to K^+\pi^-\pi^-$

(e) $D^+ \to K^0_s\pi^+ vs. D^- \to K^+\pi^-\pi^-\pi^0$ (f) $D^+ \to K^0_s\pi^+ vs. D^- \to K^0_s\pi^-$

Figure 66: Two-dimensional m_{BC} fits used to determine double-tag efficiencies, as detailed in Section 6.5, from a ∼10x data-sized sample of $D\bar{D}$ and background Monte Carlo sample, as described in Section 5.

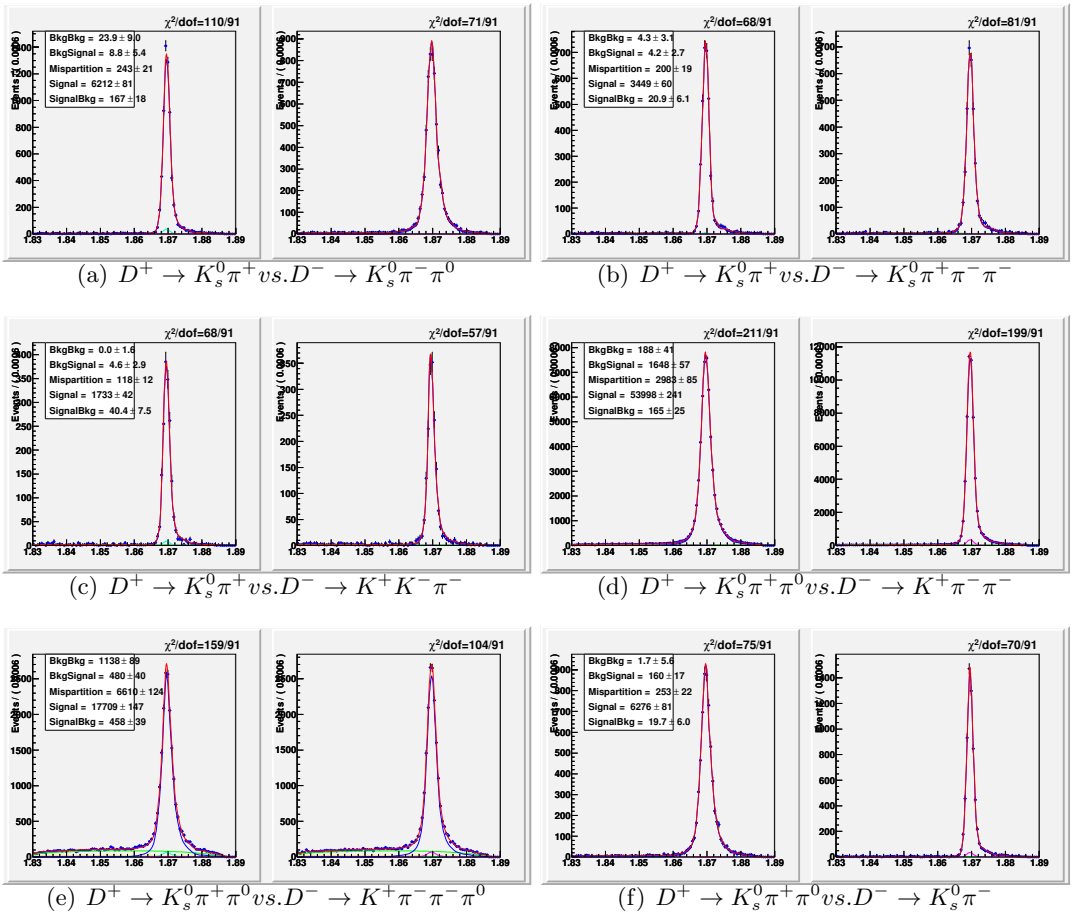

(a) $D^+ \to K^0_s\pi^+ vs. D^- \to K^0_s\pi^-\pi^0$ (b) $D^+ \to K^0_s\pi^+ vs. D^- \to K^0_s\pi^+\pi^-\pi^-$

(c) $D^+ \to K^0_s\pi^+ vs. D^- \to K^+K^-\pi^-$ (d) $D^+ \to K^0_s\pi^+\pi^0 vs. D^- \to K^+\pi^-\pi^-$

(e) $D^+ \to K^0_s\pi^+\pi^0 vs. D^- \to K^+\pi^-\pi^-\pi^0$ (f) $D^+ \to K^0_s\pi^+\pi^0 vs. D^- \to K^0_s\pi^-$

Figure 67: Two-dimensional m_{BC} fits used to determine double-tag efficiencies, as detailed in Section 6.5, from a ∼10x data-sized sample of $D\bar{D}$ and background Monte Carlo sample, as described in Section 5.

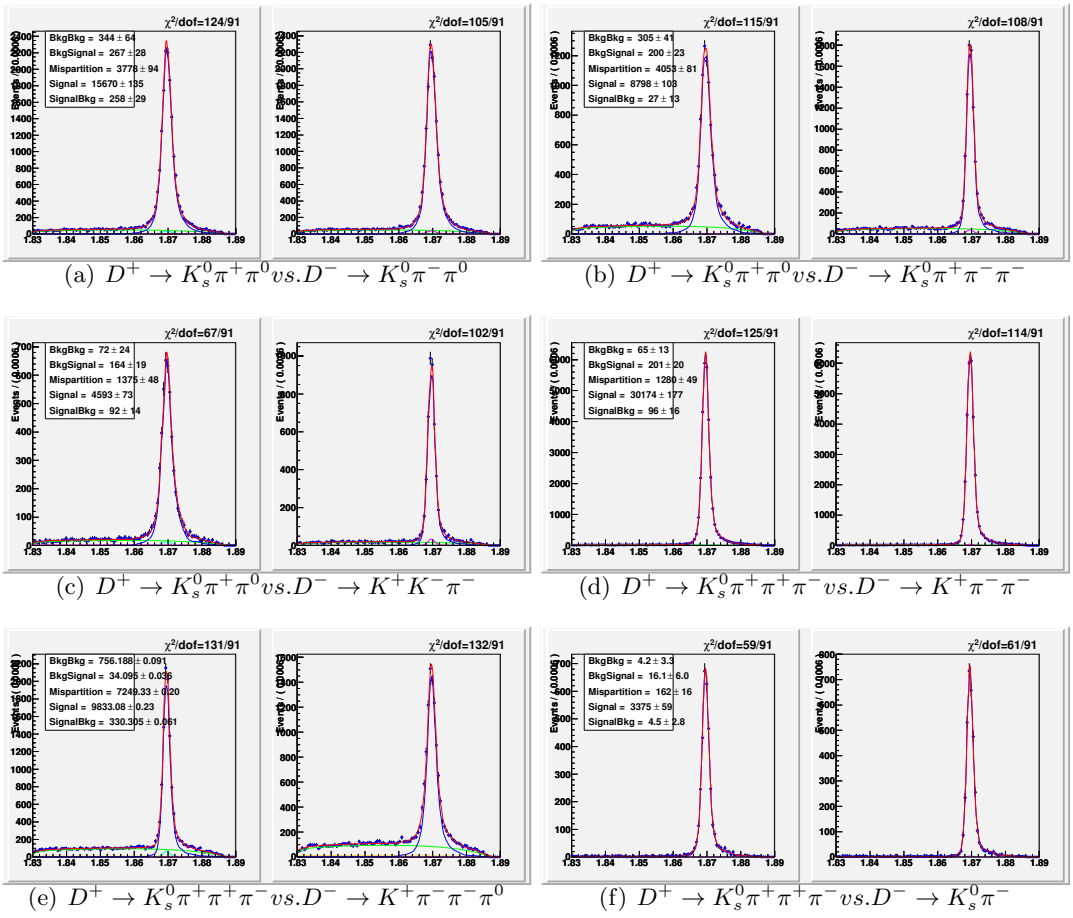

(a) $D^+ \to K^0_s\pi^+\pi^0 vs. D^- \to K^0_s\pi^-\pi^0$ (b) $D^+ \to K^0_s\pi^+\pi^0 vs. D^- \to K^0_s\pi^+\pi^-\pi^-$

(c) $D^+ \to K^0_s\pi^+\pi^0 vs. D^- \to K^+K^-\pi^-$ (d) $D^+ \to K^0_s\pi^+\pi^+\pi^- vs. D^- \to K^+\pi^-\pi^-$

(e) $D^+ \to K^0_s\pi^+\pi^+\pi^- vs. D^- \to K^+\pi^-\pi^-\pi^0$ (f) $D^+ \to K^0_s\pi^+\pi^+\pi^- vs. D^- \to K^0_s\pi^-$

Figure 68: Two-dimensional m_{BC} fits used to determine double-tag efficiencies, as detailed in Section 6.5, from a ∼10x data-sized sample of $D\bar{D}$ and background Monte Carlo sample, as described in Section 5.

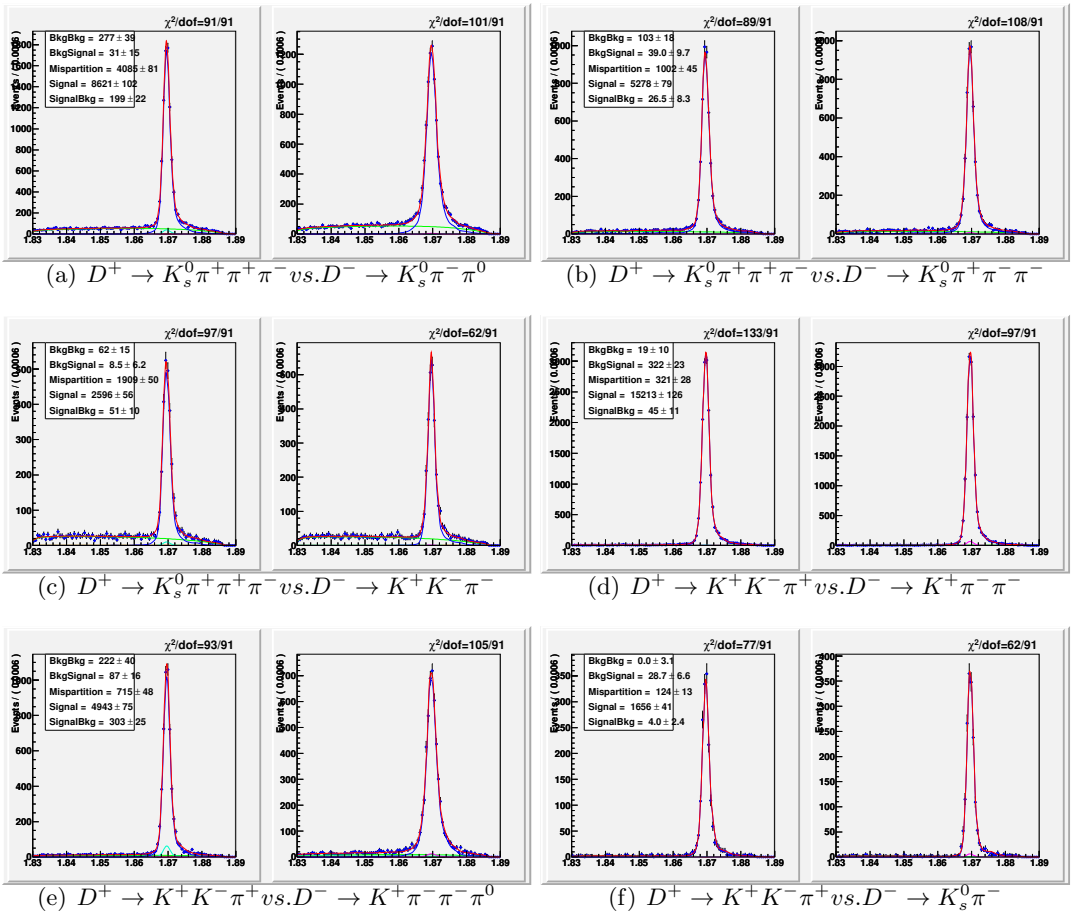

(a) $D^+ \to K^0_s\pi^+\pi^+\pi^- vs. D^- \to K^0_s\pi^-\pi^0$ (b) $D^+ \to K^0_s\pi^+\pi^+\pi^- vs. D^- \to K^0_s\pi^+\pi^-\pi^-$

(c) $D^+ \to K^0_s\pi^+\pi^+\pi^- vs. D^- \to K^+K^-\pi^-$ (d) $D^+ \to K^+K^-\pi^+ vs. D^- \to K^+\pi^-\pi^-$

(e) $D^+ \to K^+K^-\pi^+ vs. D^- \to K^+\pi^-\pi^-\pi^0$ (f) $D^+ \to K^+K^-\pi^+ vs. D^- \to K^0_s\pi^-$

Figure 69: Two-dimensional m_{BC} fits used to determine double-tag efficiencies, as detailed in Section 6.5, from a ∼10x data-sized sample of $D\bar{D}$ and background Monte Carlo sample, as described in Section 5.

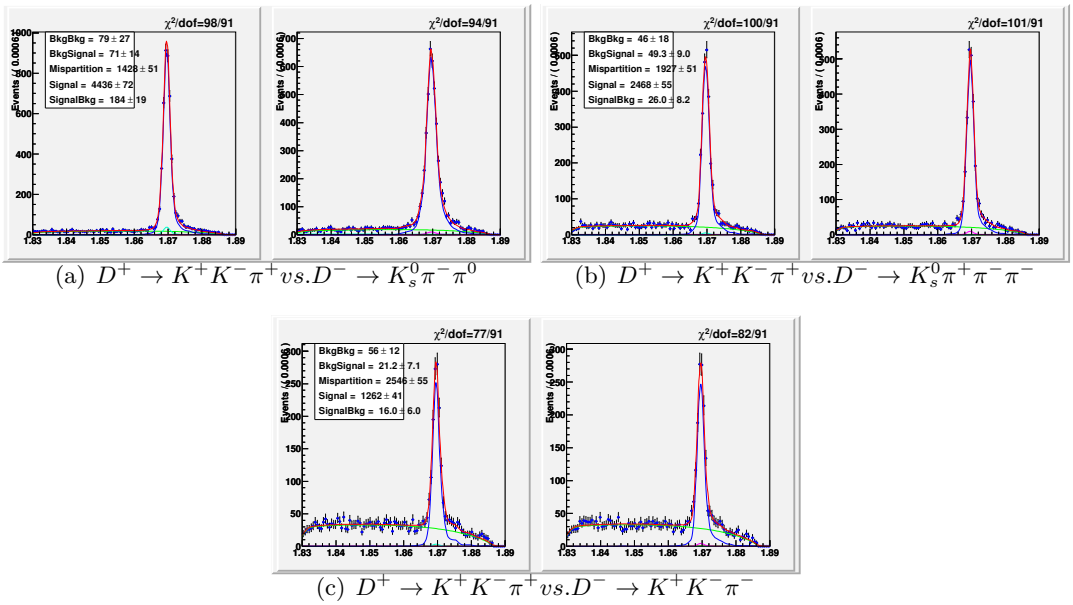

(a) $D^+ \to K^+K^-\pi^+ vs. D^- \to K^0_s\pi^-\pi^0$ (b) $D^+ \to K^+K^-\pi^+ vs. D^- \to K^0_s\pi^+\pi^-\pi^-$

(c) $D^+ \to K^+K^-\pi^+ vs. D^- \to K^+K^-\pi^-$

Figure 70: Two-dimensional m_{BC} fits used to determine double-tag efficiencies, as detailed in Section 6.5, from a ∼10x data-sized sample of $D\bar{D}$ and background Monte Carlo sample, as described in Section 5.